



**Politecnico
di Torino**

POLITECNICO DI TORINO

Master's degree in Civil Engineering

Structural Design of Asphalt Pavements for Renewable Energy Plants

Supervisors:

Prof. Lucia Tsantilis
Prof. Davide Dalmazzo
Prof. Ezio Santagata

Candidate:

Hao Xiang

April 2023

To my family

Acknowledgment

I would like to express my deepest gratitude to my supervisor, Professor Lucia Tsantilis, for all of her excellent guidance and assistance over the period of this study effort.

I would like to extend my sincere gratitude to my supervisor, Professor Davide Dalmazzo, for his invaluable support, assistance, and advice.

I also wish to show my appreciation to Professor Ezio Santagata for his invaluable contribution and sheer inspiration towards fostering my academic and personal development.

Finally, a warm thank you to all the friends I made during my two-year academic journey in Turin while studying at PoliTo. I am truly thankful for the experiences and moments we have shared together.

Abstract

The world has seen an explosive growth in renewable energy development activity in recent years, attributed to the significant technological advancements in green energy (e.g., wind and solar energy), alongside other emerging technologies. The development of wind and solar farms requires movement of very heavy equipment and components on Farm-to-Market (FM) roads during installation and operation phases by Overweight/Oversize (OW/OS) hauling units. Such moves of OW/OS vehicles necessitate designing the FM pavements to have adequate structural capacity that can accommodate the heavy and slow-moving nature of hauling vehicle.

The main objective of this study is the definition of a mechanistic-empirical methodology for the structural design of asphalt pavements in renewable energy plants. More specifically, the following aspects were analyzed in the thesis:

- The effects of climate on structural design, with special emphasis on the role played by monthly variations of temperature and precipitation in the definition of the mechanical characteristics of both the asphalt layers and the subgrade soil.
- Shear failure mechanisms in unbound layers induced by OW/OS vehicles and the corresponding design approaches.
- The influence of the model used for traffic homogenization, with the comparison of different reference axles.
- Reference traffic spectra for wind and solar farms.

These points were thoroughly analyzed and implemented in a mechanistic-empirical structural design methodology specifically developed for new asphalt pavements in wind and solar farms.

Keywords: Asphalt Pavement, Pavement Structural Analysis, Localized Shear Failure Analysis, Shear Stability, Overweight/Oversize (OW/OS) Vehicles, Renewable Energy Facilities, Wind Plant, Solar Plant, Reference Axle, Environmental Effects

Contents

1. Introduction.....	1
1.1 Problem Statement	3
1.2 Scope and Objectives	5
1.3 Outline of The Thesis	5
2. Literature Review	7
2.1 Impact of Green Energy Development on Road Infrastructure.....	7
2.1.1 Wind and Solar Energy Development	7
2.1.2 Wind and Solar Farms Associated Truck Traffic	12
2.1.3 The Traffic Impacts Induced by Green Energy Development on Roadways	14
2.2 Flexible Pavement Design Methodologies	15
2.2.1 Empirical design	15
2.2.2 Mechanistic Design.....	16
2.2.3 Mechanistic-Empirical Design Method	17
2.3 Environmental Effects Overview	18
2.4 Review of Reference Axle Used in Different Pavement Design Standards	19
2.5 The Effect of Different Load Configurations on Shear Stability Analysis	20
3. Effects of Climate Variation on Structural Analysis	22
3.1 Effects of Moisture Variation on Subgrade Resilient Modulus	22
3.1.1 M_R -Moisture Model	24
3.2 Effects of Temperature Variation on HMA Dynamic Modulus.....	25
3.3 Analysis Procedure	27
3.3.1 Site Description.....	27
3.3.2 Traffic Data Collection and Analysis	28
3.3.3 Climatic Statistics	32
3.3.4 Pavement Structure and Material Properties	34
3.3.5 Analysis Periods Definition	37
3.3.6 Performances Prediction	40

3.4 Results Analysis and Discussions	42
4. Effect of the Reference Axle Load Used in Traffic Modeling on Structural Analysis	44
4.1 Analysis Methodology	45
4.1.1 Pavement Structure and Materials Properties	45
4.1.2 Traffic Analysis	45
4.1.3 Critical Responses Calculation	47
4.1.4 Performances Prediction	49
4.2 Result Analysis and Discussions	50
5. Shear Stability Analysis.....	52
5.1 Analysis Methodology	53
5.1.1 Evaluation of Limiting Shear Stress	56
5.1.2 Structural Analysis.....	62
5.1.3 Shear Stability Verification	64
5.2 Material Properties Considerations	65
6. Reference Traffic Spectra for Wind and Solar Farms	67
6.1 Wind Farm.....	67
6.1.1 Construction Phase	69
6.1.2 Operational Phase	77
6.1.3 Decommissioning Phase	78
6.1.4 Traffic Spectrum	80
6.2 Solar Farm	84
6.2.1 Construction Phase	86
6.2.2 Operational Phase	91
6.2.3 Decommissioning Phase	92
6.2.4 Traffic Spectrum	92
6.3 Estimations of Equivalent Single Axle Loads.....	95
6.3.1 Determinations of Axle Load Distributions.....	95
6.3.2 Estimates of ESALs	111
6.4 Summary	123
7. Pavements Design for Wind and Solar Plants	124

7.1 Description of Pavements Section and Layer Materials	124
7.2 Description of Traffic Information	126
7.3 Pavement Design for Solar Farm	128
7.3.1 Determinations of Layer Mechanical Properties	128
7.3.2 Shear Stability Design	129
7.3.3 Fatigue Cracking and Rutting Design.....	139
7.4 Pavement Design for Wind Farm	143
7.4.1 Determinations of Layer Mechanical Properties	143
7.4.2 Shear Stability Design	144
7.4.3 Fatigue Cracking and Rutting Design.....	150
7.5 Summary	152
8. Conclusions and Recommendations	154
8.1 Conclusions	155
8.2 Recommendations for Future Works	157
9. References.....	158
10. Annex : Structural Design Procedure	167

List of Figures

Figure 1.1 A typical modern wind turbine (Burton, 2004).....	2
Figure 1.2 Wind plant (Cesar Quiroga et al., 2012)	2
Figure 1.3 Solar Photovoltaic Cell System (NSW, 2018)	3
Figure 1.4 Solar Thermal Power System (J. Prozzi et al.,2011).....	3
Figure 1.5 Turbine blade transport in wind farm.....	4
Figure 1.6 Main transformer transport in solar farm	4
Figure 2.1 Installed wind power capacity in Europe, 2013 - 2022.....	8
Figure 2.2 Wind Capacity Growth in Texas, 2000 - 2009.....	8
Figure 2.3 Outlook of new installations in Europe – WindEurope’s scenarios.	9
Figure 2.4 EU-27 cumulative solar PV installed capacity, 2000 - 2022	10
Figure 2.5 Total solar PV installed capacity globally, 2000 - 2021	10
Figure 2.6 EU-27 total solar PV market scenarios, 2022 - 2030	11
Figure 2.7 Global total solar PV market scenarios, 2022 - 2026.....	11
Figure 2.8 Triple, single axle load and dual wheel load (From left to right) (Jooste and Fernando, 1995).....	20
Figure 2.9 Single-, three-, and five-line load model (From left to right) (Chen et al., 2013)	21
Figure 2.10 Evaluated locations within pavement (Chen et al., 2013).....	21
Figure 3.1 US-127 highway in Clinton, Michigan	28
Figure 3.2 Evaluated response points within pavement	40
Figure 3.3 Damages comparison	42
Figure 4.1 Evaluated response points and two reference axles	48
Figure 4.2 Principal strains and material properties	49
Figure 4.3 Comparison of damages	50
Figure 5.1 Load-Settlement curve (Modified from Whitman and Hoeg, 1966)	53
Figure 5.2 First yielded zone (Whitman and Hoeg, 1966)	54
Figure 5.3 Propagation of the plastic zone (Whitman and Hoeg, 1966)	55

Figure 5.4 Plastic zone reaching the foundation surface (Whitman and Hoeg, 1966)	55
Figure 5.5 Mohr's circle (Renato Lancellotta, 2008)	57
Figure 5.6 Shear and normal stresses in a plane stress state (ODN 218.046-01, 2001)	57
Figure 5.7 Mohr diagram under volumetric stress state (ODN 218.046-01, 2001)	58
Figure 5.8 Stress components and related planes	59
Figure 5.9 Stress components on segment ABE	60
Figure 5.10 Two principal planes	62
Figure 6.1 Wind turbines spacing	68
Figure 6.2 Internal track and hardstand	69
Figure 6.3 Wind turbine composition	71
Figure 6.4 LR 1400 SX Crawler crane	73
Figure 6.5 GMK5120L Mobile crane	73
Figure 6.6 Wind turbine assembly	74
Figure 6.7 Typical cable trenching	75
Figure 6.8 Typical overhead powerline pole	76
Figure 6.9 Typical substation for wind farms	77
Figure 6.10 Wind turbine dismantling	79
Figure 6.11 10 5MW array block showing location of PCU and access track	85
Figure 6.12 Proposed solar development arrangement	86
Figure 6.13 A typical illustration of PV panels wired on one portrait tracker	88
Figure 6.14 Typical illustration of a PCU within the array.	89
Figure 6.15 Typical main transformer in solar farm	90
Figure 6.16 Typical battery storage units, located together	90
Figure 6.17 Chain wire fence with barbed wire topping	91
Figure 6.18 A typical flatbed semi-trailer	96
Figure 6.19 VOLVO® FH 16 Tractor	97
Figure 6.20 Three-axle flatbed semi-trailer	97
Figure 6.21 Computational static model of flatbed trailer	98
Figure 6.22 A typical lowbed trailer	101

Figure 6.23 The drawing of lowbed semi-trailer	102
Figure 6.24 The FAW® 6x4 15.5m ³ dump truck	103
Figure 6.25 Drawing of the dump truck	103
Figure 6.26 Computational model of dump truck.....	104
Figure 6.27 FAW® 6m ³ concrete mixer	105
Figure 6.28 Drawing of the concrete mixer	106
Figure 6.29 A typical water tanker	106
Figure 6.30 BEIBEN 20 kL water tanker	107
Figure 6.31 Hauling unit for blades	108
Figure 6.32 Hauling unit for bacelle and base tower sections	109
Figure 6.33 Hauling unit for heavier tower sections	109
Figure 6.34 Hauling unit for transformers, driver trains and hubs	110
Figure 7.1 Typical conventional flexible pavement structure (Huang, 2004)	125
Figure 7.2 Pavement structure	125
Figure 7.3 The heaviest axle configuration in solar farm	126
Figure 7.4 The heaviest axle load configuration in wind farm	127
Figure 7.5 Five-axle group (only 4 axles illustated).....	127
Figure 7.6 Evaluated response points within pavement	129
Figure 7.7 Evaluation points in the pavement under ESWL	135
Figure 7.8 Evaluated response points within pavement	141
Figure 7.9 Evaluated response points within pavement - Wind farm.....	144

List of Tables

Table 2.1 Estimates of truck traffic associated with site preparation for a single typical wind turbine (Siemens 2.3 MW)	12
Table 2.2 OW/OS Vehicles used for Moving Wind Turbine (1.5 MW) Components	12
Table 2.3 Examples of the estimates of truck traffic associated with solar farms construction.....	13
Table 2.4 OW/OS Vehicles used for moving heavy components in solar farms	14
Table 2.5 Comparison of different reference axles.....	19
Table 3.1 Traffic classification	29
Table 3.2 Axle loads definition.....	29
Table 3.3 Equivalent Axle Load Factor Calculation	30
Table 3.4 Monthly precipitation, 2002-2011	32
Table 3.5 Monthly air temperature, 2002-2011	32
Table 3.6 Moisture content (%)	34
Table 3.7 HMA layers mid-depth temperatures (°C)	34
Table 3.8 Physical properties of the asphalt mixtures	35
Table 3.9 The coefficients of Master curves.....	35
Table 3.10 Dynamic moduli of HMA mixtures (MPa).....	35
Table 3.11 Degree of saturation (S) in each month	35
Table 3.12 Regression parameters used in MR-moisture model	36
Table 3.13 Monthly resilient modulus values of subgrade soils (MPa)	36
Table 3.14 Monthly elastic moduli of unbound subbase layer	37
Table 3.15 Mechanical properties in 12 analysis periods (MPa).....	37
Table 3.16 Subgrade and subbase moduli in 5 analysis periods.....	38
Table 3.17 HMA moduli in 5 analysis periods	38
Table 3.18 Pavement material mechanical property models in five analysis periods.....	39
Table 3.19 Subgrade and subbase moduli in 3 analysis periods.....	39

Table 3.20 HMA moduli in 3 analysis periods	39
Table 3.21 Pavement material mechanical property models in 3 analysis periods.....	39
Table 3.22 Parameters used in transfer functions	41
Table 3.23 Predicted fatigue and rutting damages.....	42
Table 4.1 Key traffic information	45
Table 4.2 Equivalent axle load factor to 120 kN standard single-axle	45
Table 4.3 Comparison of ESALs with two reference axles.....	47
Table 4.4 Principal response strains	48
Table 5.1 Typical Cohesion and Angle of Friction Values for Subgrade Materials	66
Table 5.2 Typical Cohesion and Angle of Friction Values for Base/Sub-base Materials	66
Table 5.3 Physical Characteristics of Structural Layer Materials	66
Table 6.1 Wind Turbine Components (Vestas V162-6.2 MW).....	71
Table 6.2 Employed specific hauling vehicles	72
Table 6.3 Crawler crane components	72
Table 6.4 Approximate dimension and load of transformer.....	76
Table 6.5 Traffic Spectrum Estimates for wind plant.....	81
Table 6.6 The dimensions of construction compounds	87
Table 6.7 Dimension and packing information of PV panel	88
Table 6.8 Traffic Spectrum Estimates for solar plant.....	93
Table 6.9 Dimensions and unladen axle weights of tractor	97
Table 6.10 Dimensions and unladen axle weights of flatbed semi-trailer	98
Table 6.11 Load distribution factors of flatbed semi-trailer.....	100
Table 6.12 Axle loads distribution of flatbed trailer (kN)	101
Table 6.13 Dimensions and unladen axle weights of lowbed semi-trailer.....	102
Table 6.14 Axle loads distribution of flatbed trailer (kN)	102
Table 6.15 Dimensions and unladen axle weights of dump truck	103
Table 6.16 Axle loads distribution of dump truck (kN)	105
Table 6.17 Axle loads distribution of concrete mixer (kN).....	106
Table 6.18 Dimensions and unladen axle weights of water tanker.....	107

Table 6.19 Axle loads distribution of water tanker (kN).....	107
Table 6.20 Axle loads distribution of blade hauling unit (kN).....	108
Table 6.21 Axle loads distribution of nacelles and base tower sections hauling unit (kN).....	109
Table 6.22 Axle loads distribution of heavier tower sections hauling unit (kN)	110
Table 6.23 Axle loads distribution of transformers hauling unit (kN)	110
Table 6.24 ESALs of fully loaded dump trucks and water trucks	112
Table 6.25 ESALs of empty dump trucks and water trucks	112
Table 6.26 Weights of construction plant	113
Table 6.27 ESALs of loaded lowbed trailers	113
Table 6.28 ESALs of empty lowbed trailers.....	113
Table 6.29 ESALs of loaded flatbed trailers.....	114
Table 6.30 ESALs of empty flatbed trailers	114
Table 6.31 ESALs of Tractor with 2x8 dolly, 4x4 Steerable extendable	115
Table 6.32 ESALs of Tractor with 4x8-4x8 extending platform trailer	115
Table 6.33 ESALs of Tractor with 4x8-5x8 low extending platform trailer .	115
Table 6.34 ESALs of Tractor with 10x8 platform trailer	116
Table 6.35 Siemens 2.3 MW Unit	116
Table 6.36 Bowmans Creek Wind Farm (6.2 MW Unit)	117
Table 6.37 ESALs calculation - Siemens 2.3 MW Unit (1)	117
Table 6.38 ESALs calculation - Siemens 2.3 MW Unit (2)	117
Table 6.39 ESALs calculation - Siemens 2.3 MW Unit (3)	118
Table 6.40 ESALs calculation - Bowmans Creek Wind Farm (1)	118
Table 6.41 ESALs calculation - Bowmans Creek Wind Farm (2)	118
Table 6.42 ESALs calculation - Bowmans Creek Wind Farm (3)	119
Table 6.43 ESALs comparison of three types of wind turbine.....	119
Table 6.44 ESALs of loaded dump trucks, water trucks and concrete mixers	120
Table 6.45 ESALs of empty dump trucks, water trucks and concrete mixers	120
Table 6.46 ESALs of loaded lowbed trailers in solar fram	121

Table 6.47 ESALs of empty lowbed trailers in solar farm	121
Table 6.48 ESALs of loaded flatbed trailers in solar farm	121
Table 6.49 ESALs of empty flatbed trailers in solar farm.....	122
Table 6.50 ESALs of loaded 10x8 platform trailers	122
Table 6.51 ESALs of unladen 10x8 platform trailers	122
Table 7.1 Mechanical properties in 12 analysis periods (MPa).....	128
Table 7.2 Cohesion and Friction Angle Values for Sub-base and subgrade Materials	129
Table 7.3 Physical Characteristics of Structural Layer Materials	129
Table 7.4 Maximum active shear stresses results	131
Table 7.5 Shear failure verifications	134
Table 7.6 The configuration of defined Equivalent Single-Wheel Load.....	135
Table 7.7 Maximum active shear stresses and shear stability verifications ..	136
Table 7.8 Redefined pavement structures in solar farm	137
Table 7.9 Maximum active shear stresses results and verifications (Structure No.1)	137
Table 7.10 Maximum active shear stresses results and verifications (Structure No.2)	138
Table 7.11 Maximum active shear stresses results and verifications (Structure No.3)	138
Table 7.12 Pavement structure in fatigue and rutting design	140
Table 7.13 Mechanical properties in fatigue and rutting design (MPa)	140
Table 7.14 Parameters used in transfer functions	141
Table 7.15 Predicted fatigue and rutting damages in solar farm pavement...	142
Table 7.16 Pavement structure in fatigue and rutting design (2)	142
Table 7.17 Mechanical properties in fatigue and rutting design (MPa) (2) .	142
Table 7.18 Predicted fatigue and rutting damages in solar farm pavement...	143
Table 7.19 Mechanical properties in 12 analysis periods (MPa).....	144
Table 7.20 Maximum active shear stresses results	145
Table 7.21 Shear failure verifications – Wind farm	147
Table 7.22 The configuration of defined Equivalent Single-Wheel Load (Wind farm).....	150

Table 7.23 Shear verifications under ESWL	150
Table 7.24 Predicted fatigue and rutting damages in solar farm pavement...	151
Table 7.25 Pavement structure in fatigue and rutting design – Wind farm..	151
Table 7.26 Mechanical properties in fatigue and rutting design – Wind farm	151
Table 7.27 Predicted fatigue and rutting damages in wind farm pavement ..	151

Chapter 1

Introduction

In recent years, the development of renewable energy sources is growing at a dramatic rate worldwide, with several advantages including environmentally “green”, cost effective when compared to other sources of energy and the substantial potential to provide favorable economic benefits and create new employment. (John Scott Greene, 2013. Murat Tunç, 2012. Jolanda Prozzi, 2011). However, numerous energy development projects are typically situated in rural regions, which are accessed through farm-to-market roads. In order to have a better understanding of tender pavement design for the development and operation of renewable energy projects, such as solar and wind energy plants, some background information is briefly presented.

The most developed and significant renewable energy source—aside from hydropower—is wind power. Wind energy is also considered one of the most promising technologies in generating electricity. Windmills have been used for mechanical purposes such as pumping water and grinding grain for at least 3000 years, while the use of wind as a resource to generate electricity from wind turbine can be dated back to the late nineteenth century with Brush constructed a 12 kW DC windmill generator in the USA (Burton, 2004). Wind turbines can be used to generate power for a single building, or they can be linked to an electricity grid to distribute electricity more widely. Massive structures make up wind turbines. An example can be seen at the Whirlwind wind farm development in Floyd County (Lubbock District), Texas, USA, a typical wind turbine weighs 1245 tonnes, with a sweep diameter of 95m and a height of 129m to the top of the blade, and includes elements such as reinforced concrete foundation, tower, nacelle, rotor/blade, etc. (Cesar Quiroga et al., 2012). Moreover, grouping wind turbines together has the advantage of reducing the infrastructure facilities required for the network of collecting generated electricity, these wind turbine concentrations are referred to as "wind plants". Each wind plant is a sizable operation with dozens or even hundreds of wind turbines. Examples of a typical modern wind turbine and a wind plant can be seen in Figure 1.1 and 1.2.



Figure 1.1 A typical modern wind turbine (Burton, 2004)



Figure 1.2 Wind plant (Cesar Quiroga et al., 2012)

It is well known that the sun is a major source of unlimited, constant free energy (i.e., solar energy) for the planet earth. The development of solar energy is considered to be one of several main key solutions toward fulfilling a global sharply increasing electricity demand. In general, solar energy can be harnessed from the sun and converted into electrical and thermal energy by the use of two types of approach: “(a) Solar thermal technology, typically relies on parabolic concentrators to reflect direct solar radiation onto a fluid that then flows to a steam turbine that drives an electric generator; (b) Solar photovoltaic technology (PV), relies on cells constructed from semiconductor materials that directly convert sunlight into electricity” (J. Prozzi et al., 2011, 29:214).



Figure 1.3 Solar Photovoltaic Cell System (NSW, 2018)



Figure 1.4 Solar Thermal Power System (J. Prozzi et al., 2011)

1.1 Problem Statement

Wind & solar energy development projects vary from other conventional industrial activities in that they generally require the delivery of very large, heavy components that cannot be fabricated on site such as transformer, nacelle, blade, and tower sections, etc. and that cannot be transported using traditional methods due to their size and weight exceed the restrictions. Hence, Overweight/Oversize (OW/OS) vehicles carrying loads up to 125 tons (Paul W. et al., 2011) are frequently needed for assisting the movements of wind turbine and other heavy components. In comparison to ordinary trucks, OW/OS hauling units are substantially larger, heavier, and move at slower speeds and they often necessitate specific trailers and components that are assembled to fit the specifications of the OW/OS vehicles. Two examples of OW/OS vehicles employed in wind & solar energy developments are depicted in Figure 1.5 and Figure 1.6.



Source: Wind Energy Transport LLC

Figure 1.5 Turbine blade transport in wind farm



Source: FRV (2023)

Figure 1.6 Main transformer transport in solar farm

Considering the aforementioned highlighted issues, there are several concerns associated with the circulation of OW/OS vehicles in flexible pavement design. In addition to higher acceleration/deceleration forces on the roadways and turning movements at the bends, due to the heavy gross vehicle weight and slow-moving nature of OW/OS vehicles, their applications can potentially cause rapid load-induced shear failure, particularly in the subgrade and weakly bound layers.

It is worth mentioning that conventional tires (i.e., single and wide-base), are commonly used in transportation, which enables the application of existing methodologies and current procedures in pavement design to tackle crucial concerns such as pavement-tire contact pressure, pavement distress modes, and corresponding pavement response parameters.

While in the design and analysis of pavement structures, climatic condition and traffic data are two of the key elements required. Traffic can be modeled as Equivalent Single Axle Loads (ESALs) in terms of a reference axle and truck traffic spectrum according to mechanistic-empirical pavement design methods. However, reference axle varies depending on the design method in different countries, hence, remaining other conditions the same, the predicted pavement long-term functional performance could be different due to the variations of the damage caused by the passage of a reference axle and the estimated ESALs. Weather and climate attributes affect the pavement structural designs mainly due to changes in subgrade layer resilient modulus values and in asphalt complex modulus values. Therefore, there is a

pressing need to properly assess the sensitivity of the configuration of the reference axle load and climatic input in structural asphalt pavement designs.

1.2 Scope and Objectives

The final objective of this thesis is to focus on the structural design of asphalt pavements in renewable energy plants, with a particular emphasis on shear stability design, and to gain an understanding of the sensitivity of predicted pavement performance by using the mechanistic-empirical pavement design method, while taking into account climate attributes and the characteristics of different reference axles.

To this end, the following partial objectives have been conducted:

- Evaluation of the environmental and climatic effects on pavement structural design by considering three categories of analysis-periods;
- Investigation of the sensitivity in structural pavement design in terms of traffic homogenization model, with the comparison of different reference axles;
- Analysis and design of the shear stability of the subgrade and unbound layers under the traffic loads generated by the development of renewable green plants; and
- Estimates of reference traffic spectra for wind and solar farms.

1.3 Outline of The Thesis

This section outlines the overall structure of the thesis. After the introductory chapter, which presents the problem statement and research objectives, the subsequent information of this study was presented in a concise yet comprehensive manner.

- Chapter 2 presents a literature review on wind & solar energy development, three flexible pavement design methods, and environmental effects and reference axle considerations.
- Chapter 3 focuses on an investigation of the environmental effects on the predicted functional performance of flexible pavements, and in turn on the structural design.
- Chapter 4 shows an analysis of the effect of the reference axle load used in traffic modeling on structural design.
- Chapter 5 presents a design approach used to evaluate the likelihood of localized shear failure (yield) in unbound layers of asphalt pavements subjected to super-heavy load conditions following the Russian structural pavement design guide (ODN 218.046-01).
- Chapter 6 contains an assessment of reference traffic spectra for a wind and a solar farm, respectively.
- Chapter 7 focuses on the structural design of asphalt pavement sections for a proposed wind energy plant and a proposed solar energy plant, with emphasis on the shear stability, fatigue cracking, and rutting deformation.
- Chapter 8 provides a summary of the study, along with its major findings and conclusions, as well as recommendations for future research initiatives.

- Annex contains a structural design procedure internally developed at Politecnico di Torino for the structural design of asphalt pavements in renewable energy plants.

Chapter 2

Literature Review

2.1 Impact of Green Energy Development on Road Infrastructure

The present literature review in this section provides a summary of existing literature pertaining to the impact of OW/OS truck traffic, associated with the development of solar and wind energy projects, on pavement infrastructures.

The wind energy industry primarily affects the transportation system during the installation of wind turbines. Once installation is complete, the use of OW/OS vehicles is generally limited to turbine maintenance and/or replacement. The primary impact of the wind energy development on transportation infrastructure is related to the movement of turbines and other heavy components from manufacturing plants to the installation sites. Unlike the renewable fuels industry (e.g., Bio-Fuel production), wind energy does not typically generate ongoing heavy vehicle traffic. However, the magnitude and dimension of the vehicles utilized for hauling wind turbine components associated with significant frequency of the traffic during construction phase can present a challenge when these large and heavy vehicles travel on the FM roadway system (K. Gkritza et al., 2011). When assessing the impact of solar energy development on pavement infrastructure, it is important to note that, similarly to wind energy development, solar energy projects generally do not generate ongoing heavy vehicle traffic during the operational phase. However, the use of OW/OS hauling units during the construction phase is typically limited to the transportation of a few large-scale components, such as transformers, electrical buildings, and cranes required for installation (NWS, 2022). When compared to wind farm development, the limited magnitude and frequency of traffic loads associated with solar energy projects suggests that the impact on roadways is generally minimal and may even be negligible in the case of smaller-scale solar farms.

2.1.1 Wind and Solar Energy Development

Wind energy development

According to The European Wind Energy Association (Wind Europe, 2023), the installed wind power capacity in Europe had been steadily increasing from 2013 to 2022, with the capacity doubling from approximately 125 GW in 2013 to 255 GW in 2022 with 88% (225 GW) located onshore and the remaining 12% (30 GW) installed offshore. As illustrated in Figure 2.1, the wind energy sector in Europe had shown significant growth over the period of 2013 to 2022.

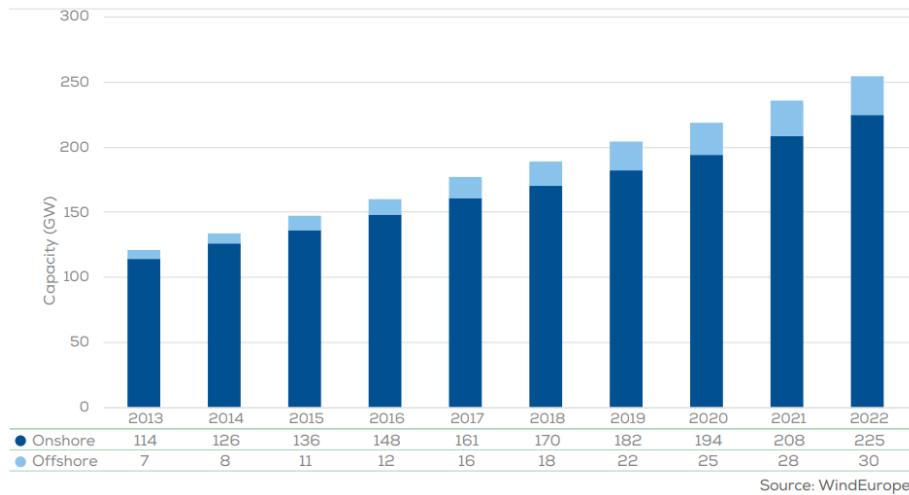
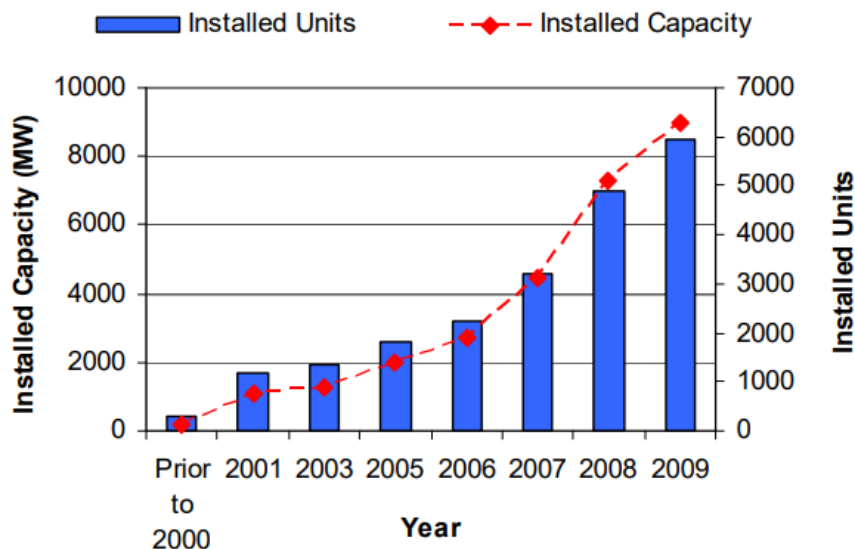


Figure 2.1 Installed wind power capacity in Europe, 2013 - 2022

In 2011, Prozzi et al. studied wind development in Texas, USA. The study found that the state of Texas achieved significant growth in wind energy production, increasing from 180 MW in 1999 to 8948 MW in June 2009, surpassing the original objective of the legislation Senate Bill 20 to install 5880 MW of capacity by 2015. Figure 2.2 illustrates the substantial growth of the wind energy sector in the state during the first decade of the 21st century.



Source: Prozzi et al. (2011)

Figure 2.2 Wind Capacity Growth in Texas, 2000 - 2009

It is foreseeable that the development of wind energy will continue to increase in the future. This is exemplified by the five-year WindEurope Market Outlook for new

wind installations (Wind Europe, 2023), as depicted in Figure 2.3. The outlook includes the 2030 Targets Scenario, which outlines the theoretical installation rate required to meet the REPowerEU target of 440 GW in EU-27, as well as the 2030 targets of non-EU countries such as the UK (50 GW), Turkey (18 GW), Norway (12 GW), and Switzerland (0.2 GW). The installation rate is expected to start at the same level as 2022 and reach its peak growth rate between 2026 and 2027, demonstrating the anticipated increase in installations in the coming years. To meet these targets, Europe will need to install 145 GW of wind energy capacity over the next five years. Within the EU, 117 GW will need to be installed between 2023-27 to remain on track towards meeting the REPowerEU targets for 2030.

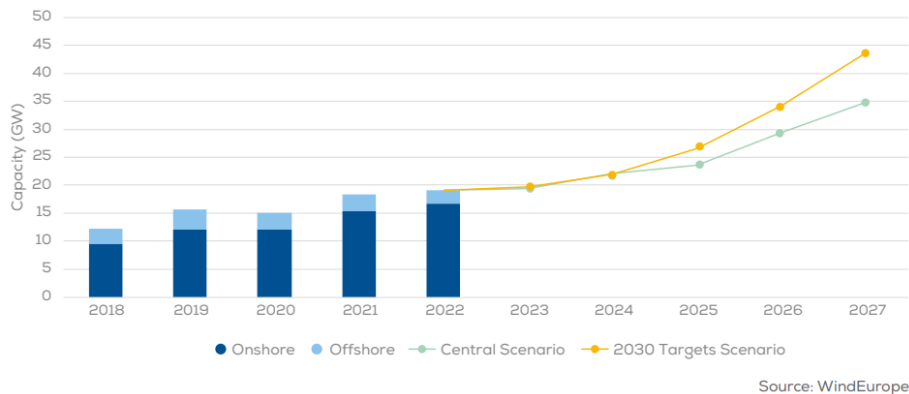


Figure 2.3 Outlook of new installations in Europe – WindEurope’s scenarios

Solar energy development

In 2022, SolarPower Europe reported that the 27 EU member states witnessed the connection of 41.4 GW of new solar PV capacity to the grids, representing a 47% increase compared to 2021, when the solar market had already expanded by 41% to 28.1 GW, making it the most substantial growth in history. The same pattern applies to cumulative installed solar power capacities, which has been rapidly growing in European Union over the past two decades, particularly in the last five years from 2017 to 2022, with capacity more than doubling from roughly 100 GW in 2017 to 208.9 GW in 2022 (SolarPower Europe, 2022). The significant growth of the wind energy sector in the EU over the past two decades is seen in Figure 2.4.

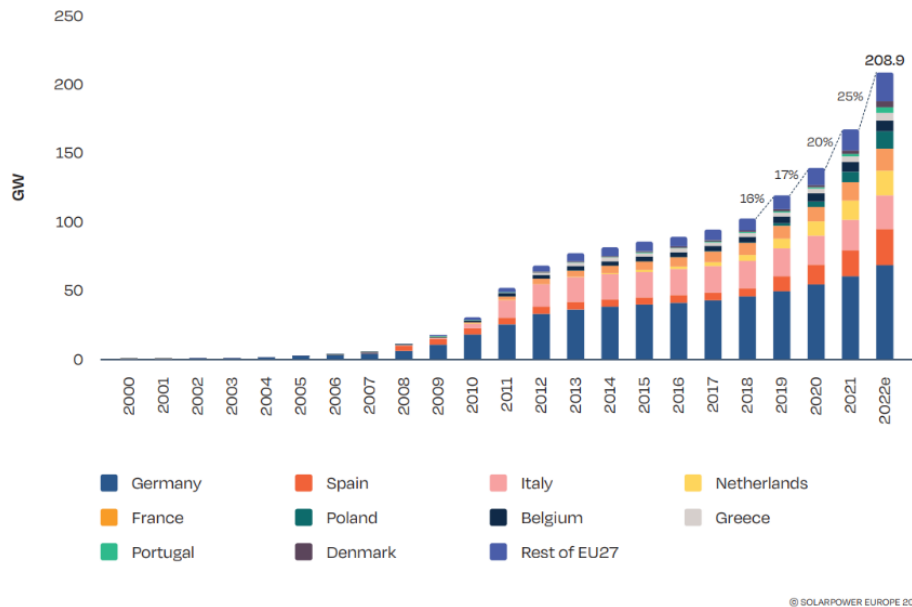


Figure 2.4 EU-27 cumulative solar PV installed capacity, 2000 - 2022

Globally, the growth trend is also evident in the cumulative installed solar PV capacity, which has seen a tremendous rise from 2000 to 2021, with a remarkable increase of 22% to reach 940.0 GW by the end of 2021, up from 772.2 GW in 2020 (SolarPower Europe, 2022a) (Fig. 2.5).

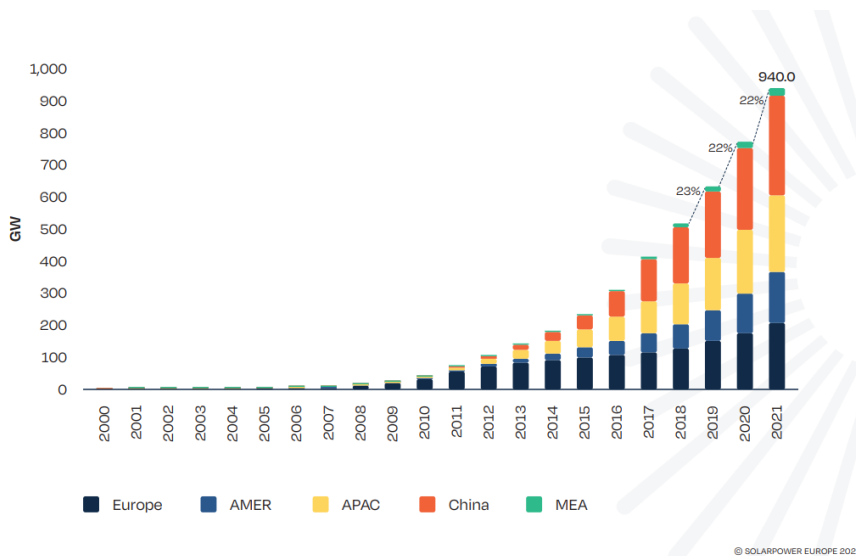


Figure 2.5 Total solar PV installed capacity globally, 2000 - 2021

The SolarPower Europe has analyzed the progress of all EU Member States towards achieving their 2030 solar targets as stated in their National Energy and Climate Plans (NECPs) of 355 GW, and the EU Commission's REPowerEU strategy of 750 GW. The analysis assessed the key measures taken by each country to promote solar deployment, including the level of ambition of solar targets, the policy framework for prosumers, and actions to ease administrative procedures, amongst others. The 2022 EU Market Outlook predicts that the total solar fleet in the EU will

increase from 209 GW installed at the end of 2022, to about 400 GW in 2025, and 920 GW in 2030, according to the Medium Scenario long-term outlook (see Fig. 2.6). Notably, the 2030 Medium Scenario outlook is almost three times higher than the aggregate PV capacity goal of 335 GW set in NECPs. Even more strikingly, the 920 GW total market size now surpasses the REPowerEU strategy's 750 GW solar target by 170 GW. The SolarPower Europe model predicts that improved policy and investment conditions will enable the EU to meet its REPowerEU solar target by 2029 and exceed the target by 24% by the end of the decade.

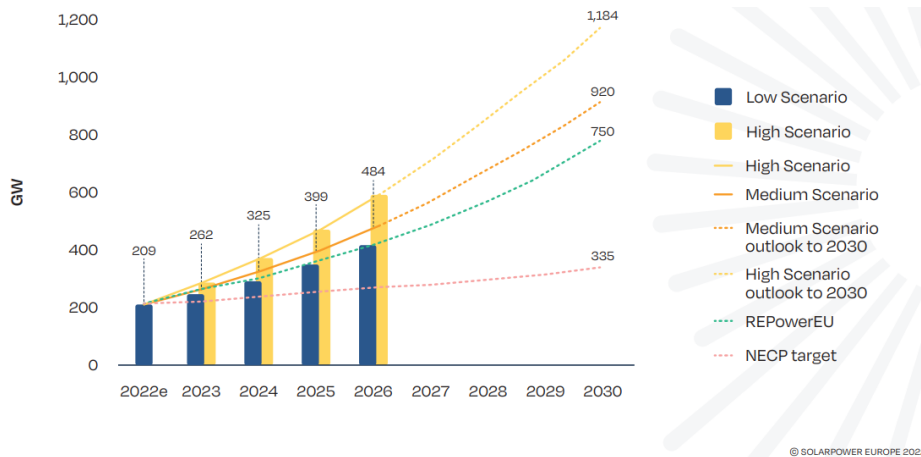


Figure 2.6 EU-27 total solar PV market scenarios, 2022 - 2030

More widely, the world will see very strong demand for solar energy in the five years starting from 2022 to 2026, due to its ability to provide a price hedge and energy security at both the national and individual levels. The 2022 Global Market Outlook published by SolarPower Europe predicts that, under the Medium Scenario, the global solar power fleet will reach 2368 GW by the end of 2026. Under optimal conditions, the world could operate PV generation plant capacities as large as 2707 GW by the same year. Over the next five years, the Medium Scenario projects that the total global installed PV generation capacity will surpass the following milestones: 1.1 (Trillion Watts) TW in 2022, 1.4 TW in 2023, 1.7 TW in 2024, 2.0 TW in 2025, and 2.3 TW in 2026. Figure 2.7 illustrates the expected trend of the cumulative global total solar capacity growth over the next five years.

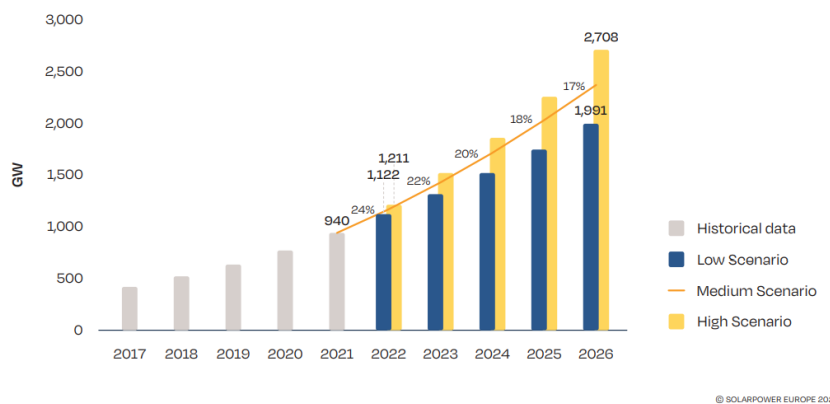


Figure 2.7 Global total solar PV market scenarios, 2022 - 2026

2.1.2 Wind and Solar Farms Associated Truck Traffic

Wind farms

Prozzi et al. conducted a study in 2011 on the wind energy supply chain in the Texas transportation system, where they evaluated the trucks that were used for transporting wind turbine components. The report assessed that 10 trips were needed to construct a single wind turbine, as per the Texas OS/OW database. The researchers then selected 97 permitted routes randomly from the Texas Department of Transportation (TxDOT) OS/OW database for further analysis. Based on their findings, they concluded that the traffic associated with wind turbine construction can be classified into several key stages.

- site preparation;
- windmill foundation installation;
- windmill delivery and assembly; and
- underground cable installation.

Table 2.1 indicates that around 336 truck trips are necessary for site preparation and the construction of the wind turbine foundation for a single wind turbine. Based on the report and the presented data, the construction of a 200-unit wind farm would result in 67200 one-way truck trips over a 6- to 12-month construction period. Additionally, Table 2.2 shows that the assembly of a wind turbine typically requires eight OW/OS components to be transported to the site.

Table 2.1 Estimates of truck traffic associated with site preparation for a single typical wind turbine (Siemens 2.3 MW)

	Quantity (t)	Truck hauls
Concrete for pad	600 - 710	35
Base material for pad	5000	223
Materials for service Road	1000 - 2250	78
Total projected truck trips		336

Source: Prozzi et al. (2011)

Table 2.2 OW/OS Vehicles used for Moving Wind Turbine (1.5 MW) Components

Vehicle	Component	Width (m)	Length (m)	Height (m)	Weight (t)
13-axle Schnabel w/ 6-axle steerable dolly	Tower, Main-Section	4.6	53.9	4.8 - 5.0	105.2
11-axle Schnabel w/ 6-axle steerable dolly	Tower, Mid-Section	4.6	48.7	4.8 - 5.0	90.3

Schnabel Dolly	Tower, Mid-Section	4.3	37.2	4.4	58.4
5-Axle Stretch Lowboy	Tower, Mid-Section	4.3	31.7	5.3	50.8
Dolly Trailer	Tower, Top-Section	3.5	37.8	4.3	41.3
13 Axle Trailer	Nacelle	3.8	36.7	4.4	98.9
Specialized Blade Trailer	Blade	2.6	53.3	4.4	35.4
Double Drop Trailer	Hub/Rotor	3.4	15.2	4.3	38.6

Source: Prozzi et al. (2011)

Solar farms

Similar to wind farms, according to the available sector literature reports (NSW, 2021; NSW, 2022; NSW, 2022a; FRV, 2020), the construction phase is expected to generate the largest volume of truck traffic over the lifetime of solar project. The traffic generated during the construction of solar plants can be categorized into several primary tasks as follows.

- site set-up and access roads;
- reticulation cable trenching and installation;
- solar panels installation;
- substation and operational & maintenance building construction; and
- transmission line and switchyard construction.

The total number of hauling trucks required for solar farm construction roughly ranges from 2500 to 6000 for every 100 MW(AC) capacity, depending on the estimation methodologies, site characteristics and scheduled construction periods, etc. As demonstrated in Table 2.3, which presents typical examples of the total one-way heavy vehicle movements and estimated construction periods associated with three modern solar PV farms, namely, Oxley Solar Farm (NWS, 2022a), Metz Solar Farm (FRV, 2020), and Daroobalgie Solar Farm (NWS, 2022).

Table 2.3 Examples of the estimates of truck traffic associated with solar farms construction

	Total one-way heavy vehicle movements	Construction schedual
215MW (AC) Oxley Solar Farm	9767	12 – 18 months
115 MW (AC) Metz Solar Farm	3237	12 – 13 months
100 MW (AC) Daroobalgie Solar Farm	5775	14 months

The traffic generated typically includes a range of vehicles such as low loader trailers, semi-trailers, standard trucks, concrete agitators, b-double trucks, utility vehicles, trailers, and waste collection trucks. In addition, OW/OS vehicles are also necessary for delivering superheavy components such as transformers and cranes (Table 2.4). The number of one-way OW/OS hauling units required for solar farm construction is typically fewer than 10, depending on the size of the solar farm in question.

Table 2.4 OW/OS Vehicles used for moving heavy components in solar farms

Vehicle	Component	Weight (t)
9-axle Schnabel w/ 3-axle steerable dolly	Transformer	80
5-Axle Stretch Lowboy	120-t Capacity Crane	60

Source: FRV (2020a), Manitowoc (2023)

The detailed analysis and corresponding estimation methods used to determine the reference traffic spectra for both wind and solar farms can be found in Chapter 6.

2.1.3 The Traffic Impacts Induced by Green Energy Development on Roadways

In 2011, Prozzi et al. conducted a comprehensive study examining the impact of wind energy industry-generated traffic on the Texas transportation system. The researchers used the Mechanical-Empirical Pavement Design Guide (MEPDG) software from the American Association of State Highway and Transportation Officials (AASHTO) to assess the service life of pavement cross-sections. To evaluate the pavements, the team of researchers used rutting depth, longitudinal cracking, and alligator cracking as distress measures. According to their findings, heavy component movement on US highways caused roughly 5% additional damage from a rutting perspective, while damage was estimated at 1% and 8% for Interstate and State Highways, respectively. The resulting additional damage led to a reduction in service life of 1.9% for Interstate highways, 15.2% for US highways, and 20.2% for state highways. The authors found that the average overall reduction in pavement service life was 9.1%.

While Steven D. Schrock et al. noticed in 2014 that minor damage has been observed on the interstate-type highways, as these are typically designed to accommodate large quantities of heavy and/or superheavy vehicles. Hence, the research team conducted a study, focused solely on lower-volume two-lane roadways, of how the wind farm associated truck traffic impacts the roadways in Kansas. Using both the International Roughness Index (IRI) and total rutting as measures of deterioration, the research team employed the AASHTO's MEPDG software to assess the reduction in useful life of five typical Kansas two-lane rural roadways caused by additional truck traffic generated from two wind farm sizes: a large wind farm with 262 turbines and a median-sized wind farm in Kansas with 67 turbines. The researchers discovered that the additional wind farm traffic did not cause a reduction in pavement life of more than 2 years when evaluating roughness on the IRI scale. However, significant reductions in service life were observed when the total rutting depth reached 0.75 inches. Depending on the different roadway models analyzed, this level of rutting was reached between 9 and 19 years earlier, reflecting a 35 to 50 percent shortening of pavement life.

Given the relatively low magnitude and frequency of traffic loads associated with solar energy projects, the impact on roadways is generally considered to be minimal and may even be negligible for smaller-scale solar farms.

2.2 Flexible Pavement Design Methodologies

“Design is a topic that is very hard to tie down. The problem is that there is never a unique solution to any given problem. When planning construction of a major pavement, there will always be a number of different options as to which combinations of materials to use” (Thom, 2008, p.179).

“Prior to the early 1920s, the thickness of pavement was based purely on experience. The same thickness was used for a section of highway even though widely different soils were encountered. As experience was gained throughout the years, various methods were developed by different agencies for determining the thickness of pavement required. Methods of flexible pavement design can be classified into five categories: empirical method with or without a soil strength test, limiting shear failure method, limiting deflection method, regression method based on pavement performance or road test, and mechanistic–empirical method” (Huang, 2004, p.1).

To define broad methods to pavement design, the technical terms “empirical design,” “mechanistic design” and “mechanistic-empirical design” are widely employed. The major aspects of these design approaches are detailed in the following subsections.

2.2.1 Empirical design

Huang (2004) stated that “although pavement design has gradually evolved from art to science, empiricism still plays an important role even up to the present day” (p. 1).

In pavement design, the environmental influences, traffic loading and mechanical characteristics of materials of the pavement structure are typically the physical causes which induce the pavement responses including stresses, strains, and deflections within a pavement structure. The empirical design method determines the relationships between the pavement responses and performance for designing pavements in the future relies only on a large number of design inputs and outcomes of experimentation, experience or combination of both. These correlations typically lack a solid theoretical basis, however, when it is too challenging to specify theoretically the cause-and-response links of a phenomena, empirical methodologies are frequently adopted as an advisable approach. In regard to the disadvantages of an empirical method, Huang (2004) debunks that “empirical method can be applied only to a given set of environmental, material, and loading conditions. If these conditions are changed, the design is no longer valid, and a new method must be developed through trial and error to be conformant to the new conditions” (p. 2).

One of the most commonly used empirical methods for designing new and rehabilitated pavements is the AASHTO 1993 Guide for Design of Pavement Structures. This method (AASHTO, 1993) was developed initially based on the AASHO Road Test conducted in Ottawa, Illinois, USA, in 1956-62, but then

complemented by decades of subsequent information to incorporate considerable adjustments based on theory and experience, allowing the design equations to be employed under a set of environmental, material, and loading conditions other than the AASHTO Road Test.

The AASHTO design equation for flexible pavements is a regression relationship between traffic loading in terms of the number of equivalent single axle load applications, the strength of the underlying subgrade, pavement structural capacity, drainage, design reliability, and functional performance measured in terms of serviceability index.

Although the AASHTO empirical method (AASHTO, 1993) has been and continues to be widely utilized for pavement structure design worldwide, it does have considerable limitations, principally because the regression relationships used are empirical and the AASHTO Road Test only covers a small range of situations. For instance, Bayomy et al. (2012) found the empirical AASHTO 1993 pavement design method has several limitations regarding climate, traffic, subgrade, pavement materials and pavement performance. These limitations the authors present are 1) The road was tested for a duration of only two years, whereas most pavements are designed to last for 20 years or more. 2) There was a limited range of properties for the asphalt concrete mixture. 3) The properties of the unbound base and subbase materials were also limited. 4) The subgrade type used was only one, i.e., A-6 soil. 5) The AASHTO 1993 design method is based on data from a single climatic location, namely Ottawa, Illinois. 6) The design criteria adopted by this method raised concerns as it is based on the concept of pavement severability, which is subjectively evaluated. 7) The number of traffic repetitions, axle weights and configurations, truck class, and tire pressures were limited. 8) The pavement performance cannot be predicted using this design method.

2.2.2 Mechanistic Design

In comparison to empirical methods, the mechanistic design method is at the opposite extreme of the spectrum of the pavement design. Mechanistic methods have the potential to forecast different forms of distress, increase design reliability, and make it possible to extrapolate from limited field-performance and laboratory-experiment data.

The mechanistic design method relies on mechanical theories to connect pavement structural performances with traffic loading and environmental factors. In mechanistic design method, the behavior of the pavement materials and pavement layer thickness can be properly predicted and designed based on pavement theoretical stress, strain, or deflection analysis. The multilayer elastic theory that Burmister developed in the 1940s to compute stresses, strains, and deflections in pavement constructions is a key development of the analytically based method for the design of flexible pavements (D. M. Burmister, 1945). These solutions exposed the engineering community to the crucial idea of considering the pavement as a layered system, even if they were restricted to conditions at layer interfaces and the findings were often given in graphical representation. Barry R. et al. (2006) addressed the elasticity-based solutions by Boussinesq, Burmister, and Westergaard were an important first step toward a theoretical description of the pavement response under load. However, the

linearly elastic material behavior assumption underlying these solutions means that they will be unable to predict the nonlinear and inelastic cracking, permanent deformation, and other distresses of interest in pavement systems. This requires far more sophisticated material models and analytical tools. Much progress has been made in recent years on isolated pieces of the mechanistic performance prediction problem. The Strategic Highway Research Program during the early 1990s made an ambitious but, ultimately, unsuccessful attempt at a fully mechanistic performance system for flexible pavements. To be fair, the problem is extremely complex, nonetheless, the reality is that a fully mechanistic design approach for pavement design does not yet exist. Some empirical information and relationships are still required to relate theory to the real world of pavement performance.

Researchers such as Duncan (1986) used finite-element analyses to model pavement response in the late 1960s. In 1969, Dehlen presented a significant finding that demonstrated how the nonlinear response of granular materials could be adequately accounted for in pavement studies. In order to represent the nonlinear characteristics of material behavior, the finite-element approach has become more and more popular for modeling pavement reaction. Modern finite-element technology has certain advantages over layered-elastic and viscoelastic solutions because it allows for more flexibility in simulating the nonlinear response characteristics of all the components that comprise the pavement section.

2.2.3 Mechanistic-Empirical Design Method

A mechanistic-empirical method to pavement design, as the name implies, is a hybrid method includes characteristics of both the mechanistic and empirical methodologies. The mechanistic component uses mechanics-based methods to calculate the responses of the pavement, including stresses, strains, and deflections imposed by traffic loads and environmental factors. Subsequently, these pavement responses are correlated to the functional performance of the pavement using empirical distress models, for example, a linearly elastic mechanics-based model can be applied to compute the vertical compressive strains at the top of a subgrade layer as a result of applied traffic load, this strain is then empirically connected to the accumulation of permanent deformation.

Huang (1993) found that Kerkhoven and Dormon (1953) were the first to suggest the use of the vertical compressive strain on the surface of the subgrade as a failure criterion for permanent deformation in flexible pavement structures, while Saal and Pell (1960) recommended the use of horizontal tensile strain at the bottom of the AC layer to minimize fatigue cracking. Huang's book also demonstrates the use of vertical compressive strain to control permanent deformation is based on the fact that plastic strains are proportional to elastic strains in paving materials. Thus, by limiting the elastic strains on the subgrade, the elastic strains in other components above the subgrade will also be controlled, hence, the magnitude of permanent deformation on the pavement surface will be controlled in turn. These two criteria have since been first adopted by Shell Petroleum International (Claussen et al., 1977) and by the Asphalt Institute (Shook et al., 1982) in their mechanistic-empirical design methods. While the latest advancement in mechanistic-empirical design method is *Mechanistic-Empirical Pavement Design Guide* (MEPDG), realized under the 1-37A project of National Cooperative Highway Research Program (NCHRP) and published by

AASHTO. The MEPDG provides numerous significant enhancements over the current pavement design guides and represents a new paradigm in pavement design.

2.3 Environmental Effects Overview

The structural design of flexible pavement is impacted by weather and climate characteristics, which cause fluctuations in the modulus values of pavement layers and the progression of deterioration conditions (W. Uddin et al., 2019).

In 2015, M.R. Mohd Hasan et al. studied the effects of mean annual precipitation and temperature on the flexible pavement distresses using the Mechanistic-Empirical Pavement Design Guide (MEPDG) software. The researchers collected the climate conditions for 76 locations from 13 states across the USA for future study. Longitudinal cracking, transverse cracking, alligator cracking, asphalt concrete rutting and total pavement permanent deformation were the measures of distress used to conduct the pavements analysis. Using the MEPDG software, the researchers found that the presence of longitudinal cracking in flexible pavement is notably impacted by both temperature and precipitation. On the other hand, the mean annual temperature plays a significant role in the development of alligator cracking, transverse cracking, and permanent deformation of flexible pavement.

Likewise, in 2019, a case study was conducted by W. Uddin et al. to analyze the sensitivity of climate effects on the mechanistic-empirical design of asphalt highway pavement. The study focused on variations in seasonal monthly pavement temperature and moisture content changes within the pavement layers. In the sensitivity study, the Pavement Design System for New and Existing Asphalt Pavements (PADAP) software was utilized to calculate seasonal modulus values based on monthly climatological data for five selected years. This allowed the team of researchers to determine the future Structural Number (SN) and overlay thickness required for future cumulative Equivalent Single Axle Loads (ESALs) over 40 years. The study revealed that monthly changes in layer modulus values have a notable impact on the mechanistic-empirical pavement design and predictions of condition deterioration model equations. It was further observed that if a design method relies on a single set of design modulus values without considering the climate impacts and appropriate nonlinear corrections for unbound layers, it can significantly limit the accuracy of the output from the use of mechanistic-empirical design methods.

In a more in-depth study, Zuo et al. (2007) investigated the impact of temperature averaging intervals (monthly, daily, and hourly) and variations in water content on the estimated pavement life, using the finite element analysis (FEA using ABAQUS). They collected two years of hourly averaged mid-depth Asphalt Concrete (AC) temperature data and water contents for the base layer and subgrade in Tennessee. The pavement life expectancy was determined by applying Miner's hypothesis to combine traffic-induced strains and probabilities of occurrence for different environmental conditions. The findings of the research indicated that the length of the temperature averaging interval has a significant impact on pavement life estimates. It was observed that the estimated pavement life increases as the length of the averaging interval increases. Monthly temperature averages used in pavement designs were found to neglect significant damage caused during brief periods of high temperature, which can lead to unconservative designs. Furthermore, the study showed that

seasonal variation in water content in the subgrade layer has a significant effect on the studied pavement systems.

2.4 Review of Reference Axle Used in Different Pavement Design Standards

Despite the extensive use of linear elastic models in flexible pavement design and performance evaluation in recent years (Huang, 2004), design methodologies and parameters still differ among countries (P. Pereira et al., 2017). One key element required for the design and analysis of pavement structures is traffic data, where traffic is defined by axle load spectra, measured in terms of the number of Equivalent Single Axle Loads (ESAL), as defined in the 2008 AASHTO design guide (AASHTO, 2008). The ESAL employs the Equivalent Axle Load Factor (EALF) concept, the EALF determines the ratio between the damage induced by a generic axle passing on a roadway and that caused by a reference axle traversing on the same road. This ratio is applied to homogenize the traffic spectrum that consists of different load and axle types into a reference axle.

However, there are considerable differences among different pavement design methodologies in converting the ESAL and the reference axle characteristics used in traffic homogenization. (P. Pereira et al., 2017). The present review of reference axle shows the various types of reference axle used in the main flexible pavement design methods, such as the French pavement design method (LCPC, 1994), the AASHTO pavement design procedure (AASHTO, 2008), the UK mechanistic-empirical pavement design method (Powell et al., 1984), and Chinese asphalt pavement design method (JTJ D50, 2006) (Table 2.5).

Table 2.5 Comparison of different reference axles

Design method	Reference axle type	Wheel load (kN)	Contact pressure (MPa)	Dual wheel spacing (m)
Franch	Single axle of 130 kN with dual tyres	32.5	0.66	0.375
AASHTO	Single axle of 80 kN with dual tyres	20.0	0.70	0.350
English	Single axle of 80 kN with single tyre	40.0	0.56	/
Chinese	Single axle of 100 kN with dual tyres	25.0	0.70	0.320

In the present study, the reference axles of a 120 kN single axle with twin wheels and 800 kPa inflation pressure according to the maximum values set by current Italian legislation (Highway Code) (Bellagamba G et al, 2010), and a single axle of 80 kN with dual tires as defined in the 2008 AASHTO mechanistic-empirical design method were considered in the analysis of the influence of the model used for traffic homogenization (see Chap. 4).

2.5 The Effect of Different Load Configurations on Shear Stability Analysis

The potential for rapid load-induced shear failure caused by super-heavy loads is a significant concern for structural pavement design. While the load/axle configuration of the superheavy load models play an important role in the definition of the potential of shear failure.

In 1995, Jooste and Fernando conducted a study to analyze how various load configurations impact the predicted stress state and yield function of shear failure in pavement layers. In their study, three different models of a typical superheavy load configuration were used to model pavement response (Fig. 2.8). The 3D Mohr-Coulomb yield criterion were used to evaluate the potential for pavement damage at the bottom of the asphalt layer, both at the top and bottom of the base layer, and at the top of the subgrade of two pavement structures (i.e., a thin and a thick pavement with typical material properties). Eight horizontal positions at each evaluated depth the stresses and yield functions were evaluated.

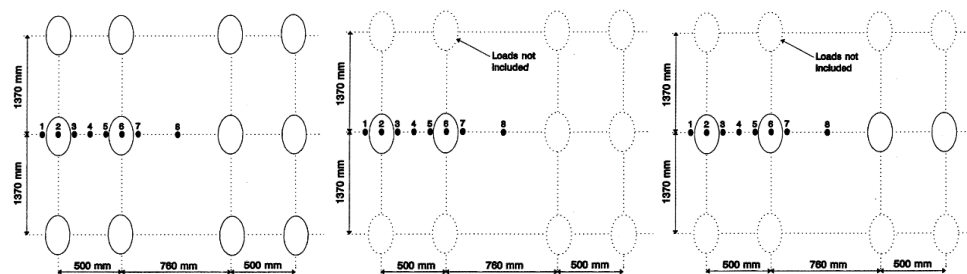


Figure 2.8 Triple, single axle load and dual wheel load (From left to right) (Jooste and Fernando, 1995)

The findings of the research indicated that the stress states and yield function values predicted with the consideration of the two simplified load configurations (i.e., single axle load and dual wheel load) were quite similar to those of the more intricate three axle assembly and the critical yield functions were typically predicted at the same locations in all three load configurations. Moreover, the authors suggested that simplifying a multiple axle load configuration to a single axle or a dual wheel load results in a more conservative prediction of the yield function. This is because, in most cases, the two simplified load configurations predicted stress states that were more critical in terms of the potential for shear failure. Based on these findings, the researchers concluded that, for the load and pavement configurations analyzed, a dual wheel load can sufficiently simulate the pavement stress conditions under a multiple axle load.

Later, Chen et al. (2013) presented a case study of the pavement structural analysis to evaluate the damage potential of a rapid, load-induced shear failure to a superheavy load movement with over 17638 kN loads and a critical axle load of 510 kN on a flexible pavement. The potential for pavement failure under the superheavy load was assessed using finite element software and a layered elastic analysis program (BISAR) with the 3D Mohr-Coulomb yield criterion. To simulate the load of the transport vehicles, the researchers chose three different axle load configurations: the

single-line load model, the three-line load model, and the five-line load model (see Fig. 2.9). Within the pavement section, pavement responses at 35 critical locations (see Fig. 2.10) were evaluated for each load model, with five horizontal analysis positions at each of the seven vertical evaluated depths (i.e., at the top, middle, and bottom of both the asphalt and the base layers, and at the top of the subgrade).

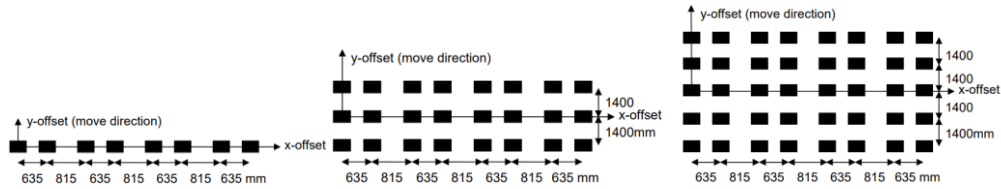


Figure 2.9 Single-, three-, and five-line load model (From left to right) (Chen et al., 2013)

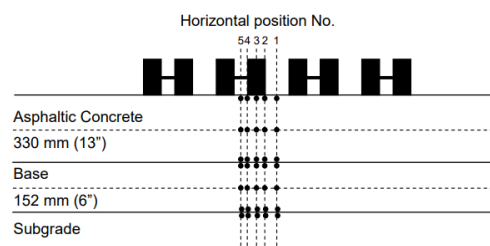


Figure 2.10 Evaluated locations within pavement (Chen et al., 2013)

The study demonstrated that, even though the three- and five-line load models are more representative of the actual load situation, the single-line load model is much more practical to use, and its results are generally more conservative in pavement structural analysis. Moreover, the impact of multiple lines on pavement performance could be assessed in terms of repeated use of the single-line load. Additionally, the research team discovered that, for the load and pavement structure simulated, the bottom of the base layer is more prone to reaching the full shear capacity of the pavement under superheavy loads.

Therefore, in the present study, the effects of load configurations on shear stability of pavement layers will not be further analyzed. Instead, based on the results of literature survey presented in this section, the half-axle load model will be adopted in the future analysis regarding shear stability.

Chapter 3

Effects of Climate Variation on Structural Analysis

The performance and structural capacity of pavements are directly impacted by changes in the environment, with pavement temperature and subgrade moisture content being two key climatic factors in pavement design. While the dynamic modulus of Hot Mix Asphalt (HMA) is sensitive to temperature fluctuations, the resilient modulus of the subgrade is impacted by moisture content levels. Therefore, it is crucial to consider the effects of both factors during the design process of flexible pavements. This chapter aimed to investigate the environmental effects on the predicted functional performance of flexible pavements. To achieve this, a mechanistic-empirical pavement design method was used to conduct a sensitivity analysis of predicted functional performance for asphalt pavements. By varying the averaging interval of obtained monthly climate data (i.e., air temperature and precipitation), the climate effects were studied parametrically on the pavement performance.

3.1 Effects of Moisture Variation on Subgrade Resilient Modulus

One of the key material characteristics for designing and evaluating pavements is the resilient modulus (M_R) of subgrade soils. Among the various factors (e.g., dry density, loading rate, temperature, etc.) that influence the prediction of M_R , the moisture content in subgrade soils is a particularly important variable. Any fluctuations in the moisture content in the subgrade soils can affect the M_R of the subgrade, and consequently, on the structural design of the pavement. Under repeated loading, granular materials that are experienced with excessive moisture content develop excess pore-water pressure. This pressure buildup can cause a reduction in the effective stress within the material, resulting in a decrease in both its strength and stiffness (Fredrick Lekarp et al., 2000).

The significance of the effects of moisture content on predicted M_R values can vary depending on the type of subgrade soil within a given range of moisture content.

Sand soils are generally only slightly affected by changes in moisture content, with the capillary effect between sand particles slightly increasing the normal stress and friction between particles at low water contents. However, as moisture content increases, the lubrication between particles becomes more significant, which ultimately overcomes the capillary effect and leads to a decrease in strength of the materials (Gilbert Baladi et al., 2009). In the case of unbound aggregates with a high proportion of fines and a well-graded distribution, the effects of moisture content have a more significant impact on its resilient behavior. This is due to such materials tending to retain water in their pores more readily than uniformly graded materials, which allow water to drain freely (Raad et al. 1992). Hence, in order to emphasize the effect of climate on structural design, the current study focused exclusively on the analysis of fine-grained subgrade soils.

The modulus of elasticity of the subgrade soil can be expressed as resilient modulus M_R . In the laboratory, soil specimens generally undergo triaxial cyclical load testing. For a specific soil type, the M_R values can be determined by dividing the imposed deviatoric stress, σ_d (the discrepancy between axial and lateral stresses), by the recoverable axial strain (ϵ_r) of the soil specimen. The M_R is mathematically represented as follows (Eq. 3.1):

$$M_R = \frac{\sigma_d}{\epsilon_r} \quad 3.1$$

The laboratory determination of the resilient modulus values of roadbed soil can be conducted in accordance with standard test methods such as AASHTO T307, "Determining the Resilient Modulus of Soil and Aggregate Materials".

The resilient modulus must be assigned with values consistent with the stress states, thickening and moisture conditions expected in service during the various periods of analysis. Effects resulting from changes in load application rates or temperature are not considered. The drainage in the subgrade layer is expected to be adequately designed by construction practices, hence the saturated conditions induced by the effects of excessive water within the subgrade soil is not considered in the structural analysis.

The pavement design guide, formulated through the NCHRP Project 1-37A, advocates the use of Equation 3.2 to compute M_R values in a mechanistic-empirical approach. The resilient modulus is represented as a function that depends on both bulk stress (θ) and octahedral shear stress (τ_{oct}). By employing linear or nonlinear regression analyses, the model's nonlinear elastic coefficients and exponents can be determined, allowing it to align with laboratory-derived M_R test data.

$$M_R = k_1 \cdot P_a \cdot \left(\frac{\theta}{P_a}\right)^{k_2} \cdot \left(\frac{\tau_{oct}}{P_a} + 1\right)^{k_3} \quad 3.2$$

Where:

- M_R is resilient modulus of subgrade soil, in MPa.

- θ is bulk stress, in MPa, $\theta = \sigma_1 + \sigma_2 + \sigma_3$, σ_1 is the major principal stress, σ_2 is the intermediate principal stress, σ_3 is the minor principal stress;
- τ_{oct} the octahedral shear stress, in MPa,

$$\tau_{oct} = \frac{1}{3} \cdot \sqrt{(\sigma_1 - \sigma_2)^2 + (\sigma_1 - \sigma_3)^2 + (\sigma_2 - \sigma_3)^2};$$
- P_a is the atmospheric pressure, in MPa;
- k_1, k_2, k_3 are the regression constants.

In order to take into account the seasonal variation of resilient modulus, the effective value of the resilient modulus of the roadbed soil is recommended. The equivalent resilient modulus, which results in the same level of pavement damage as the seasonal moduli, is known as the effective resilient modulus. The amount of damage, expressed as the relative damage, u_r , is determined by the following an empirical relationship for each of seasonal M_R values (Eq. 3.3).

$$u_r = 1.18 \cdot 10^8 \cdot M_R^{-2.32} \quad 3.3$$

By averaging the u_r values across all seasons, the mean relative damage (u_f) is determined. Following this, the effective subgrade resilient modulus (M_{REff}) can be calculated using the Equation 3.4:

$$M_{REff} = 3015 \cdot u_f^{-0.431} \quad 3.4$$

3.1.1 M_R –Moisture Model

The mechanistic-empirical pavement design guide, formulated through the National Cooperative Highway Research Program (NCHRP) Project 1-37A, recommends the use of a mathematical model established based on specimens compacted at optimum conditions (i.e., optimum moisture content and maximum dry density) to estimate the changes in resilient modulus values of subgrade soils in response to variations in moisture content:

$$\log\left(\frac{M_R}{M_{Ropt}}\right) = a + \frac{b - a}{1 + e^{\ln\left(\frac{-b}{a}\right) + k_m \cdot (S - S_{opt})}} \quad 3.5$$

Where:

- M_{Ropt} is the resilient modulus at optimum moisture content, in MPa;
- M_R is the resilient modulus at given moisture content, in MPa;
- $\frac{M_R}{M_{Ropt}}$ is resilient modulus ratio;
- a is the minimum value of $\log\left(\frac{M_R}{M_{Ropt}}\right)$;
- b is the maximum value of $\log\left(\frac{M_R}{M_{Ropt}}\right)$;

- k_m is regression parameter;
- S is the degree of saturation, expressed in decimals;
- S_{opt} is the degree of saturation at optimum moisture content, expressed in decimals;
- $(S - S_{opt})$ is variation in the degree of saturation, expressed in decimals.

The degree of saturation can be calculated using the Equation 3.6 (G. Baladi et al., 2009):

$$S = \frac{G_s \cdot (MC/100) \cdot \gamma_d}{G_s \cdot \gamma_w - \gamma_d} \quad 3.6$$

Where:

- S is degree of saturation, expressed as decimals;
- MC is moisture content (%);
- G_s is specific gravity of the soil solid;
- γ_d is dry unit weight of the sample (kN/m^3);
- γ_w is unit weight of water, $=9.81 kN/m^3$.

3.2 Effects of Temperature Variation on HMA Dynamic Modulus

Hot mix asphalt concrete is composed of two primary components: aggregate and asphalt binder. The mechanical properties of asphaltic materials are significantly influenced by temperature due to their viscoelastic and thermoplastic characteristics. Under given loading rates, hot mix asphalt concrete exhibits lower stiffness at high temperatures compared to low temperatures due to the more viscous behavior of asphalt materials. This behavior is characterized by ductile fracture and high values of phase angle δ , resulting in increased flow susceptibility. Consequently, the lower stiffness at high temperatures is likely lead to inadequate protection of the underlying base and subgrade layers against overstressing. Conversely, at low acting temperatures, the asphalt materials display a more elastic behavior, characterized by brittle fracture and low phase angle δ values, providing higher stress-carrying capacity without undergoing flow.

The Master Curve of dynamic modulus can be used to predict the stiffness of asphalt mixtures at a given temperature and frequency/loading time. The mechanistic-empirical pavement design guide, developed as part of NCHRP Project 1-37A, suggests employing the dynamic modulus ($|E^*|$) of asphalt mixtures as a crucial parameter in the flexible pavement design process. Asphalt mixtures exhibit varying $|E^*|$ values depending on the temperature (T) and loading frequencies (f). As the frequency increases, the $|E^*|$ value rises, while it decreases with an increase in temperature. The $|E^*|$ Master Curve describes how the moduli of asphalt mixtures change with temperature and frequency/loading time.

The Master Curve of an asphalt mixture enables the comparison of data across wide ranges of frequencies or temperatures. To generate Master Curves, the Time Temperature Superposition (TTS) principle is employed. By utilizing the TTS principle, the $|E^*|$ data collected at various temperatures and frequencies can be horizontally shifted relative to a reference temperature or frequency to generate a single $|E^*|$ Master Curve. After shifting, the new frequency corresponding to the dynamic modulus is referred to as the reduced frequency (f_R), which can be defined by the following Equation 3.7:

$$f_R = f \cdot \alpha_T(T) \quad 3.7$$

Where:

- f is the frequency of load application;
- $\alpha_T(T)$ is the shift factor coefficient for a given temperature T , indicating the amount of shift required at that temperature. During the shifting process, the shift factors at each temperature are adjusted until a satisfactory sigmoid fit is achieved across all temperatures.

The shift factor can be defined using the following equation:

$$\log(\alpha(T)) = a_1 \cdot (T^2 - T_{ref}^2) + a_2 \cdot (T - T_{ref}) \quad 3.8$$

Where:

- a_1, a_2 are the polynomial coefficients;
- T is a given temperature, in $^{\circ}\text{C}$;
- T_{ref} is the reference temperature, in $^{\circ}\text{C}$.

Equation 3.9 represents the complex modulus $|E^*|$ as a sigmoidal function in the form of the Master Curve:

$$\log(|E^*|) = b_1 + \frac{b_2}{1 + e^{(-b_3 - b_4 \cdot \log(f_R))}} \quad 3.9$$

Where:

- $|E^*|$ is complex modulus of asphalt mixture, in MPa.
- $b_1, b_2, b_3,$ and b_4 are sigmoid fitting coefficients describing the shape of the sigmoidal function;
- f_R is reduced frequency.

During the generation of the Master Curve, the $|E^*|$ data at a specific temperature is not shifted, and this temperature is designated as the reference temperature (T_{Ref}). This implies that the shift factor coefficient for T_{Ref} is equal to 1. In this study, the reference temperature selected is equal to 21°C . Moreover, to determine the

temperature of asphalt materials for pavement structural design purposes, the collected air temperature must be converted by considering the intermediate depth of each layer, as described in Annex.

3.3 Analysis Procedure

To illustrate the effects of climate on structural design, with a particular focus on the mechanical properties of asphalt layers and subgrade soil influenced by monthly variations in temperature and precipitation. The monthly climate data (i.e., air temperature and precipitation) were collected and averaged over a ten-year analysis period. The mechanical properties of all the pavement layers were calculated based on the obtained climate data and distributed into three categories of multiple analysis periods, which were defined according to three averaging intervals, namely, three analysis periods, five analysis periods and twelve analyses periods. This study incorporated some key data and essential models along with associated parameters from the existing literature (described below) to describe the moisture-precipitation relationship in subgrade soils, the mechanistic properties of HMA, and to estimate the subgrade resilient moduli at different moisture contents. The pavement section being analyzed in this study consisted of a HMA surface course, a HMA base course and an unbound granular subbase placed above the subgrade soil. The impact of climate variations on structural analysis was then evaluated by assessing the damages in terms of fatigue cracking and rutting in pavement.

3.3.1 Site Description

The precipitation-moisture model used in this study was assembled based on a case study conducted by A. Ahmed et al. in 2008. The model was developed using real-time field monitoring data derived from an asphalt pavement located in Kaufman County, North Texas to simulate subgrade moisture content. For the current study, the Kaufman County site was considered to investigate the impact of climate on pavement structural design. Soil samples collected from the site had a particle size distribution consisting of over 85% clay, indicating the presence of very fine subgrade soil. According to the Unified Soil Classification System (USCS), the soil at site was classified as high plastic clay (CH). The liquid limit of the soil samples was tested ranged from 50% to 64%, while the plasticity index ranged from 28% to 42%. The specific gravity of the soil ranged between 2.68 and 2.72, with an average of 2.70. The optimum moisture content was determined to be 22% as obtained from a standard proctor test (A. Ahmed et al., 2008).

In order to obtain the subgrade resilient moduli using the M_R -moisture model based on the moisture data obtained from a selected local precipitation-moisture model developed in Kaufman County, it was necessary to ensure the consistency in the soil type and corresponding physical properties between the sites where the parameters for these two models were derived. Therefore, the parameters used in the M_R -moisture model were adopted based on the findings of a previous study conducted by Khoury Naji in 2016. In that study, the soil of interest under investigation was identified as CH (or A-7 Group according to the AASHTO soil classification system), with a liquid limit of 55%, a plastic limit of 30%, optimum moisture content of 23.5% and a dry unit weight obtained as 15 kN/m³.

3.3.2 Traffic Data Collection and Analysis

To predict the pavement performance with a mechanistic-empirical design method in this study, it was necessary to homogenize the various types of vehicles and axle loads into a standard 80-kN axle load by using Equivalent Axle Load Factor (EALF) (see Annex), and to model the total mixed traffic in terms of the standard axle load over the analysis period as assumed to be 20 years. The total number of passes of the standard axle load during the design period, which was defined as the Equivalent Single-Axle Load (ESAL), calculated by the following equation:

$$ESAL = AADT \cdot T \cdot T_f \cdot G \cdot D \cdot L \cdot 365 \cdot Y \quad 3.10$$

Where:

- AADT is annual average daily traffic;
- T is the percentage of trucks in AADT;
- T_f is truck factor;
- Y is the design period in years;
- G is growth factor, $= \frac{(1+0.01 \cdot r)^Y - 1}{0.01 \cdot r}$ (r is annual growth rate, expressed in percentage);
- L is lane distribution factor (%) that depends on the number of lanes in each direction, assumed equal to 100 for one lane, 80-100 for two lanes, and 60-80 for three lanes;
- D is the directional distribution factor, assumed to be 0.5.

In the present study, the traffic data collected from Michigan Department of Transportation on US-127 highway (Fig. 3.1) in Clinton, Michigan was adopted in the analysis. The studied US-127 highway cross-section consisted of two lanes in each direction, with an annual average two-way daily traffic of 22843 in 2009 and a growth rate of 4%. The lane distribution factor was assumed to be 100% in the study in order to be conservative.



Source: Michigan Department of Transportation

Figure 3.1 US-127 highway in Clinton, Michigan

The Transportation Data Management System operated by the Michigan Department of Transportation was accessed to obtain the traffic class distribution from the April 2009 Classification Report, with the 13-category classification of vehicles defined according to Federal Highway Administration. The distribution of traffic in classes is shown in Table 3.1.

Table 3.1 Traffic classification

	Class 1	Class 2	Class 3	Class 4	Class 5	Class 6	Class 7
Percentage	0.2%	72.8%	17.4%	0.1%	0.8%	0.4%	0.1%
	Class 8	Class 9	Class 10	Class 11	Class 12	Class 13	
Percentage	1.0%	5.2%	0.7%	0.2%	0.1%	1.0%	

In order to calculate the EALF of each vehicle class and the total truck factor, the axle loads of each vehicle class were assumed based on the existing sector literature (Table 3.2). It is noted that vehicles falling into classes 1 to 3 (e.g., Motorcycles and Passenger cars) were not included in the design process, since it is believed that the vehicles in these classes generally with lower mass and can therefore be neglected in the structural design process, as they are typically considered to have a negligible impact on the pavement structures. Consequently, based on the assumed axle loads of each vehicle class and the corresponding coefficients according to different configurations of axles (see Annex), the EALF of each axle was calculated (as shown in Table 3.3).

Table 3.2 Axle loads definition

Class Group	Class Definition	Axle Description	Axle load (kN)
4	Buses	Front single axle	44
		Rear single axle	36
5	Two-Axle, Six-Tire, Single-Unit Trucks	Front single axle	53
		Rear single axle	80
6	Three-Axle Single-Unit Trucks	Front single axle	71
		Rear tandem axle	142
7	Four or More Axle Single-Unit Trucks	Front single axle	71
		Rear tandem axle	231
8	Four or Fewer Axle Single-Trailer Trucks	Front single axle	71
		Rear single axle	80
		Rear tandem axle	160
9	Five-Axle Single-Trailer Trucks	Front single axle	71
		Rear tandem axle	142
		Rear tandem axle	160
10	Six or More Axle Single-Trailer Trucks	Front single axle	71
		Rear tandem axle	160
		Rear tridem axle	231
11	Multi-Trailer Trucks	Front single axle	80

		Rear single axle	98
		Rear tandem axle	98
		Front single axle	98
		Rear single axle	107
12	Six-Axle Multi-Trailer Trucks	Front single axle	80
		Rear single axle	98
		Rear tandem axle	142
		Front single axle	98
		Rear single axle	107
13	Seven or More Axle Multi-Trailer Trucks	Front single axle	80
		Rear tandem axle	142
		Rear tandem axle	160
		Front single axle	98
		Rear single axle	107

Table 3.3 Equivalent Axle Load Factor Calculation

Class Group	Axle Description	Axle load (kN)	EALF by Axles	EALF by Classes
4	Front single axle	44	$= 1 \cdot \left(\frac{44}{80}\right)^4 = 0.10$	0.14
	Rear single axle	36	$= 1 \cdot \left(\frac{36}{80}\right)^4 = 0.04$	
5	Front single axle	53	$= 1 \cdot \left(\frac{53}{80}\right)^4 = 0.20$	1.20
	Rear single axle	80	$= 1 \cdot \left(\frac{80}{80}\right)^4 = 1.00$	
6	Front single axle	71	$= 1 \cdot \left(\frac{71}{80}\right)^4 = 0.63$	1.50
	Rear tandem axle	142	$= 2 \cdot 0.7 \cdot \left(\frac{142/2}{80}\right)^4 = 0.88$	
7	Front single axle	71	$= 1 \cdot \left(\frac{71}{80}\right)^4 = 0.63$	6.74
	Rear tandem axle	231	$= 2 \cdot 0.7 \cdot \left(\frac{231/2}{80}\right)^4 = 6.11$	
8	Front single axle	71	$= 1 \cdot \left(\frac{71}{80}\right)^4 = 0.63$	3.03
	Rear single axle	80	$= 1 \cdot \left(\frac{80}{80}\right)^4 = 1.00$	
	Rear tandem axle	160	$= 2 \cdot 0.7 \cdot \left(\frac{160/2}{80}\right)^4 = 1.40$	
9	Front single axle	71	$= 1 \cdot \left(\frac{71}{80}\right)^4 = 0.63$	2.91
	Rear tandem axle	142	$= 2 \cdot 0.7 \cdot \left(\frac{142/2}{80}\right)^4 = 0.88$	
	Rear tandem axle	160	$= 2 \cdot 0.7 \cdot \left(\frac{160/2}{80}\right)^4 = 1.40$	
10	Front single axle	71	$= 1 \cdot \left(\frac{71}{80}\right)^4 = 0.63$	3.45

	Rear tandem axle	160	$= 2 \cdot 0.7 \cdot \left(\frac{160/2}{80}\right)^4 = 1.40$	
	Rear tridem axle	231	$= 3 \cdot 0.55 \cdot \left(\frac{231/3}{80}\right)^4 = 1.42$	
11	Front single axle	80	$= 1 \cdot \left(\frac{80}{80}\right)^4 = 1.00$	8.85
	Rear single axle	98	$= 1 \cdot \left(\frac{98}{80}\right)^4 = 2.24$	
	Rear tandem axle	98	$= 2 \cdot 0.7 \cdot \left(\frac{98/2}{80}\right)^4 = 0.20$	
	Front single axle	98	$= 1 \cdot \left(\frac{98}{80}\right)^4 = 2.24$	
	Rear single axle	107	$= 1 \cdot \left(\frac{107}{80}\right)^4 = 3.17$	
12	Front single axle	80	$= 1 \cdot \left(\frac{80}{80}\right)^4 = 1.00$	9.53
	Rear single axle	98	$= 1 \cdot \left(\frac{98}{80}\right)^4 = 2.24$	
	Rear tandem axle	142	$= 2 \cdot 0.7 \cdot \left(\frac{142/2}{80}\right)^4 = 0.88$	
	Front single axle	98	$= 1 \cdot \left(\frac{98}{80}\right)^4 = 2.24$	
	Rear single axle	107	$= 1 \cdot \left(\frac{107}{80}\right)^4 = 3.17$	
13	Front single axle	80	$= 1 \cdot \left(\frac{80}{80}\right)^4 = 1.00$	8.69
	Rear tandem axle	142	$= 2 \cdot 0.7 \cdot \left(\frac{142/2}{80}\right)^4 = 0.88$	
	Rear tandem axle	160	$= 2 \cdot 0.7 \cdot \left(\frac{160/2}{80}\right)^4 = 1.40$	
	Front single axle	98	$= 1 \cdot \left(\frac{98}{80}\right)^4 = 2.24$	
	Rear single axle	107	$= 1 \cdot \left(\frac{107}{80}\right)^4 = 3.17$	

Subsequently, the total truck factor can be defined as follows:

$$\begin{aligned}
 T_f &= 0.14 \cdot 0.1\% + 1.20 \cdot 0.8\% + 1.50 \cdot 0.4\% + 6.74 \cdot 0.1\% + 3.0 \cdot 1.0\% \\
 &\quad + 2.91 \cdot 5.2\% + 3.45 \cdot 0.7\% + 8.85 \cdot 0.2\% + 9.53 \cdot 0.1\% + 8.69 \cdot 1.0\% \\
 &= 3.56
 \end{aligned}$$

Lastly, based on the presented data above, the total number of passes of the vehicles, expressed in terms of an 80-kN standard single axle within one lane of the carriageway during the service life of 20 years, was determined as follows:

$$\begin{aligned}
 ESAL &= AADT \cdot T \cdot T_f \cdot G \cdot D \cdot L \cdot 365 \cdot Y \\
 &= 22843 \cdot 9.57\% \cdot 3.56 \cdot \frac{(1 + 0.01 \cdot 4)^{20} - 1}{0.01 \cdot 4} \cdot 0.5 \cdot 100\% \cdot 365 \cdot 20 \\
 &= 42341673
 \end{aligned}$$

3.3.3 Climatic Statistics

In this sub-section, the climatic statistics were presented with the collection of the climate data (i.e., air temperature and precipitation) over a 10-year span in Kaufman County, North Texas. Subsequently, the air temperature data was converted to mid-depth pavement temperature in each HMA layer, while precipitation data was used to predict subgrade soil moisture content. Finally, the mid-depth pavement temperatures and moisture contents were presented according to each month of the year.

3.3.3.1 Climatic Data Collection

By accessing the Iowa Environmental Mesonet of Iowa State University, the monthly precipitation and air temperature data spanning 10 years from 2002 to 2011 were collected from a climate station located in Kaufman County, North Texas. The collected climate data, alongside the calculated monthly averages for the 10-year period, are reported in Tables 3.4 and 3.5.

Table 3.4 Monthly precipitation, 2002-2011

Monthly Precipitation (mm)												
	Jan.	Feb.	Mar.	Apr.	May.	Jun.	Jul.	Aug.	Sep.	Oct.	Nov.	Dec.
2002	42.4	40.9	81.5	73.9	153.9	18.0	124.7	120.4	73.2	165.1	8.1	143.8
2003	9.1	121.9	48.5	46.5	78.0	85.9	38.6	70.4	93.7	51.6	20.3	3.8
2004	49.5	163.6	46.0	174.8	111.0	176.0	64.8	77.2	9.1	81.3	99.3	25.4
2005	131.3	41.2	70.1	87.6	57.4	8.9	121.9	22.4	58.4	15.5	84.8	11.4
2006	108.0	67.3	125.0	55.1	40.9	35.1	34.5	80.8	58.4	77.0	30.7	124.5
2007	138.2	37.3	222.0	20.1	255.3	203.0	132.8	145.3	131.8	49.3	46.2	85.1
2008	41.9	48.3	162.1	89.7	95.8	60.7	4.1	84.3	70.1	51.8	133.4	31.0
2009	42.9	26.9	145.3	83.8	155.5	146.3	86.4	95.5	186.4	327.4	51.6	72.9
2010	110.7	71.1	123.4	65.5	50.3	66.3	48.8	87.1	100.3	37.1	65.0	28.2
2011	81.8	54.9	12.4	43.9	128.8	83.8	0.0	9.1	35.6	64.8	38.4	150.9
Avg.	75.6	67.3	103.6	74.1	112.7	88.4	65.7	79.2	81.7	92.1	57.8	67.7

Table 3.5 Monthly air temperature, 2002-2011

Monthly Air Temperature (°C)												
	Jan.	Feb.	Mar.	Apr.	May.	Jun.	Jul.	Aug.	Sep.	Oct.	Nov.	Dec.
2002	7.1	7.3	11.0	19.6	21.9	25.9	27.6	28.1	24.6	18.0	11.1	8.5
2003	6.1	7.4	12.1	17.6	23.1	25.1	28.3	29.1	23.0	19.5	15.3	8.9
2004	8.6	6.8	15.7	17.7	22.3	25.5	26.8	26.1	24.5	21.4	13.9	8.4
2005	9.3	10.6	12.7	17.0	21.5	27.5	28.0	29.1	27.6	18.4	15.1	7.3
2006	11.4	8.5	15.1	20.8	23.0	27.0	29.2	30.5	24.0	18.5	13.7	9.7
2007	4.6	7.6	16.8	15.2	22.2	25.3	26.3	28.3	25.2	19.8	14.9	8.6
2008	5.7	10.1	13.5	17.1	22.3	27.3	28.9	28.1	22.9	17.8	13.3	7.7
2009	6.8	12.2	13.6	16.1	21.4	26.8	28.8	27.9	23.6	16.7	14.6	5.6
2010	5.6	4.9	11.1	17.7	23.3	28.0	28.7	30.5	25.6	18.8	13.4	8.2

2011	5.0	7.6	14.8	19.5	21.5	29.0	31.4	32.9	26.0	19.0	13.6	7.8
Avg.	7.0	8.3	13.6	17.8	22.3	26.7	28.4	29.1	24.7	18.8	13.9	8.1

3.3.3.2 Estimation of Subgrade Moisture Contents and Pavement Temperatures

Moisture contents

To estimate the fluctuations of moisture content in subgrade soils, both of the seasonal and temporal variations associated with climatic factors such as precipitation need to be incorporated. In the present study, a real-time moisture model developed by Asif Ahmed et al. in 2018 was assembled, which was developed based on the collected moisture and rainfall data on site with multiple soil moisture sensors installed beneath the pavement structures in the subgrade at variable depth up to 2.4m for a consecutive period of two years. The model incorporates both seasonal and temporal variations of moisture by solving a first-degree Fourier series under the assumptions made of a homogeneous subgrade soil layer, without considering moisture evaporation. The model was further validated by the authors with the in-situ measured data, which showed that the outputs of the model were accurate within a 90% confidence level. Furthermore, comparisons made with previous studies by the team of researchers demonstrated that the model could successfully capture both seasonal and temporal variations. Based on the authors' overall analysis, moisture contents in the subgrade at site can be predicted using Equation 3.11. It should be noted that various models may yield varying results, with some models amplifying the seasonal and temporal variation of moisture content, while some others may dampen these fluctuations. However, an exhaustive study of the many available models for predicting moisture content is beyond the scope of this study.

$$MC = a_0 + a_1 \cdot \cos(x \cdot w) + b_1 \cdot \sin(x \cdot w) + 1.39 + 0.09014 \cdot P \quad 3.11$$

Where:

- MC is volumetric moisture content (%);
- a_0, a_1, b_1 are regression parameters, estimated to be 17.2825, -0.46828 and 0.5417, respectively;
- w is angular frequency, is set to $2\pi/365$ as 1 year of data was used to develop the model;
- x is the number of days starting from April 1st, ranging from 1 to 365;
- P is precipitation, expressed in mm.

Based on the processed rainfall data presented earlier and the moisture model selected, the 10-year average monthly moisture contents can be calculated (see Table 3.6).

Table 3.6 Moisture content (%)

Month	Jan.	Feb.	Mar.	Apr.	May.	Jun.	Jul.	Aug.	Sep.	Oct.	Nov.	Dec.
MC	18.2	18.3	18.6	18.6	19.1	19.4	19.5	19.6	19.4	19.0	18.5	18.3

Pavement temperatures

By knowing the average monthly air temperatures, the average pavement temperature at the mid-depth for each HMA layer can be calculated by following the design procedure as indicated in Annex. In this particular study, the HMA layers under investigation were a 4-cm HMA surface course and a 15-cm HMA base course, as illustrated as following in Section 3.3.4. Monthly mid-depth temperatures for these two HMA layers have been determined and are presented in Table 3.7.

Table 3.7 HMA layers mid-depth temperatures (°C)

Month	Jan.	Feb.	Mar.	Apr.	May.	Jun.	Jul.	Aug.	Sep.	Oct.	Nov.	Dec.
Surface course (4cm)	11.6	13.1	19.6	24.7	30.0	35.4	37.4	38.2	32.9	25.8	19.9	12.9
Base course (15cm)	11.0	12.5	18.4	23.1	28.1	33.1	34.9	35.7	30.8	24.2	18.7	12.2

3.3.4 Pavement Structure and Material Properties

In this sub-section, a pavement structure was defined, and the corresponding material properties of each layer were estimated for each month of the year.

Pavement cross section

To study the environmental effects on structural design, a pavement cross section was pre-defined with the following layers:

- A HMA surface layer measuring 4 cm depth;
- A HMA base layer measuring 15 cm depth;
- An unbound granular sub-base layer with a depth of 11 cm; and
- A homogeneous subgrade layer composed of high plastic clay (CH) soils.

Material properties

To assess the stress-strain response of the pavement under traffic loadings and in the varying environmental conditions associated with the different analysis periods, it was necessary to initially calculate material properties of the layers corresponding to each month.

HMA courses:

The mechanical properties of the HMA courses in this study were characterized by their dynamic moduli, represented as $|E^*|$, which was estimated using laboratory-derived master curves. Two types of asphalt mixtures, designated as Mix-A and Mix-B, were selected from the Michigan Department of Transportation to serve as the top and base layers in the pavement cross section, respectively. The $|E^*|$ master curves for these mixes, as determined through laboratory testing at a loading frequency of 10Hz and a reference temperature of 21°C in the Michigan Department of Transportation,

were employed in this study. The basic physical properties of Mix-A and Mix-B, as well as the corresponding master curve coefficients, are listed in Table 3.8 and Table 3.9, respectively. The volumetric binder contents of both mixes were assumed to be 12%, the Poisson's ratio of the asphalt layers was considered independent of temperature and loading rate and assumed to be 0.35.

Table 3.8 Physical properties of the asphalt mixtures

Mix type	Binder PG	Air void (%)
Mix-A	70-22P	6.80
Mix-B	58-28	7.04

Source: M. E. Kutay (2013)

Table 3.9 The coefficients of Master curves

Mix type	a ₁	a ₂	b ₁	b ₂	b ₃	b ₄
Mix-A	1.17E-04	-0.128	0.29	4.21	1.4	0.35
Mix-B	4.61E-04	-0.143	-0.52	5.09	1.24	0.31

Source: M. E. Kutay (2013)

Subsequently, following the methodology outlined in Section 3.2, the reduced frequency of the HMA layers at various loading temperatures in the pavement, as calculated previously, can be determined. Following this, the dynamic moduli of the asphalt mixtures for each month of the year can be determined by employing the master curve formula presented in Section 3.2 along with the corresponding coefficients derived from laboratory tests in the Michigan Department of Transportation. Table 3.10 presents the resulting dynamic moduli values for each month.

Table 3.10 Dynamic moduli of HMA mixtures (MPa)

Mix type	Jan.	Feb.	Mar.	Apr.	May.	Jun.	Jul.	Aug.	Sep.	Oct.	Nov.	Dec.
Mix-A	11599	10896	8098	6145	4404	3002	2576	2421	3597	5743	7970	11018
Mix-B	8584	7951	5614	4146	2938	2024	1755	1657	2406	3860	5514	8059

Subgrade:

To estimate the changes in monthly resilient modulus values of subgrade soils in response to variations in moisture content, the degree of saturation in the subgrade soils was initially calculated as reported in Table 3.11 using Equation 3.6, as detailed earlier, based on the obtained monthly subgrade moisture contents. Additionally, the specific gravity of soil solid was assumed to be 2.7, as the subgrade soil under study was classified as high plastic clay, and the considered dry unit weight of the subgrade soil of 15 kN/m³, which is consistent with a previous study of Khoury Naji that also focused on the same type of subgrade soil.

Table 3.11 Degree of saturation (S) in each month

Month	Jan.	Feb.	Mar.	Apr.	May.	Jun.	Jul.	Aug.	Sep.	Oct.	Nov.	Dec.
S	0.64	0.64	0.66	0.66	0.67	0.68	0.69	0.69	0.68	0.67	0.65	0.64

Prior to using the M_R-moisture model to estimate monthly resilient modulus at various levels of moisture content over the course of a year, it was necessary to define

the resilient modulus at the optimum moisture content (23.5%) on the site being studied. In this study, the M_R value of 62 MPa at optimum moisture content was adopted, which was determined by laboratory tests following the AASHTO T307-99 test method as part of a previous study by Khoury Naji in 2016.

Last, the monthly changes in resilient modulus values of subgrade soils resulting from variations in moisture content were determined in this study using M_R -moisture model as specified in Equation 3.5 and are reported in Table 3.13. These values were calculated based on the degree of saturation previously determined for each month, as well as the regression parameters adopted from Khoury Naji's study (Table 3.12), which exhibited a goodness of fit of 0.92. The Poisson's ratio of the subgrade soil was assumed equal to 0.35.

Table 3.12 Regression parameters used in MR-moisture model

Parameter	a	b	k_m	S_{opt}
Value	-3.786	0.400	7.457	0.828

Table 3.13 Monthly resilient modulus values of subgrade soils (MPa)

Month	Jan.	Feb.	Mar.	Apr.	May.	Jun.	Jul.	Aug.	Sep.	Oct.	Nov.	Dec.
M_R	121.3	120.5	117.6	118.0	113.7	110.9	109.6	109.2	111.1	114.2	118.4	120.6

Unbound granular mixtures:

In the case of calculating the elastic modulus for unbound granular materials (E_{MG}), a simple correlation procedure was employed with a minimal level of detail in designs. It incorporates the resilient modulus of the underlying subgrade and the thickness of the unbound granular mixture layer itself in determining elastic modulus of unbound subbase layer.

The elastic modulus of the layers in unbound granular mixture (E_{MG}) must be assigned with values consistent with the stress and thickening conditions expected in operation during the different analysis periods. For mixed granular, the effects deriving from variations in the speed of application of loads, humidity or temperature are not considered.

In this study, the design approach is characterized by a minimal level of detail for determining the values of E_{MG} , which involves assigning a value to the elastic modulus of unbound granular mixtures using Equation 3.12.

$$E_{MG} = 0.2 \cdot (h_{MG})^{0.45} \cdot E_{Supp} \quad 3.12$$

Where:

- E_{MG} is elastic modulus of the unbound granular mixture layer, expressed in MPa;
- h_{MG} is thickness of the unbound granular mixture layer, expressed in mm;
- E_{Supp} is elastic modulus of the underlying support layer, expressed in MPa.

Consequently, the elastic modulus values were estimated for each month in the course of the year and are presented in Table 3.14. The Poisson's ratio of unbound granular mixes was assumed equal to 0.30.

Table 3.14 Monthly elastic moduli of unbound subbase layer

Month	Jan.	Feb.	Mar.	Apr.	May.	Jun.	Jul.	Aug.	Sep.	Oct.	Nov.	Dec.
E_{MG}	201	200	195	196	189	184	182	181	184	189	196	200

3.3.5 Analysis Periods Definition

Followed by the definition of the mechanical properties of the pavement layers in each month of the year, and prior to defining the stress-strain responses of the pavement structure, the monthly mechanical properties of all the composed pavement layers were grouped into different analysis periods according to the defined averaging intervals, namely 12 analysis periods, five analysis periods and three analysis periods.

Twelve Analysis Periods

When to consider 12 analysis periods in assessing the effects of climate on the variations in mechanical properties of the construction materials and in turn on the structural design, each analysis period was assigned to each month of the 12 months of the year. Table 3.15 shows the mechanical properties of the pavement layers in each of the 12 analysis periods.

Table 3.15 Mechanical properties in 12 analysis periods (MPa)

Analysis period	1	2	3	4	5	6	7	8	9	10	11	12
Surface course $ E^* _1$	11599	10896	8098	6145	4404	3002	2576	2421	3597	5743	7970	11018
Base course $ E^* _2$	8584	7951	5614	4146	2938	2024	1755	1657	2406	3860	5514	8059
Subbase course E_{MG}	121	121	118	118	114	111	110	109	111	114	118	121
Subgrade M_R	201	200	195	196	189	184	182	181	184	189	196	200

Five Analysis Periods

When using three or five analysis periods, the consistency of monthly mechanical properties of the subgrade soils and that of monthly air temperatures across various months in the analysis periods was considered as a criterion for distributing each month to a particular analysis period of the moduli of subgrade-subbase and asphalt mixtures, respectively.

To define the consistency of the interested data in an analysis period, several simple steps were involved. First, the difference between the maximum and minimum values of the whole dataset was identified and divided by the number of analysis periods to obtain a "scale factor" used to define the range of each analysis period. Then, the range of the first analysis period was defined as starting from the minimum

value of the dataset and ending at the sum of the minimum value and the scale factor. Next, the range of the second analysis period was defined as the set of values that fell between the upper limit of the previous group and the sum of the scale factor and the upper limit of the previous group. This procedure was repeated for determining the range of each of all the rest analysis periods considered. Last, the data for each month was assigned to the corresponding analysis period if it falls into the previously defined range.

By following this methodology, the 12-month subgrade moduli were distributed into five analysis periods based on their respective values, and the corresponding effective resilient modulus of each analysis period was calculated using Equation 3.3 and 3.4 by considering the equivalent pavement damage. And the related subbase elastic modulus in each analysis period was subsequently calculated in accordance with the corresponding effective subgrade modulus (Table 3.16).

Table 3.16 Subgrade and subbase moduli in 5 analysis periods

No. of period	Period No.1	Period No.2	Period No.3	Period No.4	Period No.5
M_R range (MPa)	109.2-111.6	111.6-114.0	114.0-116.5	116.5-118.9	118.9-121.3
Months	Jun, Jul, Aug, Sep	May	Oct	Mar, Apr, Nov	Jan, Feb, Dec
Effective M'_R (MPa)	110.2	113.7	114.2	118.0	120.8
E'_{MG} (MPa)	182.8	188.6	189.4	195.6	200.3

In the case of HMA modulus classification of five analysis periods, the air temperatures were used as the dataset in determining the months to be included in each analysis period. Subsequently, the averaged air temperatures were converted to the mid-depth temperatures to calculate the dynamic modulus of both the top and base asphalt layers in each analysis period (Table 3.17).

Table 3.17 HMA moduli in 5 analysis periods

No. of period	Period No.1	Period No.2	Period No.3	Period No.4	Period No.5
Range of air temperature (°C)	7.0-11.4	11.4-15.8	15.8-20.2	20.2-24.7	24.7-29.1
Months	Jan, Feb, Dec	Mar, Nov	Apr, Oct	May	Jun, Jul, Aug, Sep
Surface course $ E^* _1$ (MPa)	11170	8034	5942	4404	2873
Base course $ E^* _2$ (MPa)	8195	5564	4001	2938	1942

Lastly, by incorporating the analysis periods of the subgrade-subbase moduli and asphalt mixtures moduli according to each month, the following pavement models with respect to the mechanical properties of pavement layers can be identified and employed in stress-strain analysis in the subsequent sections.

Table 3.18 Pavement material mechanical property models in five analysis periods

No. of Model	Model No.1	Model No.2	Model No.3	Model No.4	Model No.5	Model No.6
Months	Jun, Jul, Aug, Sep	May	Oct	Mar, Nov	Apr	Jan, Feb, Dec
Surface course $ E^* '_1$ (MPa)	2873	4404	5942	8034	5942	11170
Base course $ E^* '_2$ (MPa)	1942	2938	4001	5564	4001	8195
Effective M''_R (MPa)	110.2	113.7	114.2	118.0	118.0	120.8
E''_{MG} (MPa)	182.8	188.6	189.4	195.6	195.6	200.3

Three Analysis Periods

To distribute the 12-month data of modulus of each pavement layers into three analysis periods, and to subsequently form the material mechanical property models, the same procedures were followed as those used in considering five analysis periods. Table 3.19 and 3.20 reported the modulus distributions of subgrade-subbase and asphalt layers, respectively. While the pavement analysis models of the mechanical properties of the materials are presented in Table 3.21.

Table 3.19 Subgrade and subbase moduli in 3 analysis periods

No. of period	Period No.1	Period No.2	Period No.3
M_R range (MPa)	109.2-113.2	113.2-117.3	117.3-121.3
Months	Jun, Jul, Aug, Sep	May, Oct	Jan, Feb, Mar, Apr, Nov, Dec
Effective M''_R (MPa)	110.2	114.0	119.4
E''_{MG} (MPa)	182.8	189.0	197.9

Table 3.20 HMA moduli in 3 analysis periods

No. of period	Period No.1	Period No.2	Period No.3
Range of air temperature (°C)	7.0-14.4	14.4-21.7	21.7-29.1
Months	Jan, Feb, Mar, Nov, Dec	Apr, Oct	May, Jun, Jul, Aug, Sep
Surface course $ E^* ''_1$ (MPa)	9877	5942	3143
Base course $ E^* ''_2$ (MPa)	7066	4001	2114

Table 3.21 Pavement material mechanical property models in 3 analysis periods

No. of Model	Model No.1	Model No.2	Model No.3	Model No.4	Model No.5
Months	Jun, Jul, Aug, Sep	Oct	May	Jan, Feb, Mar, Nov, Dec	Apr
Surface course $ E^* ''_1$ (MPa)	3143	5942	3143	9877	5942
Base course $ E^* ''_2$ (MPa)	2114	4001	2114	7066	4001
Effective M''_R (MPa)	110.2	114.0	114.0	119.4	119.4
E''_{MG} (MPa)	182.8	189.0	189.0	197.9	197.9

3.3.6 Performances Prediction

In this section, the pavement functional performances were predicted by analyzing its resistances to structural rutting and fatigue cracking. The multi-layer elastic system was assumed as the reference structural model in predicting performances of the defined pavement structure with the materials mechanical properties evaluated in three categories of analysis-periods. Based on the structural model assumed, in the design processes, several multi-layer systems were defined according to the number of analysis periods considered. Each multi-layer system, which corresponds to a specific analysis period, was characterized with the estimated mechanical properties of the materials and the defined thicknesses of all the layers composite the pavement structure. It was assumed that all materials under consideration exhibit linear elasticity, homogeneity, and isotropy. Each layer was assumed to be infinitely extended laterally and characterized by a constant thickness, with the exception of the subgrade, which is treated as a homogeneous, infinite half-space.

The load applied to each multi-layer system was considered as the reference 80 kN axle in dual tire configuration. However, for structural analysis purposes, only the semi-axle was considered. The reference semi-axle consists of two circular loads, each with a 20 kN load, and a uniform pressure of 700 kPa. Dual spacing was assumed to be 0.35 m.

The stress-strain responses of each multi-layer system structure under loading were computed at critical depths. To predict fatigue resistance, the principal horizontal tensile strain at the bottom of the base asphalt layer was determined, with the assumption made of the top and base asphalt layers are fully bounded and considered as an integral asphalt layer in this structural analysis. The vertical compressive strain on the top of the subgrade was considered in estimating the critical response for rutting. Additionally, such responses were evaluated at three distinct transversal positions. The evaluated response points and the acting semi-axle load configuration were presented in Figure 3.2.

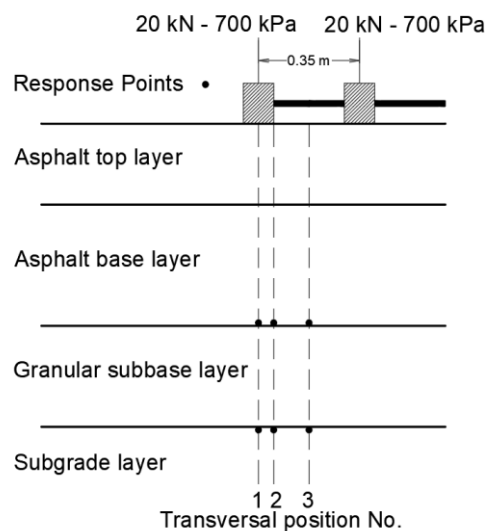


Figure 3.2 Evaluated response points within pavement

In this study, the numerical solutions of the structural response under loading at each of previously defined response points were obtained for every multi-layer elastic system in each analysis period. This was done using an open-source MATLAB[®] based code titled: Adaptive Layered Viscoelastic Analysis (ALVA) (Skar and Andersen 2020; Skar et al. 2020a). On which the multi-layer system is composed of the same number of layers of the pavement structure and each layer is described by means of an elastic modulus and a Poisson's ratio coefficient, moreover, the continuity condition is satisfied at all interfaces as full bonding between layers.

Once the principal critical responses of pavement structure in each analysis period were computed, two transfer functions were used to define the number of standard load applications that would lead to limiting conditions in terms of fatigue cracking and rutting. The Annex entailed the descriptions of these two transfer functions and the incremental damage calculations. The parameters used in each transfer function were calculated/assumed and listed in Table 3.22.

Table 3.22 Parameters used in transfer functions

Fatigue cracking	
Parameters	Values
Reliability parameter	Assumed equal to 6
Lab. shift factor	Assumed equal to 10
Self-healing shift factor	Assumed equal to 1
f_1	$f_1 = (6918 \cdot 10^{-6} \cdot (0.856 \cdot V_b + 1.08))^5$ $= (6918 \cdot 10^{-6} \cdot (0.865 \cdot 12\% + 1.08))^5$ $= 2.99 \cdot 10^{-6}$
f_2	Assumed equal to 5
f_3	Assumed equal to 1.8
Rutting	
Parameters	Values
f_4	Assumed to be $6.15 \cdot 10^{-7}$
f_5	Assumed equal to 4

It is noted that in this study, mixed traffic was represented as ESALs which was assumed to be evenly distributed in each month in the course of the year. In the case that an analysis period contains multiple months, the ESALs from each month were added together to represent the predicted traffic.

The fatigue and rutting damages resulting from each analysis period was identified by comparing the actual ESALs obtained from the traffic modeling to the predicted number of load applications resulting from transfer functions for the corresponding analysis period. Finally, the damages predicted in terms of fatigue and rutting at the end of the 20-year pavement service life in each analysis period were respectively added together as indicators to reflect the pavement performance in each category of multiple analysis periods. The numerical results are presented in Table 3.23, while Figure 3.3 illustrates the trend of the damages variation. The damages were represented as a numerical value ranging from 0 to 1, where a value of 0

indicates that the pavement did not experience any damage, and a value of 1 means a limiting condition of structural capacity in resisting fatigue cracking or rutting deformation.

Table 3.23 Predicted fatigue and rutting damages

12 Analysis Periods	
Total Fatigue Damage D_f	0.910
Total Rutting Damage D_r	0.923
5 Analysis Periods	
Total Fatigue Damage D'_f	0.906
Total Rutting Damage D'_r	0.902
3 Analysis Periods	
Total Fatigue Damage D''_f	0.888
Total Rutting Damage D''_r	0.864

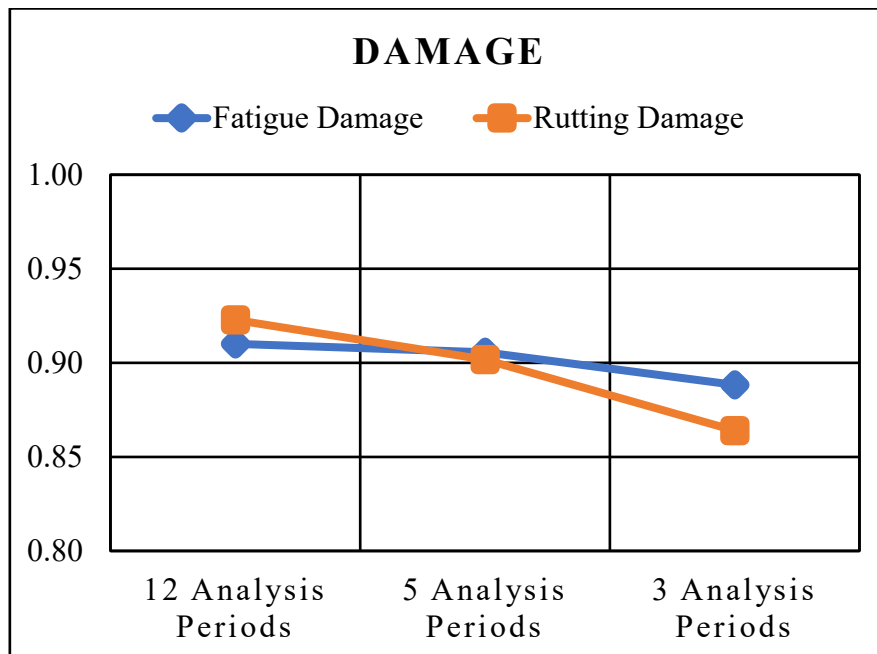


Figure 3.3 Damages comparison

By analyzing and comparing the damages in terms of fatigue cracking and rutting with the mechanical characteristics of both the asphalt layers and the subgrade soil defined in three types of multiple analysis periods assigned to structural models, the environmental effects on structure design can be assessed. The subsequent section presents an analysis of the obtained results.

3.4 Results Analysis and Discussions

This section of the study analyzed the impacts of climate variation on structural design, with a particular focus on how monthly variations in temperature and precipitation affect the mechanical characteristics of asphalt layers and subgrade soil. In all, 23 multi-layer elastic systems were analyzed across three categories of multiple

analysis periods (12 analysis periods, 5 analysis periods, and 3 analysis periods) using the ALVA computing program based on MATLAB[®].

The results showed that the length of the averaging interval used in the definition of analysis periods impacts the pavement structural design, as reflected in the estimated pavement damages at the end of its service life. It was observed that both the estimated fatigue and rutting damages decrease as the length of the averaging interval used in defining the mechanical properties of materials in an analysis period increase. For the various models and parameters considered in this study, the fatigue cracking damage was underestimated by 2% and by 6% in rutting damage when using the materials properties derived from 3 analysis periods compared to those obtained from 12 analysis periods. Consequently, it can be concluded that pavement designs based on 5 or 3 analysis periods neglect the significant damages that occur during brief periods of high temperature and/or moisture content, leading to unconservative designs, and in turn often resulting in poor performance and early deterioration of pavements. This clearly illustrated the effects of climate on structural design and emphasized the importance of using 12 analysis periods to define the mechanical properties of materials in pavement designs. Therefore, in subsequent analyses, which include examining the influences of model used for traffic homogenization, and designing pavements for wind and solar farms, the 12 analysis periods would be considered.

It is important to note that the aim of this study was to provide a general assessment of the impacts of climate (i.e., monthly variations in temperature and precipitation) on pavement design. To simplify the analysis, several readily available models and parameter values suggested by the authors of those models were used. However, if different parameter values or models were employed, it could potentially alter the results. Nonetheless, the trends presented in this study would still be applicable, even if the magnitude of the discrepancy changed.

Chapter 4

Effect of the Reference Axle Load Used in Traffic Modeling on Structural Analysis

Traffic modeling plays an important role in the design and analysis of pavement structures, the results of a traffic study, conducted for a given project period, must undergo appropriate modeling procedures to be converted into equivalent board passages, which is as known as Equivalent Single Axle Loads (ESALs). This conversion is based on the concept of the Equivalent Axle Load Factor (EALF), which determines the ratio between the damages induced by a generic axle passing on a roadway and that caused by a reference axle traveling on the same road. The EALF is applied to homogenize the traffic spectrum that consists of different loads and axle types into a reference axle. It is noted that the magnitude and configuration of the reference axle varies among different pavement design methods used to estimate ESALs, some commonly used reference axles were identified in Section 2.4 from a literature survey.

In the present study, the effect of the reference axle load used in traffic modeling on structural design was analyzed, with the use of two different reference axles, namely, a 120 kN single axle with twin wheels at a wheelbase distance of 0.375 m and 800 kPa inflation pressure, in accordance with the maximum values set by current Italian legislation (Highway Code), and a single axle of 80 kN with dual tires at a wheelbase distance of 0.35 m and 700 kPa inflation pressure as defined in the 2008 AASHTO mechanistic-empirical design method. Additionally, considering the higher magnitude of the generated traffic loads throughout construction, operational and decommissioning phases in the development of renewable energy plants compared to that of normal road traffic, the potential of using a 120 kN reference axle with different configuration and higher magnitude compared to traditionally used 80 kN standard axle in homogenizing these abnormal traffic loads was explored.

4.1 Analysis Methodology

To evaluate the influence of the model used for traffic homogenization, a mechanistic-empirical pavement design method was used in calculating the critical responses in the pavement resulting from two types of standard axles at various evaluation points, and in turn to determine the variations in fatigue cracking the rutting damages caused by the same amount of traffic loads, but homogenized to ESALs with respect to two different standard axles, while keeping other inputs such as pavement structure, material properties, etc., remaining the same.

4.1.1 Pavement Structure and Materials Properties

In this chapter, the same pavement structure and the corresponding layer materials characterized in Chapter 3 were used to maintain simplicity. As it was previously discovered that using fewer analysis periods resulted in unconservative designs, 12 analysis periods were considered in the current study and the mechanical properties of layers in each analysis period were as well taken from the previous calculations in Chapter 3.

4.1.2 Traffic Analysis

Prior to estimating the ESALs in terms of a 120 kN standard single-axle, the traffic information collected on a section of US-127 highway and the related axle loads in each class of vehicles defined in Chapter 3 were considered to be continuously used throughout this study. Some key information on traffic is listed below in Table 4.1.

Table 4.1 Key traffic information

Average annual daily traffic	Truck percentage (%)	Design period (years)	Growth factor	Lane distribution factor (%)	Directional distribution factor
22843	9.57	20	3.56	100	0.5

Subsequently, by knowing the axle loads of each vehicle, the EALF for each of vehicle classes from 4 to 9 in reference to a 120 kN single-axle was estimated in using the corresponding equations indicated in Annex with the corresponding coefficients for different configurations of axles. The resulting EALF of each axle is reported in Table 4.2.

Table 4.2 Equivalent axle load factor to 120 kN standard single-axle

Class Group	Axle Description	Axle load (kN)	EALF by Axles	EALF by Classes
4	Front single axle	44	$= 1 \cdot \left(\frac{44}{120}\right)^4 = 0.02$	0.03
	Rear single axle	36	$= 1 \cdot \left(\frac{36}{120}\right)^4 = 0.01$	
5	Front single axle	53	$= 1 \cdot \left(\frac{53}{120}\right)^4 = 0.04$	0.24
	Rear single axle	80	$= 1 \cdot \left(\frac{80}{120}\right)^4 = 0.20$	

6	Front single axle	71	$= 1 \cdot \left(\frac{71}{120}\right)^4 = 0.12$	0.29
	Rear tandem axle	142	$= 2 \cdot 0.7 \cdot \left(\frac{142/2}{120}\right)^4 = 0.17$	
7	Front single axle	71	$= 1 \cdot \left(\frac{71}{120}\right)^4 = 0.12$	1.33
	Rear tandem axle	231	$= 2 \cdot 0.7 \cdot \left(\frac{231/2}{120}\right)^4 = 1.21$	
8	Front single axle	71	$= 1 \cdot \left(\frac{71}{120}\right)^4 = 0.12$	0.60
	Rear single axle	80	$= 1 \cdot \left(\frac{80}{120}\right)^4 = 0.20$	
	Rear tandem axle	160	$= 2 \cdot 0.7 \cdot \left(\frac{160/2}{120}\right)^4 = 0.28$	
9	Front single axle	71	$= 1 \cdot \left(\frac{71}{120}\right)^4 = 0.12$	0.57
	Rear tandem axle	142	$= 2 \cdot 0.7 \cdot \left(\frac{142/2}{120}\right)^4 = 0.17$	
	Rear tandem axle	160	$= 2 \cdot 0.7 \cdot \left(\frac{160/2}{120}\right)^4 = 0.28$	
10	Front single axle	71	$= 1 \cdot \left(\frac{71}{120}\right)^4 = 0.12$	0.65
	Rear tandem axle	160	$= 2 \cdot 0.7 \cdot \left(\frac{160/2}{120}\right)^4 = 0.28$	
	Rear tridem axle	231	$= 3 \cdot 0.55 \cdot \left(\frac{231/3}{120}\right)^4 = 0.28$	
11	Front single axle	80	$= 1 \cdot \left(\frac{80}{120}\right)^4 = 0.20$	1.75
	Rear single axle	98	$= 1 \cdot \left(\frac{98}{120}\right)^4 = 0.44$	
	Rear tandem axle	98	$= 2 \cdot 0.7 \cdot \left(\frac{98/2}{120}\right)^4 = 0.04$	
	Front single axle	98	$= 1 \cdot \left(\frac{98}{120}\right)^4 = 0.44$	
	Rear single axle	107	$= 1 \cdot \left(\frac{107}{120}\right)^4 = 0.63$	
12	Front single axle	80	$= 1 \cdot \left(\frac{80}{120}\right)^4 = 0.20$	1.88
	Rear single axle	98	$= 1 \cdot \left(\frac{98}{120}\right)^4 = 0.44$	
	Rear tandem axle	142	$= 2 \cdot 0.7 \cdot \left(\frac{142/2}{120}\right)^4 = 0.17$	
	Front single axle	98	$= 1 \cdot \left(\frac{98}{120}\right)^4 = 0.44$	
	Rear single axle	107	$= 1 \cdot \left(\frac{107}{120}\right)^4 = 0.63$	
13	Front single axle	80	$= 1 \cdot \left(\frac{80}{120}\right)^4 = 0.20$	1.72
	Rear tandem axle	142	$= 2 \cdot 0.7 \cdot \left(\frac{142/2}{120}\right)^4 = 0.17$	
	Rear tandem axle	160	$= 2 \cdot 0.7 \cdot \left(\frac{160/2}{120}\right)^4 = 0.28$	
	Front single axle	98	$= 1 \cdot \left(\frac{98}{120}\right)^4 = 0.44$	

	Rear single axle	107	$= 1 \cdot \left(\frac{107}{120}\right)^4 = 0.63$	
--	------------------	-----	---	--

Consequently, the total truck factor can be calculated as follows:

$$\begin{aligned}
 T_f &= 0.03 \cdot 0.1\% + 0.24 \cdot 0.8\% + 0.29 \cdot 0.4\% + 1.33 \cdot 0.1\% + 0.60 \cdot 1.0\% \\
 &\quad + 0.57 \cdot 5.2\% + 0.65 \cdot 0.7\% + 1.75 \cdot 0.2\% + 1.88 \cdot 0.1\% + 1.72 \cdot 1.0\% \\
 &= 0.70
 \end{aligned}$$

Lastly, based on the presented data above, the total number of passes of the vehicles, represented with a 120-kN standard single axle loads within one lane of the carriageway during the service life of 20 years, was determined as follows:

$$\begin{aligned}
 ESAL &= AADT \cdot T \cdot T_f \cdot G \cdot D \cdot L \cdot 365 \cdot Y \\
 &= 22843 \cdot 9.57\% \cdot 0.70 \cdot \frac{(1 + 0.01 \cdot 4)^{20} - 1}{0.01 \cdot 4} \cdot 0.5 \cdot 100\% \cdot 365 \cdot 20 \\
 &= 8363787
 \end{aligned}$$

A significant difference was observed between the equivalent single axle loads calculated in terms of two different reference axles (120 kN and 80 kN single axles). The respective outcomes are displayed in Table 4.3.

Table 4.3 Comparison of ESALs with two reference axles

	120 kN reference single-axle	80 kN reference single-axle
ESALs	8363787	42341673

4.1.3 Critical Responses Calculation

In this section, the stress-strain responses were computed using ALVA, an open-source MATLAB[®]-based code, with the multi-layer elastic system serving as the reference structural model, as described in Chapter 3. Throughout the calculations, two sets of 12 multi-layer systems which are consistent with the number of analysis periods were defined for calculating the critical responses resulting from 120 kN and 80 kN reference single-axles, respectively. Each multi-layer system, associated with a specific analysis period, was characterized by the mechanical properties of materials estimated for that period and the defined thicknesses of the layers composing the pavement structure. The stress-strain responses of each multi-layer system structure under loading were computed at three distinct transversal positions at each of the two critical depths as described in Chapter 3 for predicting fatigue cracking and rutting resistances, respectively. The assessment response points and the applied semi-axle load configurations for two reference axles are illustrated in Figure 4.1.

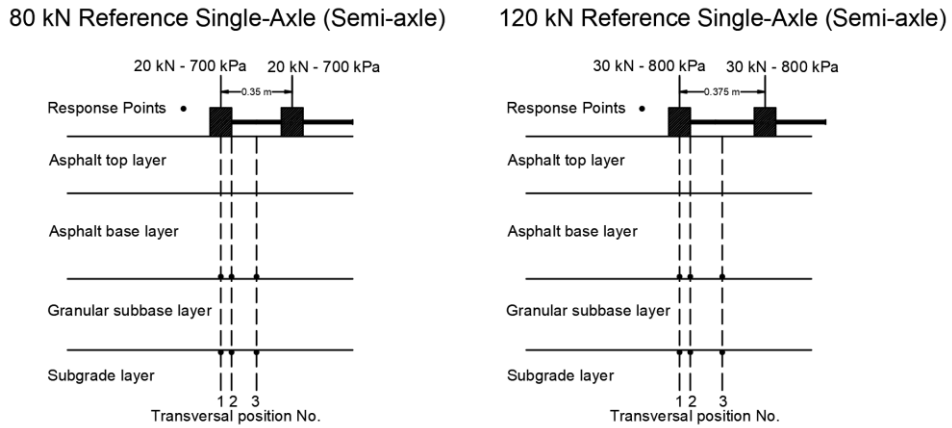


Figure 4.1 Evaluated response points and two reference axles

The numerical solutions generated by ALVA calculating program for the principal horizontal tensile strain and the principal vertical compressive strain in the pavement at their respective critical depths were obtained for each analysis period. The outputs resulting from 120 kN and 80 kN reference axle loads are listed in Table 4.4 and plotted in Figure 4.2 alongside the subgrade resilient moduli and the dynamic moduli of asphalt layers. The principal compressive strains were reported as their absolute values for the purposes of presentation.

Table 4.4 Principal response strains

Analysis period	1	2	3	4	5	6	7	8	9	10	11	12
Principal tensile strains ϵ_t (10^{-6})												
120 kN reference axle	101	106	135	165	206	258	281	290	234	174	137	105
80 kN reference axle	71	75	96	117	148	186	202	209	168	124	97	74
Principal compressive strains ϵ_c (10^{-6})												
120 kN reference axle	286	298	356	410	488	579	617	633	538	431	358	296
80 kN reference axle	197	205	247	284	340	405	433	444	376	299	248	204

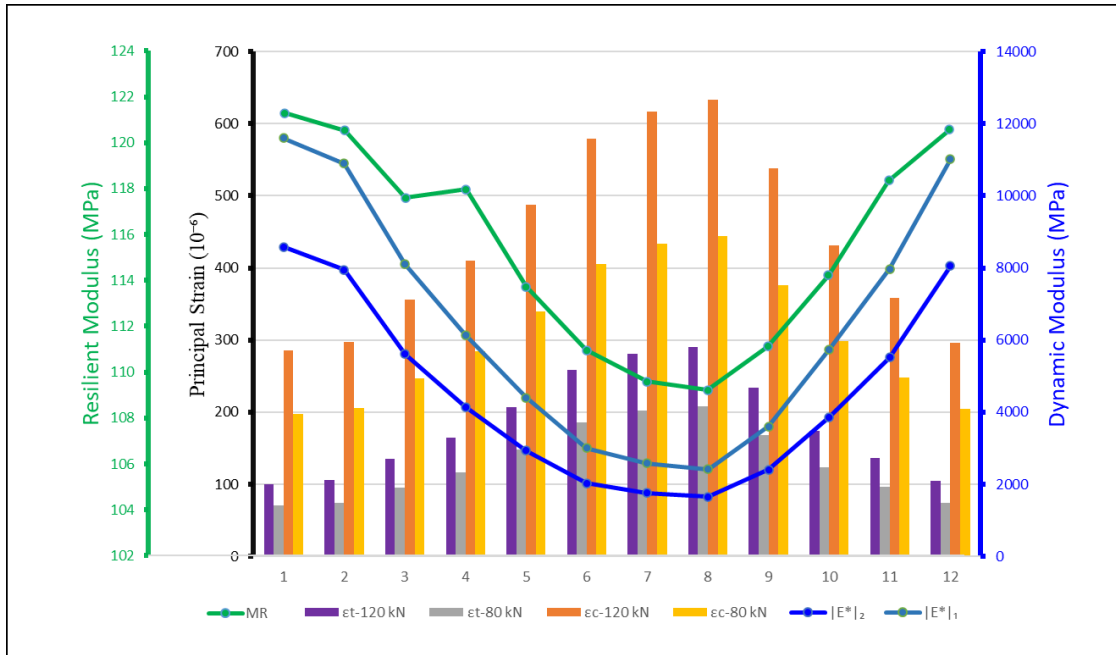


Figure 4.2 Principal strains and material properties

4.1.4 Performances Prediction

The analysis considered the pavement performances as reflected by the functional damages regarding fatigue cracking and rutting. After computing the respective principal critical responses of the pavement structure under 120 kN and 80 kN reference axles for each analysis period, two transfer functions and estimated ESALs uniformly distributed in each analysis period were used to estimate the pavement's fatigue cracking and rutting damages for all 12 of analysis periods. The parameters contained in transfer functions used in the analysis of this section and the corresponding analysis procedures can be found in Chapter 3. To evaluate the total damage resulting from the applied loads of 120 kN and 80 kN over the pavement's 20-year service life, the partial damages derived from every analysis period were summed up. Figure 4.3 shows the variations of fatigue cracking and rutting damages resulting from the structural analysis in regarding reference axles of 120 kN and 80 kN.

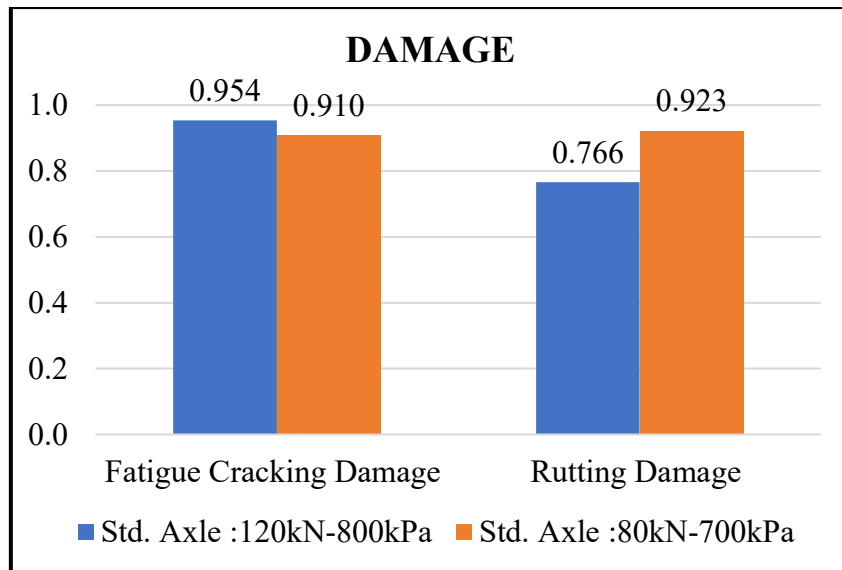


Figure 4.3 Comparison of damages

4.2 Result Analysis and Discussions

In this chapter of the study, the impact of the traffic homogenization model was examined by comparing two reference axles (120 kN and 80 kN reference single-axles). The principal critical strains were calculated using the ALVA computation program. Traffic was homogenized into ESALs using the concept of EALF in relation to the two reference axles. Ultimately, the pavement functional damages at the end of the service life were assessed based on transfer functions and the generated ESALs.

The findings of this study demonstrate that the choice of reference axle significantly impacts traffic modeling and, consequently, pavement structural design, as manifested in the estimated pavement damages at the end of its service life. For the two reference axles and various models and parameters considered in this study, it was determined that, based on identical traffic data, the ESALs modeled with the 120 kN reference axle were about five times lower than those modeled with the 80 kN reference axle. Additionally, the principal tensile strains resulting from the 120 kN reference axle at the bottom of the asphalt base layer were, on average, approximately 1.4 times greater than that resulting from the 80 kN reference axle, and a similar trend and numerical relationship were observed concerning the principal compressive strains on the top of the subgrade layer. When examining the respective estimated damages of fatigue cracking and rutting derived from structural analysis considering two different reference axles, the trends were not identical to each other. Replacing the reference single axle load and its corresponding load configuration of 80 kN with 120 kN in the traffic homogenization model consequently led to a modest increase of approximately 5% in anticipated fatigue damage in pavement, in contrast, the projected rutting damage decreased significantly by 17%.

As a result, it can be inferred that the impacts of higher principal critical strains and a lower number of ESALs resulting from the use of a higher magnitude reference axle in structural analysis and traffic modeling did not offset one another for the analyzed pavement structure. This led to contrasting effects in predicting fatigue

cracking damage compared to rutting damage, overestimating fatigue damage, and underestimating rutting damage. To address this discrepancy, further analysis and adjustments concerning the coefficients incorporated in the EALF calculation formula are necessary. Thus, in following analyses that encompass traffic spectrum estimates linked to typical wind and solar plants, along with pavement structural design for such facilities, the 80 kN reference single-axle will be taken into consideration.

It should be emphasized that the objective of this study was to offer a general evaluation of the impact of the model used for traffic homogenization by comparing two reference axles. For the sake of simplicity, several accessible models and parameter values recommended by their respective authors were used in the current study. However, employing different parameter values, models, or considering different pavement structures in the analysis, the outcomes might be subject to vary.

Chapter 5

Shear Stability Analysis

The transport of overweight/oversize (OW/OS) vehicles serves as a fundamental practice for the development of renewable energy projects, such as wind and solar power plants. The particular conditions imposed by such loads of OW/OS vehicles on pavements are commonly linked to a combination of factors: increased acceleration/deceleration forces on the roadways and augmented turning movements at the bends, abnormally high load magnitude and low traffic speed, and the resting periods may be limited between consecutive axles, which can be attributed to the complex load configurations composed of multiple wheel and axle assemblies designed to optimize load distribution.

Traditionally, pavements are designed with an 80 kN axle as specified in the AASHTO pavement design guide to accommodate vehicle traffic. However, the transport of OW/OS vehicles on these pavements can give rise to conditions that exceed the initial design assumptions, depending upon the pavement geometry and material properties. It is imperative to assess pavement performances under these unconventional loading conditions to prevent structural damage, both rapid and long-term. OW/OS vehicles not only transmit elevated load levels on pavements, but they also induce different stress states compared to the traditional ones due to the arrangement and assembly of multi-axles. Thus, using the models employed in conventional pavement design practice may be challenging given the conditions mentioned above.

The evaluation of potential damages caused by superheavy loads from OW/OS vehicles varies from standard pavement design methods, primarily due to the differences in defining failures. In traditional pavement design, the main focus is on avoiding long-term accumulated strains and fatigue that ultimately cause rutting and cracking, thereby preventing structural failure under typical loading conditions. In contrast, when evaluating pavements under superheavy loads, the emphasis is on the intensity of the wheel loads rather than the frequency of load repetitions. OW/OS vehicles are less likely to repeat loads frequently, making load repetition less of a concern. Therefore, the anticipated failure mode is a rapid load-induced failure caused by shear stress surpassing its shear strength of the material, this is especially relevant

for the subgrade and unbound layers considering their relatively low stiffness and strength characteristics compared to that of asphalt layers.

This work aims to present a design approach used to evaluate the likelihood of localized shear failure (yield) in unbound layers of asphalt pavements subjected to superheavy load conditions. To this end, the Russian structural pavement design guide (ODN 218.046-01) was considered, given its sophistication and wider applications in pavement design compared to alternative shear design methods. By adhering to this design guide, the potential for localized shear failure can be investigated through a rational approach, wherein the maximum active shear stress generated by traffic loading is compared to the shear strength of the soil under critical environmental conditions.

5.1 Analysis Methodology

From a broad perspective, the transportation of superheavy loads can be approached similarly to most geotechnical engineering problems. It involves analyzing the applied load and the resulting response of the structure. In such a case, the load refers to the vehicle carrying the superheavy load, and the behavior of pavement relies on the properties of the analyzed pavement structure. It is typical for most geotechnical engineering problems to necessitate the assessment of the stresses and strains that arise from a particular set of loading conditions and the corresponding response of the structure to these stresses (Fritz J. Jooste et al., 1995). Hence, some brief introductions within the realm of continuum mechanics that are relevant to the concern of shear stability design have been presented as reference.

When considering the application of a uniform strip load (flexible contact area) on hypothetical elasto-plastic material up to the failure of a shallow foundation, the analysis can identify two critical loads that correspond to three phases of deformation beneath the center of the applied strip load in contact with the soil foundation (Whitman and Hoeg, 1966). Based on the existing sector literature, a graphical relationship between foundation settlement and applied load is illustrated in Figure 5.1.

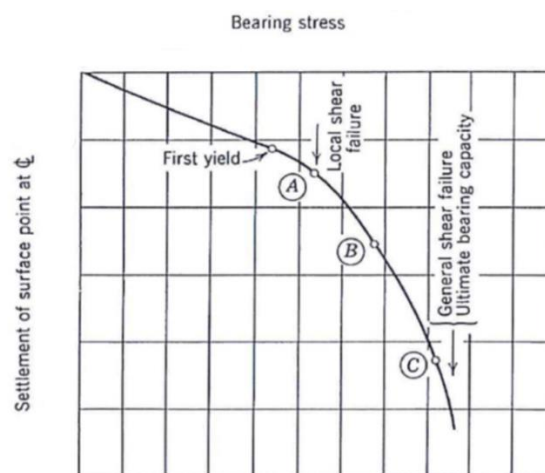


Figure 5.1 Load-Settlement curve (Modified from Whitman and Hoeg, 1966)

The initial phase can be referred to as the compaction phase, which has a linear correlation between the settlement of the foundation and the magnitude of the applied load. During this phase, the soil particles tend to move vertically, and the range of load resulting in this type of deformation is restricted to the first limit load, denoted as P_{1lim} . When the load applied to the foundation equals the first limit load, a plastic zone generates below the central axle of the footing about equal to a half width of the footing at the most critical points in the half-space, as illustrated in Figure 5.2. This indicates that the limit state has been reached, according to the Mohr-Coulomb criterion. However, the limit state has not been reached at all other soil particles under this load. During the compaction phase, the soil in the foundation exhibits elastic-plastic behavior, and the settlement includes both reversible and irreversible components. Since settlement is linearly connected with the magnitude of applied load, solutions of elasticity theory are used to determine it.

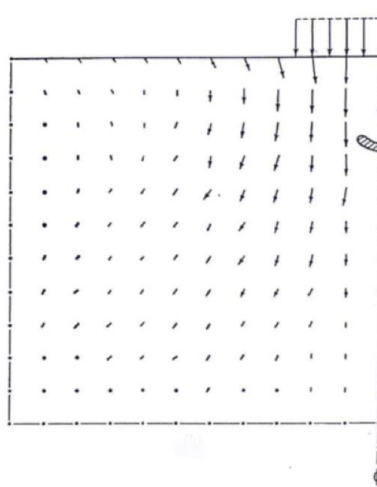


Figure 5.2 First yielded zone (Whitman and Hoeg, 1966)

The second phase of deformation is known as the local shear failure phase, where the linear relationship between the load and settlement no longer maintained and a nonlinear behavior occurs, leading up to the general shear failure of the soil foundation system. During this nonlinear phase, the rate of settlement increment significantly increases concerning a given rate of applied load, resulting in higher settlement than during the compaction phase for the same load increment. This is equivalent to saying that the compressibility of the soil increases as it exhibits plastic behavior. The onset of this nonlinear behavior occurs when the first plastic zone generates in the soil mass, characterized by the maximum stress that the material is able to sustain. Moreover, as the load on the foundation surpasses the first critical load, the plastic zone propagates further into the surrounding elastic zone, increasing the size of the unstable areas (Figure 5.3). When the load reaches the second limit load, denoted as P_{2lim} , the plasticized zone reaches the ground surface (Figure 5.4), and the sliding surface appears on the foundation surface. At this point, the failure mechanism is formed, where the soil behavior transitions from the elastic phase to shear failure due to the propagation of the plastic zone upon increasing vertical load.

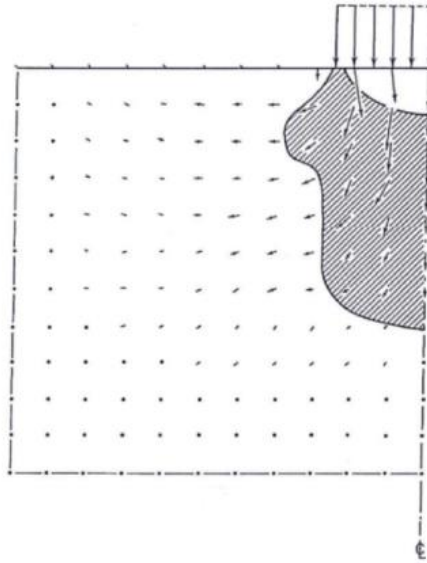


Figure 5.3 Propagation of the plastic zone (Whitman and Hoeg, 1966)

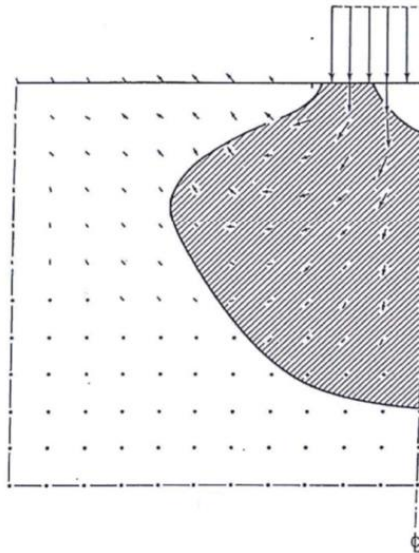


Figure 5.4 Plastic zone reaching the foundation surface (Whitman and Hoeg, 1966)

The third phase of deformation is known as the general shear failure phase, is characterized by soil displacement surpassing the load transfer zone due to the presence of a sliding surface. Within this phase, the ultimate bearing capacity of the foundation is exhausted, consequently leading to a disruption in the load distribution mechanism.

In pavement design practices, it is important to maintain the elastic behavior of unbound layers, allowing for reversible displacements under traffic loads. Additionally, emphasizing a deflection-based service limit is essential for ensuring travel comfort and safety. Therefore, a design approach was studied to evaluate the probability of localized shear failure (yield) in unbound layers of asphalt pavements subjected to superheavy load conditions using the Mohr-Coulomb criterion, based on the Russian structural pavement design guide (ODN 218.046-01).

5.1.1 Evaluation of Limiting Shear Stress

The main form of discontinuity in soils and similar mediums under the action of external loads is shear failure. The strength limit state is reached at any point in a mass when the shear stress on the sliding surfaces reaches the shear resistance value of the soil or material. Various mathematical techniques are employed to address the issue of shear resistance of soils during the initial or subsequent deformation phases. To establish equations using the linear deformed medium approach, the calculation of the total shear stress at the most critical point is determined by applying the Mohr-Coulomb criterion. The evaluation of the total shear stresses involves assuming the presence of an unstable plasticized zone that reaches a critical value when the foundation load is equal to the first critical load.

According to the Russian structural pavement design guide (ODN 218.046-01), the ultimate shear equilibrium condition is adopted as the strength condition for soils and similar media. In the case of soils, which commonly experience compressive conditions, Mohr's theory of strength is particularly applicable. The strength criterion based on Mohr's theory can be expressed as follows:

$$|\tau_n| = f(\sigma_n) \quad 5.1$$

Where:

- τ_n and σ_n are the shear and normal stresses on the slip area.

Although there may be varying views on the nature of the relationship, it is widely accepted for practical calculations that the shear resistance of soils and similar materials increases proportionally with an increase in normal stress, in accordance with Coulomb's friction law:

$$|\tau_n| = c + \sigma_n \cdot \tan\varphi \quad 5.2$$

Where:

- c is cohesion of soils, expressed in MPa;
- φ is angle of soil particle internal friction, in $^\circ$.

The Mohr's circle of stress is a geometric representation of the state of stress, which is commonly used in engineering and mechanics. It represents a linear mapping that associates the state of stress acting on the plane oriented by the outward unit normal to the direction of state of stress. By plotting the magnitudes of the stresses at different angles (referred to as φ in Figure 5.5) to the main planes wherein the shear component vanishes and only the normal component (σ_1 and σ_2 in Figure 5.5) remains, the Mohr's circle of stress establishes the relationship between the stress magnitudes and the direction of stress acting on the main plane.

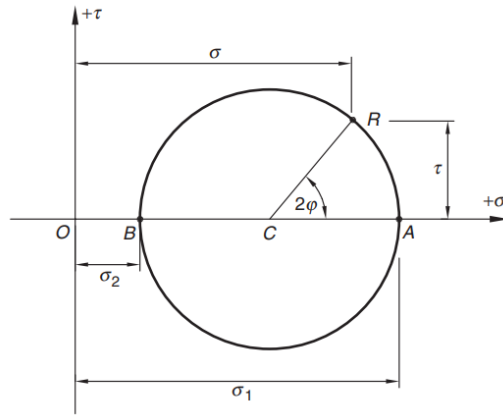


Figure 5.5 Mohr's circle (Renato Lancellotta, 2008)

In a state of plane stress, the maximum and minimum normal stresses acting on a particular plane of a stress element are known as the major and minor principal stresses, represented by σ_1 and σ_3 as shown in Figure 5.6, respectively. The shear stress τ_α acting along a plane inclined at an angle α to the principal plane is a projection onto the vertical axis of the circle radius. The radius is drawn at an angle of 2α to the abscissa axis. On the other hand, the normal stress acting on the same plane is equal to the segment σ_α .

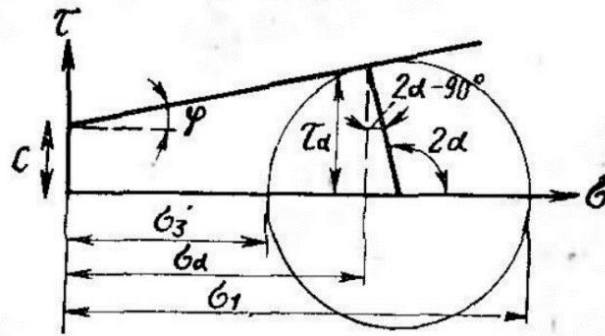


Figure 5.6 Shear and normal stresses in a plane stress state (ODN 218.046-01, 2001)

By representing the principal stresses, it is possible to express the shear and normal stresses as following:

$$\tau_\alpha = \frac{1}{2} \cdot (\sigma_1 - \sigma_3) \cdot \cos(2\alpha - 90^\circ) = \frac{1}{2} \cdot (\sigma_1 - \sigma_3) \cdot \sin(2\alpha) \quad 5.3$$

$$\begin{aligned} \sigma_\alpha &= \sigma_3 + \left[\frac{1}{2}(\sigma_1 - \sigma_3) - \frac{1}{2}(\sigma_1 - \sigma_3) \cdot \sin(2\alpha - 90^\circ) \right] \\ &= \frac{1}{2} [(\sigma_1 + \sigma_3) + (\sigma_1 - \sigma_3) \cdot \cos(2\alpha)] \end{aligned} \quad 5.4$$

When the stress state at a specific point is limiting, then the Mohr's circle intersects with the limit line (see Fig. 5.6), which is represented by Coulomb's friction criterion, and its position is determined by Equation 5.2. Moreover, the correlation between the angle of the inclination of the sliding plane and the principal plane can be stated as:

$$\alpha = 45^\circ + \frac{\varphi}{2} \quad 5.5$$

By replacing the values of σ_α and τ_α obtained from Equation 5.2 with Equation 5.3 and 5.4 and substituting the value of 2α with $90^\circ + \varphi$ as given by Equation 5.5, the limit equilibrium condition at a point in a plane stress state can be determined in Equation 5.6.

$$\frac{1}{2 \cdot \cos \varphi} [(\sigma_1 - \sigma_3) - (\sigma_1 + \sigma_3) \sin \varphi] = c \quad 5.6$$

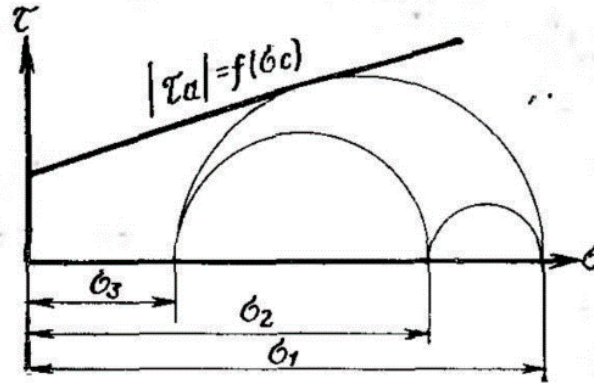


Figure 5.7 Mohr diagram under volumetric stress state (ODN 218.046-01, 2001)

According to the definition provided by the Russian structural pavement design guide (ODN 218.046-01), the volumetric stress conditions, which are typical for road pavements which under the action of a load from a vehicle wheel, a disruption in the equilibrium is only possible when a complete limit equilibrium is achieved at a specific point. In such a situation, the stress state can be depicted by three stress circles, as shown in Figure 5.7. To reach the full limit equilibrium, either the second or third stress circle must make contact with the limit line. Therefore, to properly reflect this condition, the expression given in Equation 5.6 must be accompanied by the following conditions:

$$\frac{1}{2 \cdot \cos \varphi} [(\sigma_1 - \sigma_2) - (\sigma_1 + \sigma_2) \sin \varphi] = c \quad 5.7$$

or condition:

$$\frac{1}{2 \cdot \cos \varphi} [(\sigma_2 - \sigma_3) - (\sigma_2 + \sigma_3) \sin \varphi] = c \quad 5.8$$

It is important to note that when both condition 5.6 and 5.7 are met, they result in an equality as following:

$$\sigma_2 = \sigma_3 \quad 5.9$$

and conditions 5.6 and 5.8 to equality:

$$\sigma_2 = \sigma_1 \quad 5.10$$

By combining Equation 5.6 and 5.2, the limit equilibrium condition can be expressed as following:

$$\frac{1}{2 \cdot \cos \varphi} [(\sigma_1 - \sigma_3) - (\sigma_1 + \sigma_3) \sin \varphi] = \max[\tau_n - \sigma_n \cdot \tan \varphi] \quad 5.11$$

Where:

- τ_n and σ_n are the shear and normal components of the stress at the limit state, in MPa.

In other words, the left side of the Equation 5.11 is the difference between the shear stress and the product of the normal stress on the coefficient of internal friction over such an area at each point at which this difference reaches a maximum value. Since this value is the largest free (minus the confining forces due to internal friction) shear stress, it is considered as the maximum active shear stress.

$$\tau_{max} = \frac{1}{2 \cdot \cos \varphi} [(\sigma_1 - \sigma_3) - (\sigma_1 + \sigma_3) \sin \varphi] \quad 5.12$$

Where:

- τ_{max} is the maximum active shear stress at the analysis point from the traffic load, in MPa;
- σ_1 is the major principal stress, in MPa;
- σ_3 is the minor principal stress, in MPa;
- φ is the angle of internal friction, in $^\circ$.

Equation 5.11 presents the limit stress state condition using axes that are oriented along the principal planes. However, for the sake of convenience in the stress components calculation, the principal stresses are transformed into the Cartesian coordinate system by means of the steps described below.

Considering a unit element ABCD located on the X-Z plane, this unit experiences normal stresses σ_x and σ_z as well as the accompanying shear stresses τ_{xz} and τ_{zx} on their corresponding planes (Figure 5.8). Additionally, there exists an oblique plane of AE that is inclined at an angle of α with respect to the unit element.

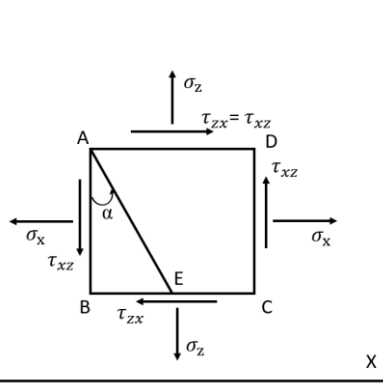


Figure 5.8 Stress components and related planes

To determine the principal stresses on the AE plane, the ABE segment was analyzed. Subsequently, all stresses acting upon this segment were transformed into

forces by multiplying their corresponding areas and assuming a unit thickness of the segment.

$$F_x = \sigma_x \cdot AB, F_z = \sigma_z \cdot BE, F_\alpha = \sigma_\alpha \cdot AE \quad 5.13$$

$$F_{\tau_{xz}} = \tau_{xz} \cdot AB, F_{\tau_{zx}} = \tau_{zx} \cdot BE, F_{\tau_\alpha} = \tau_\alpha \cdot AE \quad 5.14$$

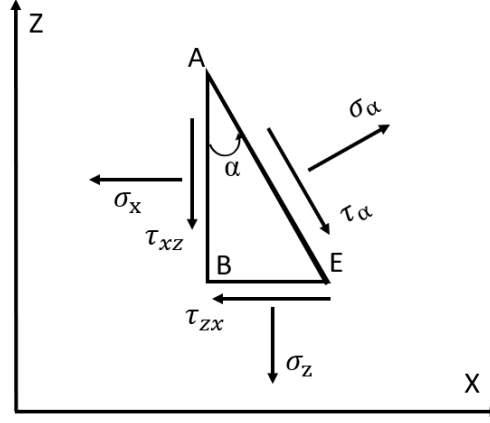


Figure 5.9 Stress components on segment ABE

Next, to resolve all the forces into directions parallel and perpendicular to AE and establish equilibrium in both of these directions.

Perpendicular to AE:

$$\sigma_\alpha \cdot AE = \sigma_x \cdot AB \cdot \cos \alpha + \tau_{xz} \cdot AB \cdot \sin \alpha + \tau_{zx} \cdot BE \cdot \cos \alpha + \sigma_z \cdot BE \cdot \sin \alpha \quad 5.15$$

Then, by solving the obtained equilibrium equation:

$$\begin{aligned} \sigma_\alpha &= \sigma_x \cdot \frac{AB}{AE} \cdot \cos \alpha + \tau_{xz} \cdot \frac{AB}{AE} \cdot \sin \alpha + \tau_{zx} \cdot \frac{BE}{AE} \cdot \cos \alpha + \sigma_z \cdot \frac{BE}{AE} \cdot \sin \alpha \\ &= \sigma_x \cdot \cos \alpha \cdot \cos \alpha + \tau_{xz} \cdot \cos \alpha \cdot \sin \alpha + \tau_{zx} \cdot \sin \alpha \cdot \cos \alpha + \sigma_z \cdot \sin \alpha \cdot \sin \alpha \\ &= \sigma_x \cdot \cos^2 \alpha + 2 \cdot \tau_{xz} \cdot \sin \alpha \cdot \cos \alpha + \sigma_z \cdot \sin^2 \alpha \\ &= \sigma_x \cdot \left(\frac{1 + \cos 2\alpha}{2} \right) + \tau_{xz} \cdot \sin 2\alpha + \sigma_z \cdot \left(\frac{1 - \cos 2\alpha}{2} \right) \end{aligned}$$

Finally, the stress normal to AE can be derived:

$$\sigma_\alpha = \frac{\sigma_x + \sigma_z}{2} + \frac{\sigma_x - \sigma_z}{2} \cdot \cos 2\alpha + \tau_{xz} \cdot \sin 2\alpha \quad 5.16$$

By following the same approach, the equilibrium parallel to AE can be written and solved to determine the shear stress tangent to AE, as presented below:

$$\tau_\alpha = -\frac{\sigma_x - \sigma_z}{2} \cdot \sin 2\alpha + \tau_{xz} \cdot \cos 2\alpha \quad 5.17$$

As the shear stress on the principal plane is equal to zero, the subsequent result can be derived:

$$\frac{\sigma_x - \sigma_z}{2} \cdot \sin 2\alpha = \tau_{xz} \cdot \cos 2\alpha \quad 5.18$$

$$\tan 2\alpha = \frac{2 \cdot \tau_{xz}}{\sigma_x - \sigma_z} \quad 5.19$$

As there are two principal planes present in the unit element, positioned perpendicular to one another, the locations of these principal planes can be determined as follows:

$$\alpha_1 = \alpha, \alpha_2 = \alpha + 90^\circ$$

Based on Equation 5.19, the subsequent derivations can be obtained:

$$\sin 2\alpha = \pm \frac{2 \cdot \tau_{xz}}{\sqrt{(\sigma_x - \sigma_z)^2 + 4 \cdot \tau_{xz}^2}} \quad 5.20$$

$$\cos 2\alpha = \pm \frac{\sigma_x - \sigma_z}{\sqrt{(\sigma_x - \sigma_z)^2 + 4 \cdot \tau_{xz}^2}} \quad 5.21$$

By substituting Equations 5.20 and 5.21 into Equation 5.16, the principal stresses could be written as:

$$\sigma_\alpha = \frac{\sigma_x + \sigma_z}{2} \pm \sqrt{\left(\frac{\sigma_z - \sigma_x}{2}\right)^2 + \tau_{xz}^2} \quad 5.22$$

Consequently, the major principal stress can be determined as:

$$\sigma_1 = \frac{\sigma_x + \sigma_z}{2} + \sqrt{\left(\frac{\sigma_z - \sigma_x}{2}\right)^2 + \tau_{xz}^2} \quad 5.23$$

The minor principal stress can be obtained as:

$$\sigma_3 = \frac{\sigma_x + \sigma_z}{2} - \sqrt{\left(\frac{\sigma_z - \sigma_x}{2}\right)^2 + \tau_{xz}^2} \quad 5.24$$

The two principal planes within the unit element can be depicted as shown in Figure 5.10.

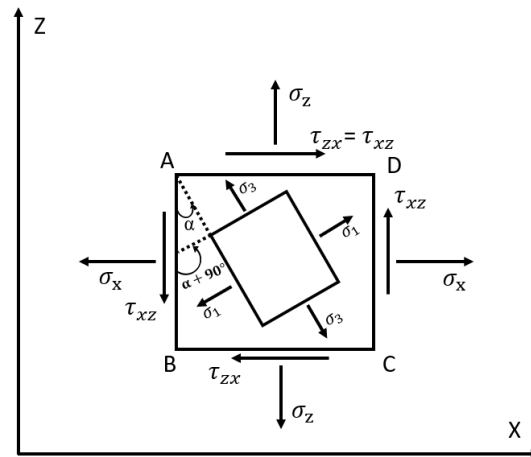


Figure 5.10 Two principal planes

5.1.2 Structural Analysis

The prediction of the likelihood of load induced shear failure under a superheavy load can be solved by determining the maximum allowable axle load that a designed pavement structure can be sustained. This necessitates the determination of the stresses generated by the applied load. To do this, the multi-layer elastic system was assumed as the reference structural model in defining the stresses in the defined pavement structure with the materials mechanical properties assigned to each layer evaluated in the most critical environment condition. It was assumed that each material is considered as linearly elastic, homogeneous, isotropic. Additionally, each layer was assumed to be infinitely extended laterally and of constant thickness, except for the subgrade, which was modeled as a homogeneous infinite half-space.

The load applied to the multi-layer system was considered to be the heaviest axle load of a single axle or within an axle group (e.g., tandem, tridem, and multi-axle group). It was anticipated that superheavy load hauling units would be employed in the development of wind and solar farms. The load configurations of these hauling vehicles are typically complex, consisting of multiple axles within an axle group (e.g., quad-axle and five-axle group). According to the previous studies of the effects of multi-axle assembly on the shear stability prediction reviewed in Section 2.5, it was found that the stress states and yield function values predicted by simplified load configurations (i.e., single axle load and half-axle load) were quite similar to those of the more complex multi-axle assembly and the critical yield functions were typically predicted at the same locations in all load configurations. Moreover, it is believed that simplifying a multiple axle load configuration to a single axle, or a half-axle load resulting a more conservative prediction of the shear failure and can sufficiently simulate the pavement stress conditions under a multiple axle load. Therefore, to simplify the current study, in the event that a multi-axle group represents the heaviest load, only one of those composing axles will be applied to evaluate the stresses in the pavement layers of the defined multi-layer structural model. Moreover, for structural analysis purposes, only the semi-axle was considered.

The stress responses of multi-layer system structure under loading were computed at four critical depths: on the top of both the unbound base layer and subgrade layer,

and at the bottom and in the middle of unbound base layer. Regarding asphalt layers, it is believed that they are less prone to shear failure than unbound layers attributed to their high stiffness and strength of mechanical characteristics. Therefore, the assessment of load-induced shear failure in asphalt layers was not considered in this study.

Additionally, such responses were evaluated at several distinct transversal positions depending on the wheel load configuration of the axle under analysis. In general, the transversal evaluation positions can be grouped as follows:

- Group 1- under the vertical axis of each circular load;
- Group 2- under the center-point between each two circular loads vertical axis;
- Group 3- under the two edges of each circular load; and
- Group 4- under the middle of axle load.

In this study, the numerical solutions of the stress responses under loading at each of previously defined response points were obtained for the multi-layer elastic system under the most critical environmental condition. This was done using an open-source MATLAB[®] based code titled: Adaptive Layered Viscoelastic Analysis (ALVA), which is described in Section 3.3.6. In order to compare the shear stress invoked by the applied load to the material strength, once the stress responses of pavement structure in each of evaluation points were computed, the limiting shear stress can be subsequently determined by following the limit equilibrium criterion outlined in Section 5.1.1.

It should be noted that the stress states calculated at the predefined estimation points may not be subjected to the volumetric stress conditions for which the shear stability design method indicated in the Russian pavement design method is applicable. As a result, predicting shear failure under such conditions may not lead to a full limit equilibrium failure and may not cause a disruption in the equilibrium. Thus, the predicted results may only represent partial shear failure and result in a conservative analysis. However, the outputs obtained from the estimation points can be considered as a preliminary analysis to identify the most susceptible points in the pavement under loading. As per the Russian pavement design method, volumetric stress conditions can be observed in road pavements when subjected to a load from a vehicle wheel along the center vertical line of the loading area. Accordingly, the current study adopts the Equivalent Single-Wheel Load (ESWL) to predict shear failures that disrupt full limit equilibrium in pavements, replacing the multiple wheel loads acting on the pavements.

According to Huang's book (2004), the ESWL can be determined through theoretically calculated or experimentally measured equal vertical stress, equal tensile strain, or equal vertical deflection, assuming that a single wheel and one of the dual wheels have the same contact pressure or equal contact radii. Given the closer relateness between vertical deflection and shear stability compared to other criteria, the criterion of equal vertical deflection was chosen to determine the ESWL in the present study. Furthermore, the assumption was made that the single wheel has a different contact radius but the same contact pressure as each of the dual wheels in estimating the ESWL. This assumption is more reasonable and has been frequently

made in the determinations of ESWL, as opposed to assuming equal contact radius (Huang, 2004). In this study, the ESWLs were determined using a "trial and error" approach, with equal vertical deflection calculations conducted at the most vulnerable estimation point to shear failure in the defined pavement structure by using MATLAB[®] based code ALVA.

5.1.3 Shear Stability Verification

The design of pavements aims to prevent the accumulation of unacceptable residual deformations over their entire service life caused by traffic loads on the underlying soil and unbound layers. By referring to shear failure, to ensure that no inadmissible shear strains occur in the pavement structure, the damage ratio between the computed maximum active shear stress and the allowable shear strength of the analyzed layer, is verified as indicated in Equation 5.25:

$$D_{\tau} = \frac{\tau_{max}}{\tau_{all}} \quad 5.25$$

Where:

- D_{τ} is the load-induced shear damage ratio;
- τ_{max} is the maximum shear stress generated by the heaviest axle load, in MPa;
- τ_{all} is the allowable shear strength of the material composing the analyzed layer, in MPa.

According to the definition provided in the Russian structural pavement design guide (ODN 218.046-01), the allowable shear strength of the material composing the analyzed layer can be determined by the following relationship:

$$\tau_{all} = \frac{1}{F_{rel}} \cdot (c_c \cdot k + \sigma \cdot \tan\varphi_{st}) \quad 5.26$$

Where:

- τ_{all} is the allowable shear strength of the material composing the analyzed layer, in MPa;
- F_{rel} is a reliability parameter that depends on the importance of the pavement;
- c_c is the cohesion of the soils in the analyzed layer under critical environmental condition, in MPa;
- k is a parameter that depends on the boundary properties at the layer interface. When constructing with reinforced materials, as well as when inserting a separating geotextile layer at the boundary base-subgrade, the values can be taken as:
 - = 4,5, when used in a sandy layer of coarse sand;
 - = 4, when used in a sand layer of medium-size sand;
 - = 3, when used in a sandy layer of fine sand;
 - = 1, in all other cases.

- σ is the normal stress generated from the self-weight of the layers placing above the analyzed one, in MPa;
- φ_{st} is the design value of the angle of internal friction of the material of the analyzed layer under the static action of the load, expressed in $^{\circ}$.

The normal stress generated from the self-weight of the layers placing above the analyzed one can be calculated as:

$$\sigma = \gamma_{avg} \cdot H \quad 5.27$$

Where:

- γ_{avg} is the weighted average density of the structural layers located above the analyzed one, in kN/m^3 , $\gamma_{avg} = \frac{\sum \gamma_i \cdot H_i}{\sum H_i}$;
- H is the depth of the layer's surface being analyzed, measured from the top of the pavement structure, in m.

In according to the pavements in the development of renewable green plans, the structural verification of localized shear failure (yield) is satisfied when damage values computed for shear is lower than the unity, with the consideration of the maximum shear stresses generated in the subgrade and in all unbound layers under the heaviest axle load.

5.2 Material Properties Considerations

The problem of predicting the probability of shear failure when subjected to a superheavy load can be addressed by estimating the maximum active shear stress that a particular pavement structure can withstand. It should be highlighted that, in numerous instances, the reason for load-induced local shear failure (i.e., rapid plastic deformations) cannot be attributed solely to an excessive load but rather to the strength characteristics of the material. This observation is particularly significant in examining how pavements react to superheavy loads. It is possible that a pavement structure could appear sufficient for supporting a superheavy load, provided that the materials employed in the analysis are well-designed and stable materials. Nonetheless, if any of the pavement layer materials turn out to be inadequately designed or prone to rutting, it could result in rapid shear deformations. Thus, the material parameters serve as important factors in determining the probability of shear failure under atypical loading circumstances.

The shear strength of a pavement material, such as soil or crushed stone, comprises two primary elements: the cohesive component and the frictional component. The cohesive strength of granular materials and clays is linked to the moisture content in the material. On the other hand, the friction angle is determined by various factors such as surface roughness, angularity, and the particle size distribution. These two elements contribute differently to the material's shear strength, depending on the type of material. For instance, a wet clay material typically exhibits little to no frictional resistance since its particles tend to slide against each other. In this scenario, the majority of the material's shear strength is attributed to the cohesion present between individual particles. In contrast, if a coarse granular material is under

compression, the majority of its shear strength comes from the frictional component, the source of this friction is the resistance that arises between particles when they slide or roll against each other while under loading (Fritz J. Jooste et al., 1995).

In this section, common material properties derived from previous engineering experience and studies conducted on various types of base and subgrade materials using a series of Texas Triaxial Class tests are presented (Fritz J. Jooste et al., 1995). Tables 5.1 and 5.2 present standard values for cohesion and angle of friction associated with typical types of subgrade and base/sub-base course materials.

Table 5.1 Typical Cohesion and Angle of Friction Values for Subgrade Materials

Material Type	Cohesion at moisture content (kPa)			Friction Angle at moisture content (°)		
	Below Opt.	At Opt.	Above Opt.	Below Opt.	At Opt.	Above Opt.
Sand	7.6	10.3	4.8	42.0	40.0	41.0
Sandy Gravel	24.8	15.8	21.4	29.0	48.0	39.0
Lean Clay	108.9	113.0	51.7	44.0	38.0	38.0
Fat Clay	137.1	119.9	43.4	18.0	0.0	0.0
Silt	32.4	33.1	28.9	43.0	42.0	43.0
Averages for Sandy Materials	16.5	13.1	13.1	36.0	44.0	40.0
Standard Deviation for Sandy Materials	12.2	3.9	11.7	9.9	5.7	1.4
Averages for Clayey Materials	92.8	88.7	41.3	35.0	27.0	27.0
Standard Deviation for Clayey Materials	54.2	48.3	11.5	14.7	23.2	23.5

Table 5.2 Typical Cohesion and Angle of Friction Values for Base/Sub-base Materials

Material Type	Cohesion at moisture content (kPa)			Friction Angle at moisture content (°)		
	Below Opt.	At Opt.	Above Opt.	Below Opt.	At Opt.	Above Opt.
Caliche	90.8	77.3	46.9	43.0	48.0	49.0
Iron Ore Gravel	68.3	73.3	59.3	47.0	48.0	48.0
Shell Base	74.4	68.2	59.9	51.0	51.0	53.0
Limestone	29.5	48.9	54.4	55.0	53.0	52.0
Average	65.8	66.9	55.1	49.0	50.0	50.5
Std. Dev.	26.0	12.6	6.0	5.2	2.4	2.4

Additionally, some typical material densities for asphalt layer, base/sub-base layer and subgrade layer are provided in Table 5.3 in accordance with ODN 218.046-01.

Table 5.3 Physical Characteristics of Structural Layer Materials

Material Type	Density (kN/m ³)
Hot Mixed Asphalt	2.40E-05
Crushed Limestone	1.60E-05
Gravel	1.80E-05
Gravel-Sand Mixture	2.00E-05
Crushed Stone from Granite	1.80E-05

Chapter 6

Reference Traffic Spectra for Wind and Solar Farms

In this chapter, an assessment is presented regarding the traffic that could be generated as a result of the development of wind and solar farms.

6.1 Wind Farm

Wind farm developments generally consist of three distinct phases, which are outlined below:

- Phase 1: Construction of the wind farm
- Phase 2: Operation of the wind farm
- Phase 3: Decommissioning of the wind farm

The subsequent sections present an overview of the activities that take place in each of the phases. These activities were then considered to estimate the reference traffic spectrum of wind farm development in each phase.

Key Assumptions

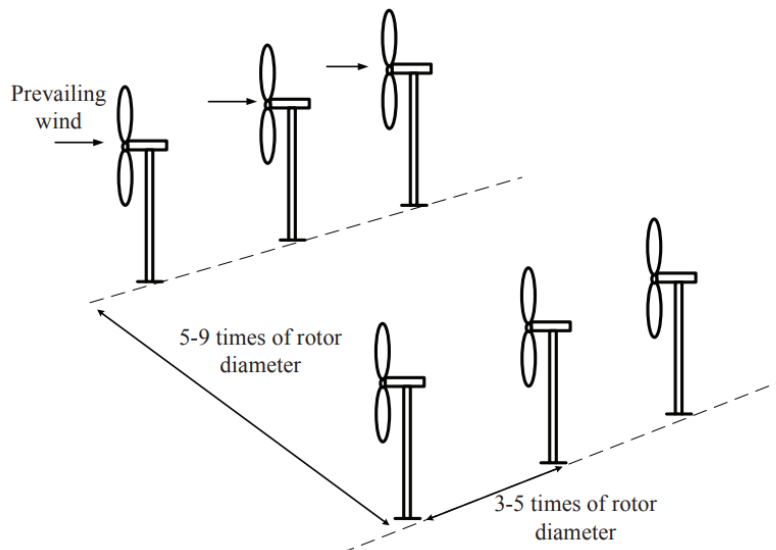
The estimations of trip generation and traffic distribution in this assessment relied on several assumptions that have been considered regarding the scope of construction activities, construction program, construction methodology, and sources of materials. These assumptions comprise, but are not limited to, the following:

Proposed development:

The proposed wind farm was planned to have a generation capacity of 186 MW (million watts) of electrical power from the combined output of 30 Vestas V162 wind turbines, each with a nominal generation capacity of 6.2 MW. The proposed lifetime of the wind farm was assumed to be 25 years.

Wind turbines spacing:

Since wind turbines convert the energy of the wind into electricity, the wind that leaves the turbine must possess less energy content than the wind that approaches the turbine. As a result, a wind turbine will inevitably cast a wind shade in the direction of the wind downstream. The wind behind the turbine will create a wake that is relatively turbulent and slowed down, as opposed to the wind ahead of the turbine. In order to limit the turbulence around turbines downstream, it is optimal to position turbines as far apart as possible in the direction of the prevailing wind. However, the cost of connecting wind turbines to the power grid and the available land usage necessitate spacing them closer together. As a general guideline, wind turbines in wind farms are typically positioned between 5 and 9 rotor diameters apart in the direction of the prevailing wind and between 3 and 5 diameters apart in the direction perpendicular to the prevailing wind a grid pattern (see Fig. 6.1) (DWIA, 2023). Hence, in this study, the wind turbines are assumed to be arranged at a spacing of 7 rotor diameters in the direction of the prevailing wind and 4 rotor diameters perpendicular to the wind direction.



Source: N. Gupta (2016)

Figure 6.1 Wind turbines spacing

Internal access tracks:

The internal access tracks will serve the purpose of providing access to each turbine location for construction vehicles, work forces and hauling vehicles during the construction and decommissioning phases. Additionally, the access tracks will also enable service access during the operational phase.

Assuming the wind turbines were spaced in a grid pattern as specified previously, the maximum total distance for internal access roads was estimated to be 44.5 km (consisting of 5 rows in the direction of the prevailing wind, with 6 turbines in each row, and 6 columns perpendicular to the wind direction, with 5 turbines in each column), while the minimum distance was 19.0 km (only one row of turbines in the prevailing wind direction). Considering the geographical and topographical features of the site in question, approximately 30 km of roads were assumed for internal access

tracks and were assumed to be 6 m wide and have 400 mm pavement depth of gravel and crushed stone materials.

6.1.1 Construction Phase

This section describes the works proposed for the construction, and the corresponding traffic associated with each task was also discussed. The various construction work phases will occur concurrently, resulting in an overlapping schedule. It was assumed that the construction phase of the project would last around 18 months.

Site establishment

Internal track and hardstands:

The 30 km of on-site access tracks (6 m wide x 400 mm deep) required for construction and ongoing operation and maintenance of the wind farm was assumed as mentioned above. In addition, it is necessary for each turbine to have a hardstand area that serves multiple purposes, including parking for construction vehicles, laydown of turbine components, assembly areas for the large cranes used for erecting turbine components and other equipment, as well as turning areas for trucks used to transport equipment and materials to each turbine. It was assumed that a single hardstand area measuring 70 meters by 50 meters and with a depth of 500 millimeters will be required to support the construction activities at each individual wind turbine location.



Source: NWS (2021)

Figure 6.2 Internal track and hardstand

It can be further assumed that the construction materials for both the internal roads and hardstands will be made of gravel and crushed stones, with a density of 2 tonnes per cubic meter and a loading bulk factor of 20 %. Based on these assumptions, the total volume of construction materials required for the construction of 30 kilometers of internal access tracks and 30 hardstands can be estimated as 172800 tonnes and 126000 tonnes, respectively.

Batching plant:

Given that wind farms are typically constructed in rural areas, it was expected that an on-site batching plant will be realized to produce the concrete needed for turbine foundation construction and other related activities. The assumed batching plant was estimated to occupy an area of approximately 100 meters by 100 meters and with a depth of 400 millimeters, and likely to consist of a trailer-mounted concrete mixer, cement bins, truck loading hardstand, aggregate stockpiles, as well as a storage container for various equipment and tools. Applying the same assumptions regarding the construction materials used for internal tracks and hardstand, it was estimated that approximately 9600 tonnes of gravel and crushed stones will be required for the batching plant ground construction.

Delivery of equipment:

Establishing the site for a wind farm construction project encompasses a variety of civil works activities and infrastructure installation tasks that necessitate the use of diverse equipment. It is listed below the assumed typical equipment to be delivered to the site during site establishment phase.

5 x Excavator; 5 x Bulldozer; 5 x Loader; 5 x Grader; 2 x Roller; 2 x Trencher; 2 x 60-t capacity crane;

Water delivery:

During construction, water will be needed primarily for dust control and site restoration, and to a lesser extent for domestic use by site staff. It was expected that approximately 20 kiloliters (kL) of water would be required each day for dust suppression, and 5 kL of water would be used each working day as potable water.

Work force

The workforce needed for the construction activities varies depending on the specific tasks being performed. Consequently, there will be fluctuations in the amount of traffic generated on a monthly basis to reflect the work being done. To simplify the estimation of traffic associated with the workforce, it was assumed that there would be an average daily workforce of 80 people throughout the 18-month construction period, with a 6-day work week and an average of 2 people per car/light vehicle.

Footing

Each of the wind turbines was mounted on a reinforced concrete footing. And its design is dependent upon the specific wind turbine model and geotechnical features of each site. It was estimated that the dimension for each circular footing would be approximately 8 meters in radius and up to three meters deep, requiring about 603 m³ of concrete (typical ratio 1 cement : 1.5 sand : 3 aggregates : 0.6 water), say 610 m³. A total of 80 tonnes of steel per foundation was assumed. Additionally, it was assumed that the typical densities of the composite materials used in producing concrete are 1.5 tonnes/m³ for Portland cement, 2 tonnes/m³ for sand, 1.5 tonnes/m³ for aggregates, and 1.0 tonne/m³ for water. The excavation for the footings was planned to be about 9 meters in radius to allow for sufficient working space, facilitating easy access during the installation of the foundation and construction of

the structure. While the bulk density of 1.5 tonnes per cubic meter and 20% of bulking factor were expected for the excavated debris.

Wind turbine delivery and assembly

Wind turbine components:

Each wind turbine would be consisting of a nacelle mounted onto a tubular tower made up of 5 tower sections, a drive train, a turbine hub, and a three-blade rotor (Fig. 6.3)



Source: Vestas (2020)

Figure 6.3 Wind turbine composition

The dimensions and loads of the major components that make up a single wind turbine are outlined in Table 6.1.

Table 6.1 Wind Turbine Components (Vestas V162-6.2 MW)

Component	Length (m)	Width (m)	Height (m)	Weight (kN)
Nacelle	18.1	4.2	4.4	860
Hub	5.0	4.4	4.0	621
Blade	80.0	4.8	3.5	280
Base section 1	11.7	5.0	4.7	860
Base section 2	18.8	4.7	4.5	850
Middle section	28.0	4.5	4.5	900
Top section 1	28.9	4.5	4.5	760
Top section 2	29.0	4.5	4.0	640
Drive train	7.5	2.7	3.0	953

Source: Tilt Renewables Australia Pty Ltd (2022)

The movements of the wind turbine components require OW/OS vehicles. Table 6.2 specifies the specific hauling units required for transporting each component.

Table 6.2 Employed specific hauling vehicles

Component	Hauling unit
Nacelle	Tractor with 4x8-4x8 extending platform trailer
Hub/Rotor	Tractor with 10x8 platform trailer
Blade	Tractor with 2x8 dolly, 4x4 Steerable extendable
Tower-section 1	Tractor with 4x8-4x8 extending platform trailer
Tower-section 2	Tractor with 4x8-4x8 extending platform trailer
Tower-section 3	Tractor with 4x8-5x8 low extending platform trailer
Tower-section 4	Tractor with 4x8-4x8 extending platform trailer
Tower-section 5	Tractor with 4x8-4x8 extending platform trailer
Drive train	Tractor with 10x8 platform trailer

Source: Tilt Renewables Australia Pty Ltd, (2022)

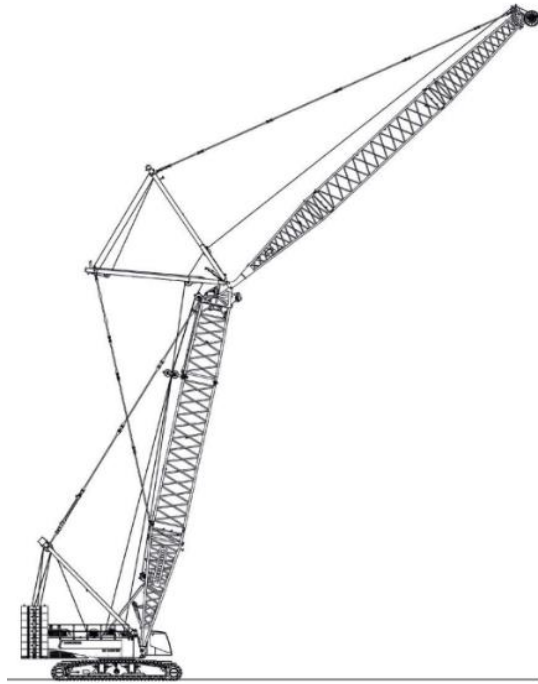
Cranes:

Following completion of the footings and components delivery, a 400-t capacity crawler crane (Fig. 6.4) and an ancillary 120-t capacity mobile crane (Fig. 6.5) would be introduced to assemble the wind turbine components. Figure 6.6 illustrates a typical example of wind turbine erection that involves the use of cranes. The erection of turbines consists of two primary tasks: off-loading and stack-out. Due to its abnormal weight and dimension, the crawler crane would be transported in sections and assembled on site. On the other hand, the mobile crane was likely to be transported to the site using a low bed semi-trailer. The weight of each main component of the crawler crane is summarized in Table 6.3.

Table 6.3 Crawler crane components

Component	Weight (T)
Basic machine	46
2 x Crawler side frame	35 (Each)
5 x Boom sections	26 (Total)
6 x Luffing jib sections	13 (Total)
A-Frame	6
Basic counterweight slab	20
12 x Counterweight slab	10 (Each)
2 x Upper counterweight slab	5 (Each)
2 x Car body counterweight slab	20 (Each)
Load hook	6.5

Source: Liebherr group (2023)



Source: Liebherr group (2023)

Figure 6.4 LR 1400 SX Crawler crane



Source: Manitowoc (2023)

Figure 6.5 GMK5120L Mobile crane



Source: PMV Middle East

Figure 6.6 Wind turbine assembly

O&M Facility

The Operations and Maintenance Facility (O&M Facility) serves as the primary administrative building throughout the operational phase of the Project, with its primary objective being to facilitate ongoing maintenance and operation of the wind farm, as well as to the temporary use during the construction phase. This includes tasks such as monitoring and controlling the wind turbines, storing necessary spare parts and equipment, etc. During construction phase, the O&M Facility can serve as temporary offices and welfare facilities for workers. Ideally, the O&M Facility is located at the same site as the on-site substation in order to minimize site disturbance. Within the facility, it was assumed to include a main control room, amenities for staff, equipment and material storage areas, and a car park. To accommodate these, 15 portacabins were assumed to be transported to the site via lowbed trailer to create the O&M Facility.

Electrical works

To facilitate the widespread distribution of the generated electricity, the generated power from the wind turbines would be transferred to the electricity grid through an on-site substation. Commonly, the electrical works would include:

- The installation of low-voltage underground reticulation cables and overhead powerlines to link the wind turbines to the substation;
- The installation of on-site substation to elevate the voltage from the reticulation voltage to the appropriate transmission voltage compatible with the transmission grid;
- The installation of high-voltage transmission line, mounted on transmission towers, extended from the project site towards the connection point of the transmission network;
- The installation of control cables to connect each of the turbines to a building dedicated to site monitoring.

Electricity reticulation cables:

To enable electrical connection to transmission network, the individual turbines would be connected to each other and then being linked to a substation via low-voltage underground cables and overhead powerlines. When connecting wind turbines along ridgelines and in the flat areas, it is generally preferred to use underground cables, whereas overhead power lines are preferred for conducting power between adjacent ridges and crossing natural or artificial obstacles to connect groups of wind turbines to the substation with less ground disturbance.

Approximately 35 km of underground cables was assumed to be necessary, requiring the excavation of trenches around 2 m wide and 1 m deep (Fig. 6.7), whenever possible, the trenches will be placed within or close to access tracks in order to minimize ground disturbance. The 1000 mm wide x 500 mm deep trenching sand (2 tonne/m³, 20% bulking factor) was then assumed to be placed at the bottom of the trench to serve as a cushion for the cables and provide drainage. The sand as a protective layer helps to distribute the load on the cable evenly, reducing the risk of damage to the cable due to external pressure. Once the cable is installed and covered with the trenching sand, the trench is then backfilled with soil and compacted. Assuming that approximately 2 km of overhead powerlines (Fig. 6.8) would be necessary, it was planned that these powerlines would be mounted on single pole type structures with a height of 12 meters and a spacing of 80 meters.



Source: NWS (2011)

Figure 6.7 Typical cable trenching



Source: NWS (2011)

Figure 6.8 Typical overhead powerline pole

It was assumed that the underground cables and overhead powerlines would be wound onto wooden spools, with each spool containing approximately 2km of cable or powerline. These spools will then be transported to the site using flatbed trailers.

Substation:

It was assumed that the substation facility would occupy an area (including the O&M Facility) of 150 meters by 150 meters on a hardstand area made of 400 mm deep of gravel and crushed stones. A typical substation is shown in Figure 6.9. To step up the reticulation voltage to electricity grid voltage, the substation will include a transformer, the approximate dimension and load of which are detailed in Table 8.4. The transformer would be transported to the site using a specialized trailer. Additionally, the substation would be equipped with circuit breakers, busbars, isolators, control and protection systems, smaller voltage and current transformers, communications equipment, and fire protection. Two or three small buildings, assumed to be made of portacabins for the sake of simplicity in analysis, would be included in the substation to house equipment and facilities necessary for the operation of the substation. These buildings will likely include a switch room and an auxiliary services building.

Table 6.4 Approximate dimension and load of transformer

Component	Height (m)	Width (m)	Length (m)	Weight (t)
Site transformer	4.5	4.5	8	80



Source: NWS (2021)

Figure 6.9 Typical substation for wind farms

Control cable:

The underground control and communication cabling between the wind turbines and the substation for the use of monitoring and operation during operational phase would be installed alongside low-voltage underground cables in the same trenches or mounted on the same poles. The control cable would be wound onto wooden spools, with each spool containing 4 kilometers of cable. The total length of the control cable assumed necessary is 40 kilometers.

High-voltage transmission line:

It was assumed that the transmission line will span a length of 5 kilometers and will be supported by steel transmission towers extending from the substation to the grid connection point. The towers were expected to be roughly 45 meters in height and would be spaced at intervals of 300 to 400 meters, depending on the site's topography.

In order to facilitate construction and maintenance activities, a 3-meter-wide access track with 3 km length, constructed with 400mm depth of gravel and crushed stones, would be built within the overhead transmission line easement where necessary.

The foundation design and size for each tower will depend on various factors such as the soil type, soil bearing capacity, and expected wind loads. For the sake of simplicity, it was assumed that pile cap foundations will support the transmission towers, with each foundation containing 30 cubic meters of concrete and 4 tonnes of steel.

6.1.2 Operational Phase

Although the operation of wind turbines is largely automated during the operational phase, routine inspections and preventive maintenance will still require visits to be made. The traffic generated by the operation and maintenance of the wind farm typically involves the following activities:

- Turbine maintenance and inspection;
- Turbine components repair and/or replacement;
- Access track maintenance;
- Substation maintenance and inspection.

Up to 15 people per day were expected to conduct routine maintenance and inspections during the operational phase, and up to 10 days of maintenance per year. Wind turbine components may require repair or replacement in the event of unscheduled fault conditions. Considering the robustness and durability of the wind turbines, it was assumed there would be no components subjected to replacement. In the event of a major component repair (assuming 10 repairs throughout the lifetime), a 120-ton mobile crane would be required on site.

6.1.3 Decommissioning Phase

This section outlines a step-by-step approach to evaluating the traffic distribution associated with the post-operational stage of a wind farm development.

After the 25-year project life, the wind farm infrastructure would be dismantled and removed, and the site would be restored to its original condition. The decommissioning of a wind farm involves various tasks, such as the removal of wind turbines, substation, overhead and underground cables, foundations, buildings, and other construction-related activities to restore the site. This process was expected to be a relatively short-term activity, lasting approximately 8 months with 40 workers per day, as compared to the construction phase.

Dismantling of the wind turbine

Before decommissioning each wind turbine, they would be de-energized and safely disconnected from the internal reticulation network of the wind farm. The main components of the wind turbine, such as the hub, nacelle, blade, and tower, would then be disassembled using a 400-ton capacity crawler crane, a 120-ton capacity mobile crane, and other specialist heavy machinery and tools. In order to avoid using the OW/OS hauling unit during the decommissioning phase, the wind turbine components were likely to be dismantled using a jaw cutter, as depicted in Figure 6.10, and then transported by semi-trailers. For the same consideration, the nacelle would also be disassembled into smaller pieces to enable more manageable transportation.



Source: WindEurope (2020)

Figure 6.10 Wind turbine dismantling

Dismantling of the foundation

Following the complete dismantling of the wind turbines, the foundation would also need to be removed. However, in the case of wind turbine foundations made of concrete and measuring about 3 meters in depth, their complete removal may result in excessive disturbance to the soil structure. Therefore, it was anticipated that only the upper 1 meter of the pedestal will be removed and brought to the landfill, leaving the rest of the footing in the ground to minimize ground disturbance.

Once the upper part of the footings has been removed, the site was expected to be placed with clean fill material and re-vegetated. The area would be adequately graded to match the surrounding area's profile and minimize environmental disturbance.

Dismantling of the infrastructure

Substation and O&M facility:

It was anticipated that all equipment, conductors, transformers, parking areas, and buildings within the substation and O&M facility area would be removed. The entire compound would be taken down and removed from the substation site, with the waste material transported to a landfill and the replacement of 200mm-depth seeding soils.

Electrical network:

The underground collection cabling would be extracted from the cable trench using a mechanical tool, which will pull the cable and re-roll it onto a cable drum. Additionally, all overhead powerlines and supporting poles would be completely removed. The transmission line extending from the collector substation to the point of transmission grid connection would also be taken down. The transmission steel towers would be decomposed, and foundations would be dismantled to a depth of 1 meter from the ground and transported to a landfill or recycled.

Access roads and crane pads:

Once the decommissioning activities have been completed, mechanical excavators would fully excavate the wind turbine access road, transmission line access tracks, and hardstands. After the removal works are complete, the access road areas would be de-compacted. Before revegetating the area, the ground would be appropriately graded to align with the slope and contour of the surrounding land.

6.1.4 Traffic Spectrum

According to the proposed development and the associated assumptions described above, the project was expected to generate a total of 143352 two-way vehicle movements over the course of an 18-month construction period, a 25-year operational phase, and an 8-month decommissioning phase.

Out of these, approximately 92922 were estimated to be heavy vehicle movements, 49760 were expected to be car/light vehicle movements (typically employee movements), and 690 were OW/OS hauling unit movements. Table 6.5 provides a breakdown of the detailed composition of the traffic spectrum.

It should be noted that the estimations of traffic in this study assumed that all vehicles would use the same access point to enter and exit the wind farm, resulting in the estimated traffic being the maximum traffic that could be expected on the pavement in the proposed wind farm. However, in actual wind farm development projects, several access points could be observed due to the road networks around the site and the wide distribution of wind turbines on site. Furthermore, for OW/OS hauling units, which have abnormal dimensions, extra turning radii may be required to ensure them to turn the driving direction and exit the site from the same road where they accessed it. In the current study, it was assumed that these vehicles would as well use the same access point to enter and exit the site.

Table 6.5 Traffic Spectrum Estimates for wind plant

Traffic Spectrum Estimates							
1	Construction phase	Quantity	Unit	Vehicle type	Unit per vehicle	Total two-way traffic	Notes
1.1	Site establishment						
	Internal track	172800	t	Dump truck	30	11520	Based on 20 km of roads (8 m wide x 400 mm deep). 2 tonne/m ³ , 20% bulking factor
	Hardstands	126000	t	Dump truck	30	8400	Based on 30 hardstands (70 m length x 50 m wide x 400 mm deep). 2 tonne/m ³ , 20% bulking factor
	Batching plant-Miscellaneous equipment	5	Count	Flatbed trailer	1	10	
	Batching plant-Compound	9600	t	Dump truck	30	640	Based on 1 batching plant (100 m length x 100 m wide x 400 mm deep). 2 tonne/m ³ , 20% bulking factor
	Delivery of equipment for civil works	26	Count	Lowbed trailer	1	52	5 x Excavator; 5 x Bulldozer; 5 x Loader; 5 x Grader; 2 x Roller; 2 x Trencher; 2 x 60-ton capacity crane;
	Delivery of equipment for civil works After construction	26	Count	Lowbed trailer	1	52	5 x Excavator; 5 x Bulldozer; 5 x Loader; 5 x Grader; 2 x Roller; 2 x Trencher; 2 x 60-ton capacity crane.
	Water delivery						
	Non-potable water	8640	kL	Water tanker	20	864	Based on 20 kL each working day
	Potable water	2160	kL	Water tanker	20	216	Based on 5 kL each working day
1.2	Work force	34560	Person	Car/Light vehicle	2	34560	Carpooling factor 2
1.3	Tower footing						
	Cement	27450	t	Dump truck	22.5	2440	
	Aggregate	82350	t	Dump truck	22.5	7320	Based on 610 m ³ concrete per foundation,
	Sand	54900	t	Dump truck	30	3660	typical ratio 1 cement : 1.5 sand : 3 aggregate : 0.6 water,
	Water	10980	kL	Water tanker	20	1098	80 tonnes of steel per foundation.
	Steel work	2400	t	Flatbed trailer	30	160	
	Debris	41300	t	Dump truck	22.5	3672	Based on 30 excavated circular footings (9 m diameter x 3 m deep). 1.5 tonne/m ³ , 20% bulking factor
1.4	Wind turbine delivery and assembly						
	Wind turbine delivery						
	Nacelles	30	Count	Specialized vehicle	1	60	Based on 1 per turbine
	Drive trains	30	Count	Specialized vehicle	1	60	Based on 1 per turbine
	Hubs	30	Count	Specialized vehicle	1	60	Based on 1 per turbine
	Tower sections	150	Count	Specialized vehicle	1	300	Based on 5 tower sections per turbine
	Blades	90	Count	Specialized vehicle	1	180	Based on 3 blades per turbine
	Miscellaneous	60	Count	Flatbed trailer	1	120	Assuming 2 containers of equipment per turbine
	Wind turbine assembly						
	400-t capacity Crawler crane**	10	N.A*	Flatbed trailer	1	40	Based on 10 loads per crane transported and assembled on site
	Counterweight**	190	t	Flatbed trailer	40	20	
	120-t capacity Mobile crane**	1	Count	Specialized vehicle	1	4	
1.5	O&M Facility						
	Site temporary offices, amenities, storage, etc.	30	t	Flatbed trailer	30	2	Assuming 15 portacabins, 2 tonnes/each
1.6	Electrical works						
	Electricity reticulation cables	19	Count	Flatbed trailer	10	4	Based on 37 km cables, 2 km/spool, 3 tonnes/spool
	Trench sand	42000	t	Dump truck	30	2800	Based on 35 km of trench, 1000 mm wide x 500 mm deep trenching sand 2 tonne/m ³ , 20% bulking factor
	Trench debris	105000	t	Dump truck	22.5	9334	Based on 35 km trenching (2 m wide x 1 m deep). 1.5 tonne/m ³

Powerline poles	25	Count	Flatbed trailer	14	4	Based on 2 km overhead powerline, pole spacing 80m, 1 tonne/each
Substation						
Compound	21600	t	Dump truck	30	1440	Based on 1 compound (150 m wide x 150 length x 400 mm deep). 2 tonne/m ³ , 20% bulking factor
Transformer	1	Count	Specialized vehicle	1	2	
Miscellaneous equipment	5	N.A	Flatbed trailer	1	10	Assuming 5 containers of equipment
Storage and operation rooms	6	t	Flatbed trailer	30	2	Assuming 3 portacabins, 2 tonnes/each
Control cable	30	t	Flatbed trailer	30	2	Based on 40 km cables, 4 km/spool, 3 tonnes/spool
High-voltage transmission grid						
Transmission line	25	t	Flatbed trailer	30	2	Based on 5 km transmission line, 1 km/spool, 5 tonnes/spool
Transmission tower	45	Count	Flatbed trailer	2	46	Based on 2 loads per tower transported and assembled on site
Transmission tower - Access road	8640	t	Dump truck	30	576	Based on 3 km of roads (3 m wide x 400 mm deep). 2 tonne/m ³ , 20% bulking factor
Tower foundation						
Cement	675	t	Dump truck	22.5	60	
Aggregate	2025	t	Dump truck	22.5	180	Based on 610 m ³ concrete per foundation,
Sand	1350	t	Dump truck	30	90	typical ratio 1 cement : 1.5 sand : 3 aggregate : 0.6 water,
Water	270	kL	Water tanker	20	28	80 tonnes of steel per foundation.
Steel work	60	t	Flatbed trailer	30	4	
Debris	810	t	Dump truck	22.5	72	Based on 30 m ³ of each foundation, 1.5 tonne/m ³ , 20% bulking factor
2 Operational phase						
Work force	3750	Person	Car/Light vehicle	1	7500	Assuming 15 stuff per day, 10 days per year
120-t capacity Mobile crane	10	Count	Specialized vehicle	1	20	Assuming 10 repairs throughout the lifespan
Miscellaneous	10		Flatbed trailer	1	20	Assuming 1 truck of equipment used in repairing each time
3 Decommissioning phase						
3.1 Dismantling of the wind turbine						
Wind turbines	20442	t	Flatbed trailer	40	1024	Assuming the all the wind components will be decomposited for manageable transportation
400-t capacity Crawler crane**	10	N.A	Flatbed trailer	1	40	Based on 10 loads per crane transported and assembled on site
Counter weight**	190	t	Flatbed trailer	40	20	
120-t capacity Mobile crane**	1	Count	Specialized vehicle	1	4	
3.2 Dismantling of the foundation						
Foundation debris - Concrete	14470	t	Dump truck	30	966	Base on 30 footings, with upper 1m of structure being removed, 2.4 tonne/ m ³
Foundation debris - Steel	800	t	Dump truck	30	54	Base on 30 footings, with upper 1m of structure being removed, 26.7 tonnes steel per 1m of footing
Seeding soil	10900	t	Dump truck	22.5	970	Based on 1.5 tonne/m ³ , 20% bulking factor
3.3 Dismantling of the infrastructure						
Electrical reticulation network						
Electricity reticulation cables	19	Count	Flatbed trailer	10	4	Based on 37 km cables, 2 km/spool, 3 tonnes/spool
Powerline poles	25	Count	Flatbed trailer	14	4	Based on 2 km overhead powerline, pole spacing 80 m, 1 tonne/each
Substation						
Compound	21600	t	Dump truck	30	1440	Based on 1 compound (150 m wide x 150 length x 400 mm deep), 2 tonne/m ³ , 20% bulking factor
Compound - Seeding soil	8100	t	Dump truck	22.5	720	1.5 tonne/m ³ , 20% bulking factor
Transformer	2	Count	Flatbed trailer	1	4	Based on 2 trips for a decomposited transformer

Miscellaneous equipment	5	Count	Flatbed trailer	1	10	Assuming 5 containers of equipment
Storage and operation rooms	6	t	Flatbed trailer	30	2	Assuming 3 portacabins, 2 tonnes/each
Control cable	30	t	Flatbed trailer	30	2	Based on 40 km cables, 4 km/spool, 3 tonnes/spool
High-voltage transmission grid						
Transmission line	25	t	Flatbed trailer	30	2	Based on 5 km transmission line, 1 km/spool, 5 tonnes/spool
Transmission tower	45	Count	Flatbed trailer	2	46	Based on 2 loads per tower transported and assembled on site
Tower foundation - Concrete	1080	t	Dump truck	36	60	Base on 45 footings, with upper 10 m ³ concrete being removed each. 2.4 tonne/ m ³
Tower foundation - Steel	68	t	Dump truck	30	6	Base on 45 footings, with 1.5 tonnes of steel being removed each
Tower foundation - Seeding soil	810	t	Dump truck	22.5	72	Based on 1.5 tonne/m ³ , 20% bulking factor
Transmission tower - Access road	8640	t	Dump truck	30	576	Based on 3 km of roads (3 m wide x 400 mm deep), 2 tonne/m ³ , 20% bulking factor
Access roads and crane pads	298800	t	Dump truck	30	19920	Based on 20 km road, 30 crane pads
3.4 Dismantling of the internal track						
Internal track	172800	t	Dump truck	30	11520	Based on 20 km of roads (8 m wide x 400 mm deep), 2 tonne/m ³ , 20% bulking factor
3.5 Equipment and water delivery						
Equipment & Miscellaneous	10	N.A	Flatbed trailer	1	20	Assuming 10 containers of equipment and miscellaneous material delivery
Non-potable water	3840	kL	Water tanker	20	384	Based on 20 kL each working day
Potable water	960	kL	Water tanker	20	96	Based on 5 kL each working day
3.6 Work force	7680	Person	Car/Light vehicle	2	7680	Carpooling factor 2
Total estimated vehicles					143352	
Total estimated heavy vehicles					92922	
Total estimated OW/OS vehicles					690	
Total estimated car/light vehicles					49740	

*: N.A = Not Applicable, **: Twice transportations

6.2 Solar Farm

Similar to the development of wind farms, the development process of solar farms typically comprises three consecutive stages.

- Phase 1: Construction
- Phase 2: Operation
- Phase 3: Decommissioning

To assess the traffic spectrum to the three development phases, the specific tasks involved in each phase were outlined and their correlations with generated traffic were analyzed in detail in the following subsections. Finally, this analysis led to a presentation of a generic traffic spectrum that could be expected from a proposed solar farm project.

Key Assumptions

This section of the study provides estimates and analysis of a solar traffic spectrum based on several assumptions that have been made regarding the scope of proposed development, construction program, methodology, and material sources. These assumptions include but are not limited to the following:

Proposed development:

The proposed development was a 186 MW capacity of electricity generation work, comprised of 413500 First Solar[®] Series 6 (FS-6445) photovoltaic (PV) modules, where each module is capable of producing 450 W nominal power. It was anticipated that the proposed development would take roughly 12 months to be constructed and would be operational over a period of approximately 30 years.

Solar array arrangement:

The project envisions the installation of PV panels mounted on east-west horizontal single-axis-tracking structures, which were designed to track the sun from east to west. These structures would be arranged in rows and columns oriented towards the north to optimize power generation at the site. It was assumed that each tracker would have the capacity to hold 48 PV panels with a clearance of 20 mm between modules to allow for thermal expansion. The trackers would be arranged longitudinally in a column to form a string array, with six trackers in each column. Additionally, 39 string arrays would be arranged parallel to form a 5 MW output capacity of array block, which would consist of approximately 11232 solar panels (Fig. 6.11). The array block would feed a Power Conversion Unit (PCU) located within the block. The pitch distance of 6m was selected to minimize shading effects between adjacent columns and to ensure overall energy efficiency. The proposed solar development would comprise 38 array blocks, each with a 5 MW output capacity

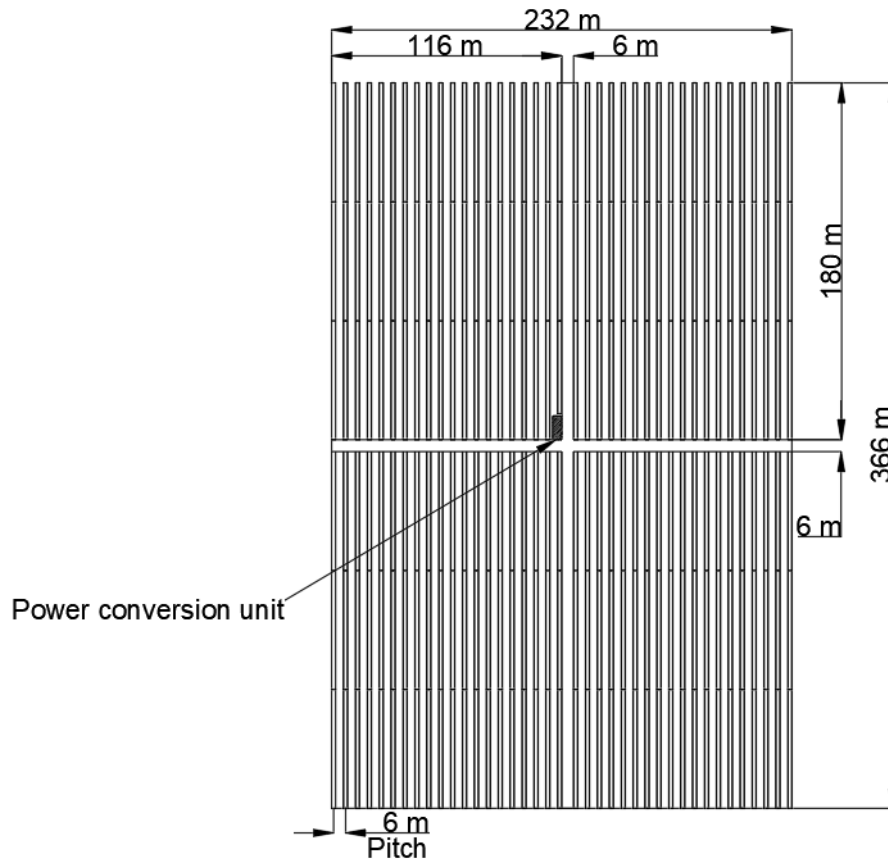


Figure 6.11 10 MW array block showing location of PCU and access track

To facilitate transport during installation, construction, and ongoing maintenance, internal access tracks would be constructed to each PCU and the substation. Onsite tracks would be made of 300mm-depth compacted gravel and crushed stone and would have an approximate width of 6 m to ensure safe delivery, unloading, and installation of key components such as PCUs, PV panels, and switch equipment. The proposed design includes two internal access tracks per 5MW array block, originating from the center and arranged perpendicular to each other (Fig. 6.11). Additionally, tracks were also expected to be constructed in the vicinity of adjacent array blocks (Fig. 6.12). Assuming a flat site and the ability to place all array blocks together, approximately 600 m of internal roads would be required within each 5MW array block, with a total of 42.7km, say 43 km, expected to be constructed for the proposed solar development.

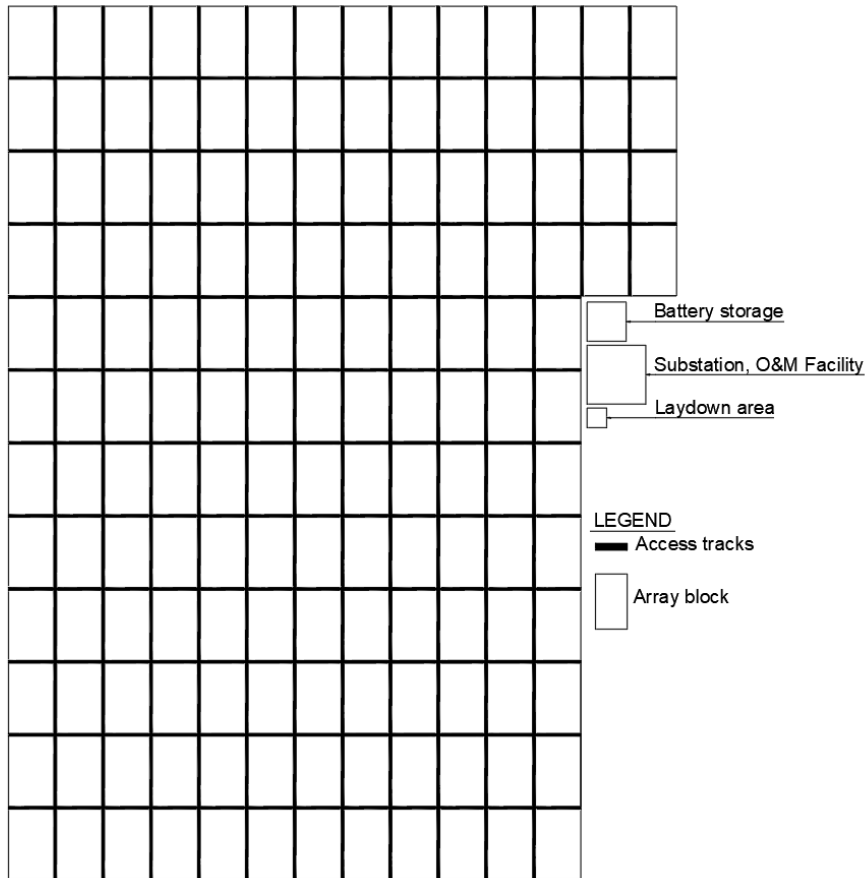


Figure 6.12 Proposed solar development arrangement

6.2.1 Construction Phase

In this section, the construction activities were presented in sequential order, along with a discussion on the potential factors that may impact traffic generation. The construction phase was anticipated to span approximately 9 months.

Site Preparation:

To ensure timely installation of roads, solar equipment, cabling, and infrastructure, site preparation activities would commence immediately across the entire development area. Given that the site is generally assumed flat or to have consistent slope and be largely free of dense vegetation and trees, minimal preparation would be required such as removing any timber or rock debris. During the site preparation phase, construction vehicles and equipment would be mobilized and made available for ongoing and future use. The construction equipment that was anticipated to be used onsite includes:

2 x dozer or equivalent for levelling and road development; 2 x excavator for earthworks; 2 x grader for road development and levelling activities; 1 x mulcher for the mulching; 2 x vibrating roller for road construction; 2 x piling rig for installing PV piles; 2 x mobile crane for the lifting of loads, erection of steel and movement of heavy plant; 2 x trenchers for the installation of underground conduits and cabling; 2 x wheel loader and 1 x container of hand power tools and miscellaneous equipment.

Internal access and foundation compounds:

To facilitate construction and ongoing maintenance, internal access tracks capable of supporting light traffic would be constructed to each PCU and the solar substation. The 30 km internal roads would be made of compacted gravel and crushed stone with a depth of 400 mm, and an approximate width of 6 m as previously assumed. In addition, various foundation compounds, including those for the substation, site facilities, PCUs, battery storage, and a construction laydown area, would be established within the development footprint. It was assumed that site facilities, such as the site office and amenities, would be accommodated in the same area as the substation. The estimated dimensions of each compound are provided in Table 6.6.

Table 6.6 The dimensions of construction compounds

Foundation Compound	Length (m)	Width (m)	Quantity	Note
Substation	150	150	1	All the compounds constructed with 400mm depth of concrete mixture
PCUs	12	4.5	38	
Battery storage	100	100	1	
Laydown area	50	50	1	

Water:

On a daily basis, it was anticipated that up to 15 kiloliters (kL) of non-potable water would be necessary, primarily for dust suppression and other construction-related activities. Additionally, 8 kL of potable water would be required each working day during the construction phase.

Work force

Throughout a 12-month period with a 6-day work week, it was anticipated that approximately 100 construction workers would be required on a daily basis during the construction phase. The construction workforce would consist of a variety of skilled and semi-skilled positions. It was expected that the majority of construction staff would utilize carpooling for transportation to and from the site.

Operation and Maintenance (O&M) facility

The proposed O&M facility was anticipated to be co-located with the proposed substation, adjacent to the PV arrays. The facility would consist of several structures, including a temporary site office, a control room, car park, and staff amenities such as toilets, showers, a lunchroom, and a first aid room. Additionally, a maintenance building would be constructed to provide storage for spare parts and maintenance equipment, as well as a workshop. For ease of analysis, all buildings were expected to be constructed with demountable portacabins.

Installation

Once the site preparation is complete, the supporting structures and solar modules will be installed. The proposed solar development would consist of up to 413500 individual solar panels, the dimensions and packing information of which can be found in Table 6.7. Each solar panel would be attached to a metal mounting structure that would be driven or screwed into the ground at a depth of approximately 2-3m,

without requiring excavation or the use of concrete to minimize ground disturbance. To track the movement of the sun, the PV mounting structures (as shown in Figure 6.13) would be equipped with automated tracker units that slowly track the sun's movement in a single axis. Based on the key assumption made earlier regarding the solar arrangement, it was estimated that 8892 trackers would be installed, assuming each weighted one tonne and measuring 60 m in length, 2 m in width, and 1.8 m in height above the ground.

Table 6.7 Dimension and packing information of PV panel

Dimension of a PV panel		Packing Information	
Length	2009 mm	Modules Per Pack	27
Width	1232 mm	Pack Dimensions	2200 x 1300 x 1164mm
Thickness	49 mm	Pack Weight	1032 kg
Weight	34.5 kg	Packs per 12-m Container	18

Source: First Solar (2023)



Source: Solar Power World

Figure 6.13 A typical illustration of PV panels wired on one portrait tracker

Electrical Collection System

Following the installation of the PV modules, cable trenches would be excavated, and Alternating Current (AC) and Direct Current (DC) cables would be laid. The PCUs would then be installed in each array block and connected to the onsite substation, where the electricity would be distributed to the transmission grid after voltage is stepped up by a transformer installed at the substation.

DC&AC cabling:

The typical collector system for the solar farm will begin with DC reticulation cabling running along each solar array and underground to connect each PV module in a string to the corresponding PCU for each array block. Inverters installed within the PCUs will convert the DC-generated electricity to AC at medium voltage, which will then be transformed at the onsite substation via underground AC cables. To install the DC/AC cabling underground, trenches with a depth of 1 m and a width of 2 m would be excavated. The trenches would then be backfilled with trenching sand (2 tonne/m³, 20% bulking factor) of 1000 mm wide x 500 mm deep at the bottom to

serve as a cushion for the cables and provide drainage. Based on the earlier assumptions regarding the array arrangement, it was estimated that approximately 9 km of DC cable and 11 km of AC cable would be required.

Power conversion unit:

Each array block would include a PCU, which houses the central inverters, step-up transformers, and switchgear required to convert the DC electricity collected from the PV panels into medium voltage AC electricity. The PCU, along with its associated equipment, was designed to be housed within a shipping container mounted on concrete footings or piles, making it easily transportable and installable onsite. A typical PCU is approximately 10 meters in length, 2.5 meters in width, and 3 meters in height, as shown in Figure 6.14. There would be 38 PCUs estimated to be installed on the site.



Source: NWS (2022a)

Figure 6.14 Typical illustration of a PCU within the array.

Substation:

To facilitate the connection of the proposed solar farm to the electricity transmission grid, an electrical substation would be constructed on site. The substation would consist of a main step-up transformer and associated equipment such as circuit breakers and high voltage conductors, etc. It was assumed that the transformer weighs 80 tonnes (Fig. 6.15), while the associated equipment would be transported to the site via 10 containers.



Source: FRV (2023)

Figure 6.15 Typical main transformer in solar farm

Electricity transmission line:

The proposed solar farm would connect to the transmission grid via the newly established substation, using a high-voltage transmission line. The transmission line was estimated to be 5 kilometers in length and supported by steel transmission towers spaced at 400-meter intervals, with a height of approximately 45 meters. To facilitate construction and maintenance activities of the transmission towers, a 3-kilometer-long access track, 3 meters wide and built with 400mm of gravel and crushed stones, would be constructed within the transmission line easement where necessary. The foundation design and size for each tower will depend on various factors. It was expected pile cap foundations would be used to support the transmission towers, with each foundation requiring 30 cubic meters of concrete and 4 tonnes of steel.

The Battery Energy Storage System (BESS):

The proposed development would also include battery storage (Fig. 6.16) on the site to address the intermittent nature of solar energy. Battery storage systems can be used to smooth the fluctuating energy output of the solar farm, store excess energy during low demand periods, and provide electricity during high demand periods or when solar energy is unavailable, such as at night. Additionally, energy storage can contribute to sustainable outcomes by combining clean energy generation with clean energy storage.



Source: NWS (2022a)

Figure 6.16 Typical battery storage units, located together

The proposed solar farm was assumed to include a provision for a battery storage facility consisting of approximately 25 containers (12 m long by 2.5 m wide by 3.0 m high) containing lithium-ion batteries in containerized packs. The battery storage infrastructure would be installed in a designated area near the substation once the solar farm is operational, rather than being distributed throughout the site. The BESS compound would be fully fenced and secured, approximately 100 m by 100 m in size, the compound components would include battery containers, bidirectional inverters that convert power from DC to AC and allow charging of the batteries via AC to DC rectifiers, protection devices, cooling systems, and a control system. It was anticipated that after 15 years the batteries would be replaced.

Security and fencing

Prior to the commissioning of the proposed solar farm, a security system would be constructed. The perimeter of the solar farm, substation site, BESS would be secured with a 2.5 m height chain wire fence with barbed wire topping (Fig. 6.17). It was anticipated that 8900 m length of fence would be transported to site with 12-m shipping containers (150 m of fence packed in each container).



Source: Yujun Metal Mesh Co., Ltd.

Figure 6.17 Chain wire fence with barbed wire topping

6.2.2 Operational Phase

The project was expected to remain in operation for a period of up to 30 years, during which a number of operational activities would be undertaken, such as maintenance of solar panels, monitoring of the solar farm's performance, inspection of the installation, site security response, and vegetation management within the development footprint.

On average, it was assumed that 10 staff members would visit the site once a month during the operational phase, and they would likely drive cars or light vehicles to the site each working day using available roads. Water would be needed for panel cleaning, site maintenance, and staff amenities. Under normal operating conditions, it was estimated that up to 1 ML of water would need to be transported to the site per year by water trucks.

6.2.3 Decommissioning Phase

The objective of this stage was to restore the site to its original land capability, making the solar farm development reversible. The specific decommissioning procedures for the project will vary depending on the future use of the project location. For instance, if the land is intended for agricultural use, the decommissioning process will involve restoring the land to its productive state. Therefore, this section outlined a generic decommissioning plan. The decommissioning process would span a period of 6 months and involve the employment of 30 workers each day.

Upon reaching the end of the operational life of the proposed development, decommissioning of the development area would take place, involving the removal of all above ground infrastructure. Key elements of infrastructure decommissioning were expected to include:

- removal of PV modules, and removal of tracker mounting posts, mounting frames;
- removal of all buildings and equipment;
- removal of and cabling, transmission line, transmission towers; and
- removal of fencing;

Following infrastructure removal, the following were expected to be undertaken to re-instate the site to pre-existing land use:

- removal of internal tracks and roads;
- removal of foundation compounds; and
- deep ripping of any compacted areas.

6.2.4 Traffic Spectrum

As per the proposed development and related assumptions mentioned above, the project was predicted to generate 87044 two-way vehicle movements during a 12-month construction period, a 30-year operational phase, and a 6-month decommissioning phase. Out of which, nearly 46718 movements were expected to be heavy vehicles, 40320 movements were anticipated to be car/light vehicle movements (primarily employee movements), and only 6 movements were limited to OW/OS hauling units. Table 6.8 provides a detailed breakdown of the traffic spectrum composition.

It is worth mentioning that, to simplify the traffic estimations for the solar farm, the same assumptions were used as those in the wind farm traffic estimation. All vehicles were assumed to enter and exit the solar farm via a single access point, leading to the estimated traffic volume representing the maximum expected traffic on the pavement within the proposed solar farm.

Table 6.8 Traffic Spectrum Estimates for solar plant

Traffic Spectrum Estimates							
1	Construction phase	Quantity	Unit	Vehicle type	Unit per vehicle	Total two-way traffic	Notes
1.1	Site preparation						
	Internal track	185760	t	Dump truck	30	12384	Based on 43 km of roads (6 m wide x 300 mm deep). 2 tonne/m ³ , 20% bulking factor
	Foundation compounds						
	Substation	21600	t	Concrete mixer	14.5	2980	Based on 150 m length x150 m wide x 400 mm deep. 2.4 tonne/m ³
	Power conversion unit	1970	t	Concrete mixer	14.5	272	Based on 38 PCUs (12 m length x4.5 m wide x 400 mm deep). 2.4 tonne/m ³
	Battery storage	9600	t	Concrete mixer	14.5	1326	Based on 100 m length x100 m wide x 400 mm deep. 2.4 tonne/m ³
	Laydown area	2400	t	Concrete mixer	14.5	332	Based on 50 m length x50 m wide x 400 mm deep. 2.4 tonne/m ³
	Delivery of equipment for civil works**	17	Count	Lowbed trailer	1	68	2 x Dozer, 2 x Excavator, 2 xGrader, 2 x Vibrating Roller, 2 x Piling Rig, 2 x Mobile Crane 2 x Trenchers, 1 x Container miscellaneous equipment, 2 x Wheel loader
	Water delivery						
	Non-potable water	4320	kL	Water tanker	20	432	Based on 15 kL each working day
	Potable water	2304	kL	Water tanker	20	232	Based on 8 kL each working day
1.2	Work force	28800	Person	Car/Light vehicle	2	28800	Carpooling factor 2
1.3	O&M Facility						
	Site temporary offices, amenities, storage, etc.	20	t	Flatbed trailer	30	2	Assuming 10 portacabins, 2 tonnes/each
1.4	Installation						
	Solar panel	10212	t	Flatbed trailer	19	1076	Based on 413500 PV panels, 27 modulus per pack, 12 packs per container, 19 tonne/container
	Tracker frame	8892	t	Flatbed trailer	40	446	Based on 8892 tracker frames, each measuring 60 m in length, 2m in width, 1 tonne/tracker frame
1.5	Electrical collection system						
	DC&AC cabling	30	t	Flatbed trailer	30	2	Based on 20 km cables, 2km/spool, 3 tonne/spool
	Trench sand	24000	t	Dump truck	30	1600	Based on 20 km of trench, 1000 mm wide x 500 mm deep trenching sand, 2 tonne/m ³ , 20% bulking factor
	Trench debris	45000	t	Dump truck	22.5	4000	Based on 35 km trenching (2 m wide x 1 m deep). 1.5 tonne/m ³
	Power conversion unit	380	t	Flatbed trailer	10	76	Based on 38 PCU, each PCU is housed in a 10-m shipping container, assumed 10 tonne/each
	Substation						
	Transformer	1	Count	Specialized vehicle	1	2	
	Miscellaneous equipment	5	N.A	Flatbed trailer	1	10	Assuming 5 containers of equipment
	The Battery Energy Storage System	750	t	Flatbed trailer	15	100	Assuming battery storage facility consisting of 25 containers, being replaced after 15 years, 15 tonne/each
	High-voltage transmission grid						
	Transmission line	25	t	Flatbed trailer	30	2	Based on 5 km transmission line, 1 km/spool, 5 tonne/spool
	Transmission tower	24	Count	Flatbed trailer	1	48	Based on 2 loads per tower transported and assembled on site
	Transmission tower - Access road	8640	t	Dump truck	30	576	Based on 3 km of roads (3 m wide x 400 mm deep). 2 tonne/m ³ , 20% bulking factor
	Tower foundation						
	Concrete	870	t	Concrete mixer	14.5	120	Based on 30 m ³ concrete (2.4 tonne/m ³), 4 tonnes of steel per foundation.
	Steel work	48	t	Flatbed trailer	30	4	
	Debris	360	t	Dump truck	22.5	32	
	120-t capacity mobile crane**	1	Count	Specialized vehicle	1	4	
1.6	Security and fencing						
	2.5m high chain wire fence	60	Count	Flatbed trailer	1	120	Based on 8900 m fencing, 150 m in one shipping container

2	Operational phase						
	Work force	3600	Person	Car/Light vehicle	1	7200	Assuming 15 staff per day, 10 days per year
	Water	30000	kL	Water tanker	20	3000	Assuming 10 repairs throughout the lifespan
	Miscellaneous	10	Count	Flatbed trailer	1	20	Assuming 10 loads of equipment will be required
3	Decommissioning phase						
	3.1 Dismantling of PV panels and trackers						
	Solar panel	10212	t	Flatbed trailer	19	1076	Based on 413500 PV panels, 27 modulus per pack, 12 packs per container, 19 tonne/container
	Tracker frame	8892	t	Flatbed trailer	40	446	Based on 8892 tracker frames, each measuring 60 m in length, 2m in width, 1 tonne/tracker frame
	3.2 Dismantling of electrical collection system						
	DC&AC cabling	30	t	Flatbed trailer	30	2	Based on 20 km cables, 2 km/spool, 3 tonne/spool
	Power conversion unit	380	t	Flatbed trailer	10	76	Based on 38 PCU, each PCU is housed in a 10-m shipping container, assumed 10 tonne/each
	Substation						
	Transformer	2	Count	Flatbed trailer	1	4	Based on 2 trips for a decomposited transformer
	Miscellaneous equipment	5	N.A	Flatbed trailer	1	10	Assuming 5 containers of equipment
	The Battery Energy Storage System	25	Count	Flatbed trailer	1	50	Assuming battery storage facility consisting of 25 containers
	High-voltage transmission grid						
	Transmission line	25	t	Flatbed trailer	30	2	Based on 5 km transmission line, 1 km/spool, 5 tonne/spool
	Tower foundation - Concrete	120	t	Dump truck	30	8	Base on 12 footings, with upper 10 m ³ concrete being removed
	Tower foundation - Steel	16	t	Dump truck	30	2	Base on 12 footings, with upper 10 m ³ concrete being removed
	Transmission tower	24	Count	Flatbed trailer	1	48	Based on 2 loads per tower transported and assembled on site
	Transmission tower - Access road	8640	t	Dump truck	30	576	Based on 3 km of roads (3 m wide x 400 mm deep). 2 tonne/m ³ , 20% bulking factor
	3.3 Dismantling of fencing						
	2.5m high chain wire fence	60	Count	Flatbed trailer	1	120	Based on 8900 m fencing, 150 m in one shipping container
	3.4 Dismantling of foundation compounds						
	Substation	21600	t	Dump truck	30	1440	Based on 150 m length x150 m wide x 400 mm deep. 2.4 tonne/m ³
	Power conversion unit	1970	t	Dump truck	30	132	Based on 38 PCUs (12 m length x4.5 m wide x 400 mm deep). 2.4 tonne/m ³
	Battery storage	9600	t	Dump truck	30	640	Based on 100 m length x100 m wide x 400 mm deep. 2.4 tonne/m ³
	Laydown area	2400	t	Dump truck	30	160	Based on 50 m length x50 m wide x 400 mm deep. 2.4 tonne/m ³
	3.5 Dismantling of O&M Facility						
	Site temporary offices, amenities, storage, etc.	20	t	Flatbed trailer	30	2	Assuming 10 portacabins, 2 tonne/each
	3.6 Dismantling of internal track						
	Internal track	185760	t	Dump truck	30	12384	Based on 43 km of roads (6 m wide x 300 mm deep). 2 tonne/m ³ , 20% bulking factor
	3.7 Equipment and water delivery						
	Equipment & Miscellaneous	10	N.A	Flatbed trailer	1	20	Assuming 10 containers of equipment and miscellaneous material delivery
	Non-potable water	2160	kL	Water tanker	20	216	Based on 15 kL each working day
Potable water	432	kL	Water tanker	20	44	Based on 3 kL each working day	
3.8 Work force							
	4320	Person	Car/Light vehicle	2	4320	Carpooling factor 2	
Total estimated vehicles						87044	
Total estimated heavy vehicles						46718	
Total estimated OW/OS vehicles						6	
Total estimated car/light vehicles						40320	

* N.A = Not Applicable, **: Twice transportations

6.3 Estimations of Equivalent Single Axle Loads

Following the identification of various truck types and their corresponding quantities for wind and solar farm developments, the generated traffic was subsequently homogenized into an 80 kN single-axle with dual wheels as specified in the AASHTO pavement design guide. This was done to ensure the traffic considerations in the mechanistic-empirical pavement design method applied in this study could be accommodated in the subsequent flexible pavement designs. To achieve this, the concept of equivalent axle load factor, as outlined in Annex, was employed in the process of traffic homogenization.

Prior to estimating the equivalent axle load factors for each of axles within a vehicle, it is essential to obtain the weight on each individual axle. This weight comprises the unladen weight distributed on each axle from the self-weight of the vehicle in question, which could be derived from the manufacturer's specifications of the vehicle, and the corresponding loads distributed from the payload carried on the vehicle on each axle. To account for the variations in payload weight, which depend on the types of cargo being transported, the distribution of this weight may not be uniform across all axles. Therefore, it was necessary to define the payload distribution factors on each axle of the vehicles included in this analysis.

6.3.1 Determinations of Axle Load Distributions

In order to define load distribution factors for heavy vehicles in a rational and effective way, in the present study, a modeling approach was employed based on a previous study conducted by Alexander Grakovski et al. in 2020. The authors evaluated the load distributions on an articulated vehicle (i.e., dry van trailer) using an analogy to a multi-span continuous beam with hinges. The axle loads of the articulated vehicle were calculated based on the assumed multi-span beam system using a statically indeterminate structural analysis and a system of nonlinear equations solved by a nonlinear programming method in MATLAB®, respectively. The results obtained from two methods were compared to the actual measurements of axle loads obtained from a weighing system on the same vehicle. In such a comparison, the researchers observed a deviation of 2% to the results obtained from the statically indeterminate structural analysis, and a deviation of 1% to the results derived from the nonlinear programming method. Considering the accuracy of both analytical methods for determining load distributions and the challenges associated with using the second method, the present study employed the statically indeterminate structural analysis to determine the axle loads of vehicles. As for specialized hauling units employed in transporting the wind turbine components, due to their complex configurations and connections of the composing components, the readily available analysis of

transport of wind turbine equipment for Rye Park wind farm (Tilt Renewables Australia Pty Ltd, 2022) was adopted in the present study.

6.3.1.1 Heavy Vehicles

In the following, the calculations of the load distribution factors to the heavy vehicles considered in this study, including lowbed trailers, flatbed trailers, concrete mixers, and dump trucks, will be presented.

Flatbed trailer

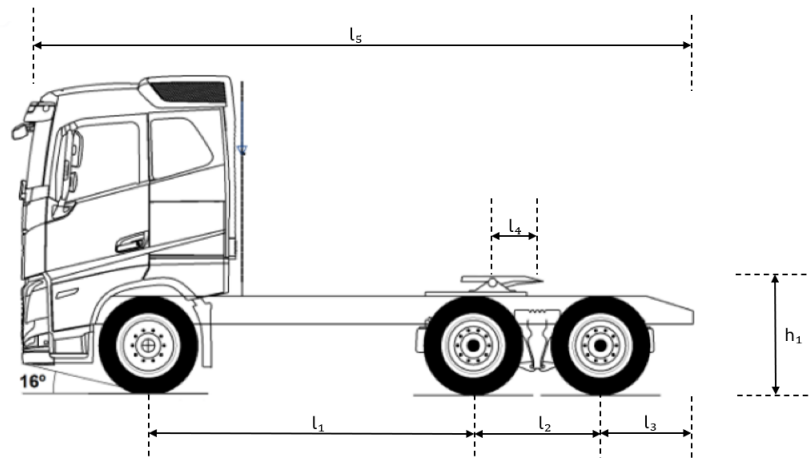
Flatbed trailers are typically designed and used for transporting a variety of cargos that cannot be fit inside a closed trailer, such as powerline poles, portacabins, containers, or oversized cargos that require a flat platform for transport. The trailer consists of two components articulated together, a detachable front section, known as the tractor, and an articulated wheeled semi-trailer on which the cargos placed, the semi-trailer in this case is a flat deck without any sides or roof, making it easy to load and unload cargo from any direction. Figure 6.18 provides a typical example of a flatbed trailer.



Source: Max Trailer

Figure 6.18 A typical flatbed semi-trailer

In this study, the chosen tractor was a VOLVO® FH 16 6x4 Tractor with a maximum gross combination weight of 640 kN, as depicted in Figure 6.19.



Source: Modified from Volvo Trucks

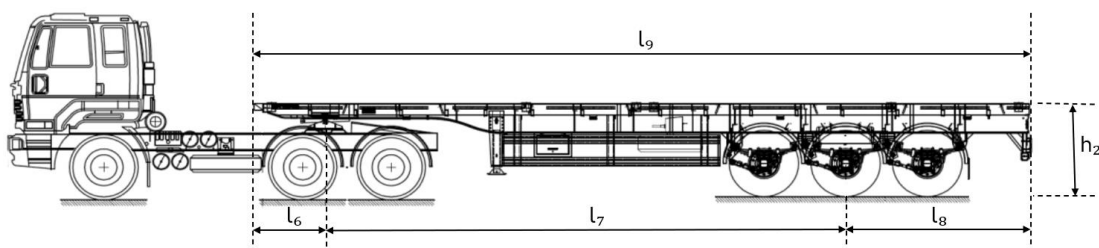
Figure 6.19 VOLVO® FH 16 Tractor

The dimensions and unladen axle weights of the tractor were obtained from its manufacture specification and are presented in Table 6.9.

Table 6.9 Dimensions and unladen axle weights of tractor

Dimensions (m)					
l_1	l_2	l_3	l_4	l_5	h_1
3.00	1.37	1.00	0.50	6.73	Variable
Unladen axle weights (kN)					
Front single axle			Rear tandem axle		
52			38		

Furthermore, this study has chosen a flatbed semi-trailer made by SATRAC®. Figure 6.20 depicts the configuration that the semi-trailer connected onto the chosen tractor.



Source: Modified from SATRAC®

Figure 6.20 Three-axle flatbed semi-trailer

Through accessing the manufacturer's specifications, the dimensions and tare weight of the semi-trailer can be acquired. In the present study, the tare weight of

the flatbed semi-trailer was found to be 82 kN as per the manufacturer's specifications. It was assumed that the tare weight of the flatbed semi-trailer was distributed such that one-third of its weight was supported by the saddle/fifth-wheel (where a towed semi-trailer attaches to the tractor and facilitating vehicle articulation for the vehicle around the vertical axis), while the remaining two-thirds of the weight was loaded onto the rear tridem axle group. The dimensions and corresponding axle weights are listed in Table 6.10.

Table 6.10 Dimensions and unladen axle weights of flatbed semi-trailer

Dimensions (m)					
l_6	l_7	l_8	l_9	h_2	
1.00	8.35	2.95	12.30	1.50	
Unladen weight distributions (kN)					
Saddle			Rear tridem axle		
27			55		

As per the modeling approach described earlier, to determine the load distribution factors on each axle from the load of cargo, a corresponding computational scheme of the tractor and semi-trailer was depicted in Figure 6.21, represented as two rigid beams stacked one above the other. In this model, the tractor was represented as a simply supported rigid beam, with the front single axle and rear tandem axle group being modeled as two supports. It was assumed that the load acting on the tandem axle group is evenly supported by the two axles within the group. The semi-trailer was also considered a two-support beam, with the saddle placed on the tractor serving as the front support, and the tridem axle group modeled as the second support where the middle axle of the tridem axle was located.

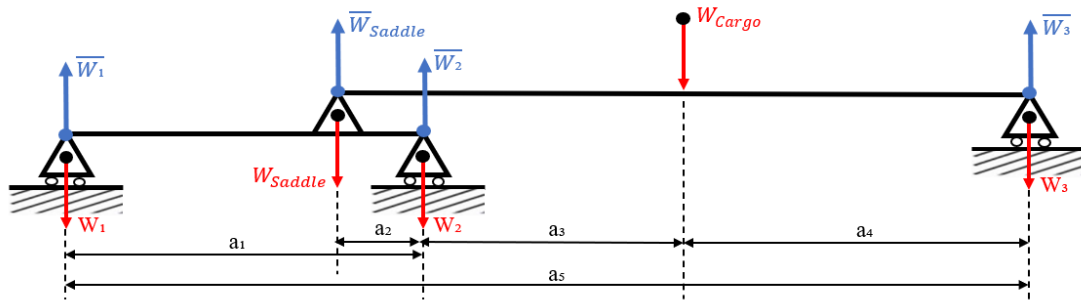


Figure 6.21 Computational static model of flatbed trailer

As demonstrated in Figure 6.21, the flatbed trailer was represented as a static structure, with W_i ($i=1,2,3$) and W_{Saddle} indicate the load acting on the i -th axle or axle group and the saddle distributed from the cargo load W_{Cargo} . For the sake of simplicity, the gravity center of the load of cargo was assumed always to be positioned in the middle of the semi-trailer. The reactions of the i -th axle or axle

group and saddle were represented by \overline{W}_i ($i = 1,2,3$) and \overline{W}_{Saddle} , respectively. It should be noted that the flatbed trailer was modeled in a static state, considering only the loads and reactions acting vertically, with the horizontal reaction and bending moment reaction on the saddle equal to zero.

By knowing the load of cargo and distance of the gravity center of the loads on the semi-trailer, the reactions on the saddle and tridem axle group can be determined as following:

$$\sum M_{Saddle} = 0, \overline{W}_3 \cdot (a_2 + a_3 + a_4) - W_{Cargo} \cdot (a_2 + a_3) = 0 \quad 6.1$$

Where:

- M_{Saddle} is the moment calculated around saddle, in $\text{kN} \cdot \text{m}$;
- \overline{W}_3 is the reaction of tridem axle of the flatbed trailer, in kN ;
- W_{Cargo} is the load of cargo, in kN ;
- a_4 is the distance of gravity center of cargo from rear tridem axle, in m ;
- a_2 is the distance between saddle and rear axle of tractor, in m ;
- a_3 is the distance measuring from the gravity center of cargo to rear axle of tractor, in m .

Then,

$$\overline{W}_3 = W_{Cargo} \cdot \frac{a_2 + a_3}{a_2 + a_3 + a_4} \quad 6.2$$

$$\overline{W}_{Saddle} = W_{Cargo} - \overline{W}_3 \quad 6.3$$

Where:

- \overline{W}_{Saddle} is the reaction on saddle, in kN ;

To determine the loads distributed on the axles of the tractor, the beam model of tractor was solely considered, the corresponding reactions can be defined as follows:

$$\sum M_1 = 0, \overline{W}_2 \cdot a_1 - W_{Saddle} \cdot (a_1 - a_2) = 0 \quad 6.4$$

Where:

- M_1 is the moment calculated around the front axle of tractor, in $\text{kN} \cdot \text{m}$;
- \overline{W}_2 is the reaction of tandem axle of tractor, in Kn ;

- W_{Saddle} is the load distributed from cargo acting on the saddle, with its absolute value equal to the reaction on the saddle, in kN;
- a_1 is the distance between two axles of tractor, in m;

Then,

$$\overline{W}_2 = \overline{W}_{Saddle} \cdot \frac{a_1 - a_2}{a_1} \quad 6.5$$

$$\overline{W}_1 = W_{Saddle} - \overline{W}_2 \quad 6.6$$

Considering the load of cargo equals the unity, the load distribution factors for each axle can be defined as follows:

$$f_1 = \left(1 - \frac{a_2 + a_3}{a_2 + a_3 + a_4}\right) \cdot \frac{a_2}{a_1} \quad 6.7$$

$$f_2 = \left(1 - \frac{a_2 + a_3}{a_2 + a_3 + a_4}\right) \cdot \frac{a_1 - a_2}{a_1} \quad 6.8$$

$$f_3 = \frac{a_2 + a_3}{a_2 + a_3 + a_4} \quad 6.9$$

Where:

- f_1 is the load distribution factor of front axle of tractor;
- f_2 is the load distribution factor of rear axle of tractor;
- f_3 is the distribution factor of rear axle of semi-trailer;

By knowing the distances provided previously, specifically $a_1=3.185$ m, $a_2=0.500$ m, $a_3=3.675$ m, and $a_4=4.175$ m, the load distribution factors were calculated and are presented in Table 6.11.

Table 6.11 Load distribution factors of flatbed semi-trailer

f_1	f_2	f_3
0.08	0.42	0.50

Consequently, by adding the unladen weight of each axle to the corresponding load distributed from the cargo, the axle loads of the analyzed flatbed trailer can be represented as shown in Table 6.12.

Table 6.12 Axle loads distribution of flatbed trailer (kN)

Front axle - Tractor	$= W_1^{Tare} + 0.08 \cdot W_{Cargo} + 0.84 \cdot W_{Saddle}^{Tare}$ $= 52 + 0.08 \cdot W_{Cargo} + 22.7$ $= 74.7 + 0.08 \cdot W_{Cargo}$
Rear tandem axle - Tractor	$= W_2^{Tare} + 0.42 \cdot W_{Cargo} + 0.16 \cdot W_{Saddle}^{Tare}$ $= 38 + 0.42 \cdot W_{Cargo} + 4.3$ $= 42.3 + 0.42 \cdot W_{Cargo}$
Rear tridem axle - Semi-trailer	$= W_3^{Tare} + 0.50 \cdot W_{Cargo}$ $= 55 + 0.50 \cdot W_{Cargo}$

Lowbed Trailer

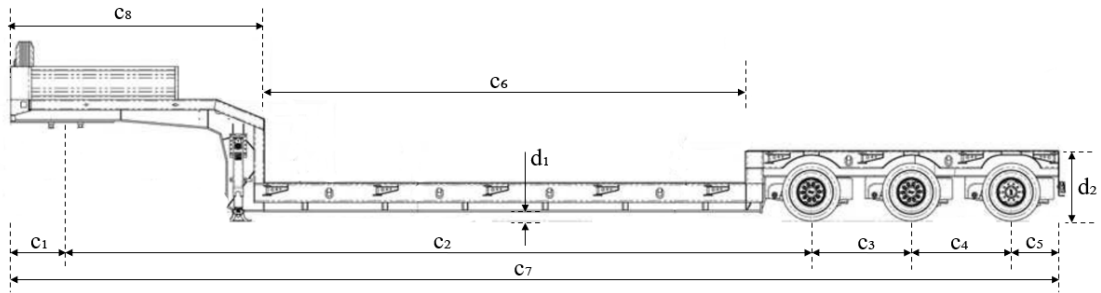
Lowbed trailers are designed with low deck height, allowing it to haul large and heavy cargos such as bulldozers, excavators, as well as other heavy and oversized cargo that requires a low-profile trailer in transportation. Same as flatbed trailers, the lowbed trailers as well consist of two components articulated together, namely, front tractor and rear semi-trailer. A typical example of articulated lowbed trailer is presented in Figure 6.22



Source: MAX Trailer

Figure 6.22 A typical lowbed trailer

For the sake of simplicity, the same tractor of Volvo FH 16 used in flatbed trailer was considered in composing a lowbed trailer. Regarding the lowbed platform, an analysis was made based on a three-axle semi-trailer manufactured by RAC[®] Germany, as depicted in Figure 6.23. Based on its technical specifications, the semi-trailer's unladen weight was specified as 105 kN. It was assumed that one-third of the unladen vehicle weight would be supported by the saddle/fifth-wheel, while two-thirds would be distributed over the rear tridem axle group.



Source: Modified from RAC Germany

Figure 6.23 The drawing of lowbed semi-trailer

The dimensions of the selected semi-trailer as obtained from the manufacturer's specifications along with the unladen weight distributions are presented in Table 6.13.

Table 6.13 Dimensions and unladen axle weights of lowbed semi-trailer

Dimensions (m)									
c ₁	c ₂	c ₃	c ₄	c ₅	c ₆	c ₇	c ₈	d ₁	d ₂
0.75	9.94	1.36	1.36	0.66	6.56	14.07	3.46	0.12	0.95
Unladen weight distributions (kN)									
Saddle					Rear axle group				
35					70				

For lowbed trailers, the characteristics of the connections are similar to that of the lowbed trailer, and in turn the simplified equivalent static model. Accordingly, the same modeling methodology and corresponding calculation procedures used in the computations previously for the flatbed trailer were applied to determine the load distributions for the lowbed trailer. As a result, the axle loads of the analyzed lowbed trailer were derived and are presented in Table 6.14.

Table 6.14 Axle loads distribution of flatbed trailer (kN)

Front axle - Tractor	$= W_1^{Tare} + 0.08 \cdot W_{Cargo} + 0.86 \cdot W_{Saddle}^{Tare}$ $= 52 + 0.06 \cdot W_{Cargo} + 30.1$ $= 82.1 + 0.06 \cdot W_{Cargo}$
Rear tandem axle - Tractor	$= W_2^{Tare} + 0.41 \cdot W_{Cargo} + 0.14 \cdot W_{Saddle}^{Tare}$ $= 38 + 0.41 \cdot W_{Cargo} + 4.9$ $= 42.9 + 0.41 \cdot W_{Cargo}$
Rear tridem axle - Semi-trailer	$= W_3^{Tare} + 0.53 \cdot W_{Cargo}$ $= 70 + 0.53 \cdot W_{Cargo}$

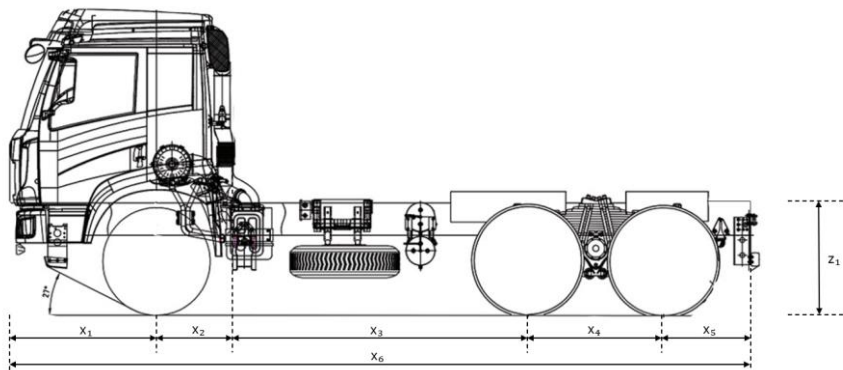
Dump Truck

The FAW® 6x4 15.5m³ dump truck, as depicted in Figure 6.24 and 6.25, was chosen for use in the development of wind and solar energy plants.



Source: FAW TRUCKS, Inc.

Figure 6.24 The FAW® 6x4 15.5m³ dump truck



Source: Modified from FAW TRUCKS, Inc.

Figure 6.25 Drawing of the dump truck

The dimensions and unladen axle weights of the dump truck were obtained by accessing the manufacturer's specifications and are listed in Table 6.15.

Table 6.15 Dimensions and unladen axle weights of dump truck

Dimensions (m)						
X ₁	X ₂	X ₃	X ₄	X ₅	X ₆	Z ₁
1.49	0.78	2.92	1.35	0.85	7.39	1.14
Unladen axle weight distributions (kN)						
Front axle			Rear tandem axle			
45			50			

The same modeling approach used for the flatbed trailer was employed to determine the cargo load distributions on individual axles of dump trucks. To accomplish this, a simplified beam structure (as shown in Figure 6.26) was taken into consideration. The variables \bar{W}_1 and \bar{W}_2 denote the loads distributed on the two axles from the carried cargo, W_{Cargo} . Meanwhile, it was assumed that the gravity center of the carried cargo is consistently located in the middle between the track-head end and the end of the tipper box.

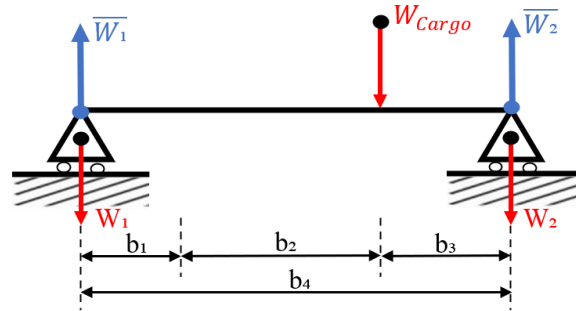


Figure 6.26 Computational model of dump truck

By writing the bending moment equilibrium equation around the center of front axle, the reactions from two axles could be defined.

$$\sum M_1 = 0, \bar{W}_2 \cdot b_4 - W_{Cargo} \cdot (b_1 + b_2) = 0 \quad 6.10$$

Where:

- M_1 is the moment calculated around the front axle, in $\text{kN} \cdot \text{m}$;
- \bar{W}_2 is the reaction of rear axle of the dump truck, in kN ;
- W_{Cargo} is the load of cargo, in kN ;
- b_1 is the distance from the center of the front axle to the end of the truck head, $=0.78 \text{ m}$;
- b_2 is the distance measured from the gravity center of cargo to the rear axle of dump truck, $=2.56 \text{ m}$;
- b_3 is the distance measured from the gravity center of cargo to end of tipper box, $=1.04 \text{ m}$;
- b_4 is the length measuring from the front axle to the rear axle, $=4.38 \text{ m}$.

Then,

$$\bar{W}_2 = W_{Cargo} \cdot \frac{b_1 + b_2}{b_4} \quad 6.11$$

$$\bar{W}_1 = W_{Cargo} - \bar{W}_2 \quad 6.12$$

Where:

- \bar{W}_1 is the reaction of front axle of the dump truck, in kN;

Finally, the axle loads of the analyzed dump truck were determined by adding the unladen weight of each axle to the load distributed from the cargo. The resulting values are listed in Table 6.16.

Table 6.16 Axle loads distribution of dump truck (kN)

Front axle	$= W_1^{Tare} + 0.41 \cdot W_{Cargo}$ $= 45 + 0.24 \cdot W_{Cargo}$
Rear tandem axle	$= W_2^{Tare} + 0.59 \cdot W_{Cargo}$ $= 50 + 0.76 \cdot W_{Cargo}$

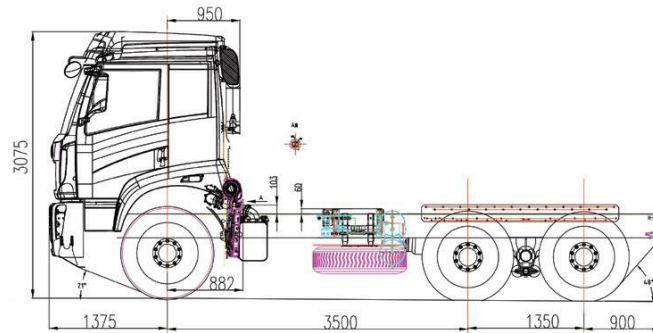
Concrete Mixer

The concrete mixer considered in this study was a 6 m³ mixer manufactured by FAW TRUCKS®, a visual representation and a technical drawing along with the dimensions of the mixer can be found in Figure 6.27 and 6.28, respectively. In accordance with the specifications from the manufacture, an unladen front axle load of 44 kN and an unladen rear tandem axle load of 73 kN were recorded.



Source: FAW TRUCKS, Inc.

Figure 6.27 FAW® 6m3 concrete mixer



Source: FAW TRUCKS, Inc.

Figure 6.28 Drawing of the concrete mixer

By following the same modeling and calculation approach previously presented for the dump truck, the axle loads for the analyzed concrete mixer were determined and are presented in Table 6.17.

Table 6.17 Axle loads distribution of concrete mixer (kN)

Front axle	$= W_1^{Tare} + 0.20 \cdot W_{Cargo}$ $= 44 + 0.20 \cdot W_{Cargo}$
Rear tandem axle	$= W_2^{Tare} + 0.80 \cdot W_{Cargo}$ $= 73 + 0.80 \cdot W_{Cargo}$

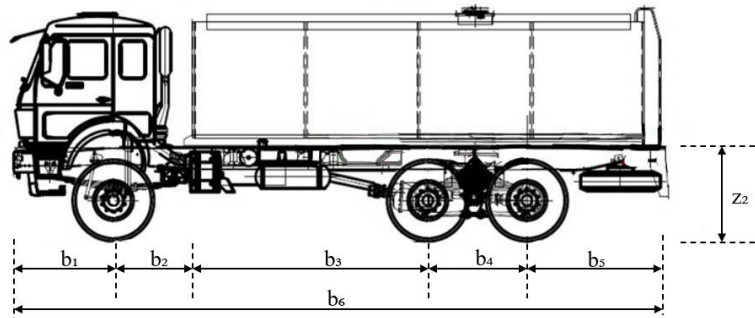
Water Tanker

The transportation of portable and non-portable water to construction sites was anticipated by the use of water tankers and a typical example is depicted in Figure 6.29. For the sake of simplicity, the same type of water tanker was considered for both portable and non-portable water transportation. Specifically, a BEIBEN 20 kL water tanker, as depicted in Figure 6.30 of a drawing of which, was chosen in the current study.



Source: Hydra Solutions Enterprise

Figure 6.29 A typical water tanker



Source: Modified from BEIBEN TRUCKS

Figure 6.30 BEIBEN 20 kL water tanker

In accordance with the specifications from the corresponding manufacture, an unladen front axle load of 35 kN and an unladen rear tandem axle load of 45 kN were obtained for the BEIBEN 20 kL water tanker. These values, along with the detailed dimensions of the water tanker collected from the specifications, are presented in Table 6.18.

Table 6.18 Dimensions and unladen axle weights of water tanker

Dimensions (m)						
b ₁	b ₂	b ₃	b ₄	b ₅	b ₆	z ₂
1.41	1.07	3.38	1.40	2.18	9.44	1.99
Unladen axle weight distributions (kN)						
Front axle			Rear tandem axle			
35			45			

Similar to the dump truck analyzed, the water tanker was evaluated using the same modeling and calculation approach to determine the axle load distributions. The resulting axle loads for the analyzed water tanker are presented in Table 19.

Table 6.19 Axle loads distribution of water tanker (kN)

Front axle	$= W_1^{Tare} + 0.11 \cdot W_{Cargo}$ $= 35 + 0.11 \cdot W_{Cargo}$
Rear tandem axle	$= W_2^{Tare} + 0.89 \cdot W_{Cargo}$ $= 45 + 0.89 \cdot W_{Cargo}$

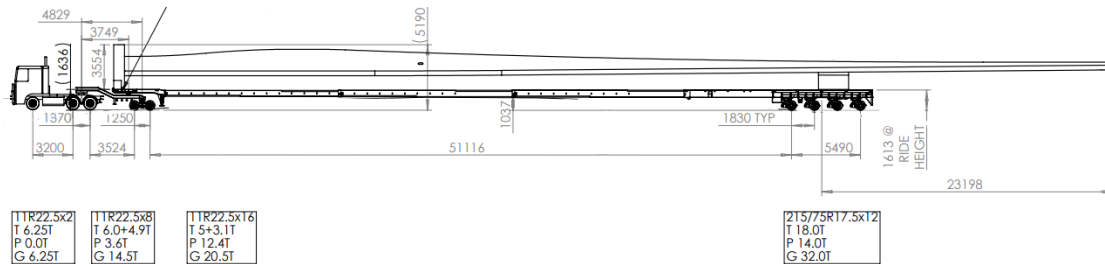
6.3.1.2 Specialized Hauling Units

Considering the superheavy nature and abnormal dimensions of the wind turbine components, some specialized hauling units were anticipated to be employed in each movement of the turbine components. For the sake of simplicity, the readily available analysis of transport of wind turbine equipment made for the development of Rye Park wind farm was adopted in the present study (Tilt

Renewables Australia Pty Ltd, 2022). In the following, 4 different types of specialized hauling units alongside the axle load distributions will be introduced.

Tractor with 2x8 dolly, 4x4 Steerable extendable

To accommodate the movement of blades, due to the nature of its abnormal length and height, a specialized hauling unit consists of a tractor, a 2x8 dolly and a 4x4 Steerable extendable was considered as shown in Figure 6.31.



Source: Modified from Tilt Renewables Australia Pty Ltd (2022)

Figure 6.31 Hauling unit for blades

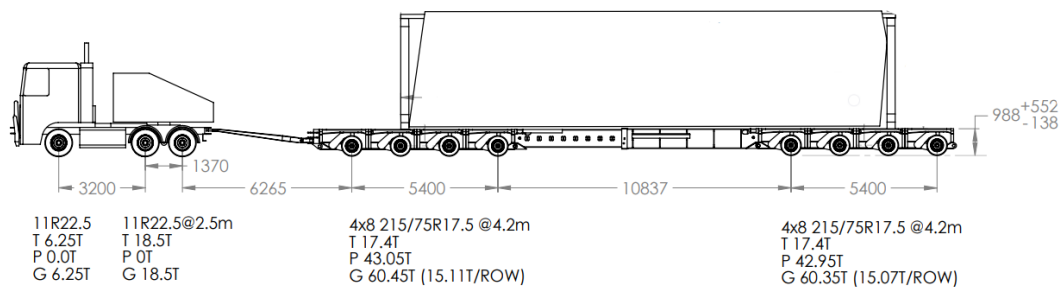
According to the distributions of tare vehicle weight and cargo weight to each axle or axle group as depicted in Figure 6.31, the axle load distributions of blade hauling vehicle in a general form to variable weight of blades in question can be derived as presented in Table 6.20 with the assumption made of the consistent placement of gravity center to different blades on the hauling vehicle.

Table 6.20 Axle loads distribution of blade hauling unit (kN)

Front axle	= 62.5
Tractor tandem axle	= 109 + 0.12 · W_{Cargo}
Dolly tandem axle	= 81 + 0.41 · W_{Cargo}
Rear quad-axle	= 180 + 0.47 · W_{Cargo}

Tractor with 4x8-4x8 extending platform trailer

The hauling vehicle for the movements of wind components such as nacelle, base tower sections, considering the comparatively lower magnitude of weight and length compared to middle tower sections, was selected as a tractor with 4x8-4x8 extending platform trailer (Figure 6.32).



Source: Modified from Tilt Renewables Australia Pty Ltd (2022)

Figure 6.32 Hauling unit for nacelle and base tower sections

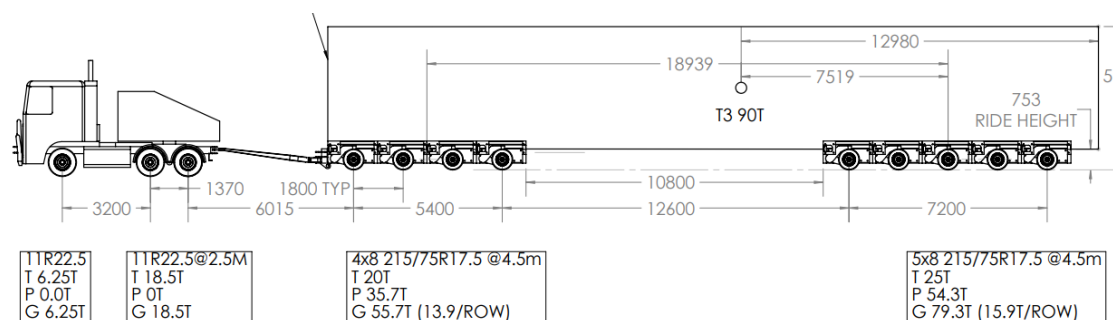
The resulting load distributions to each axle (group) were calculated based on the transport analysis of a nacelle in the development of Ray Park wind farm and are shown in Table 6.21.

Table 6.21 Axle loads distribution of nacelles and base tower sections hauling unit (kN)

Front axle	= 62.5
Tractor tandem axle	= 185
Middle quad-axle	= $174 + 0.5 \cdot W_{Cargo}$
Rear quad-axle	= $174 + 0.5 \cdot W_{Cargo}$

Tractor with 4x8-5x8 Low extending platform trailer

For the transport of the heaviest tower sections, a 5x8 platform modulus was expected to be necessary in distributing the higher magnitude of payload. Similar to the hauling unit employed in transporting the nacelles and base tower sections, a specialized vehicle composing a tractor with 4x8-5x8 Low extending platform trailer (Figure 6.33) was used in such a case.



Source: Modified from Tilt Renewables Australia Pty Ltd (2022)

Figure 6.33 Hauling unit for heavier tower sections

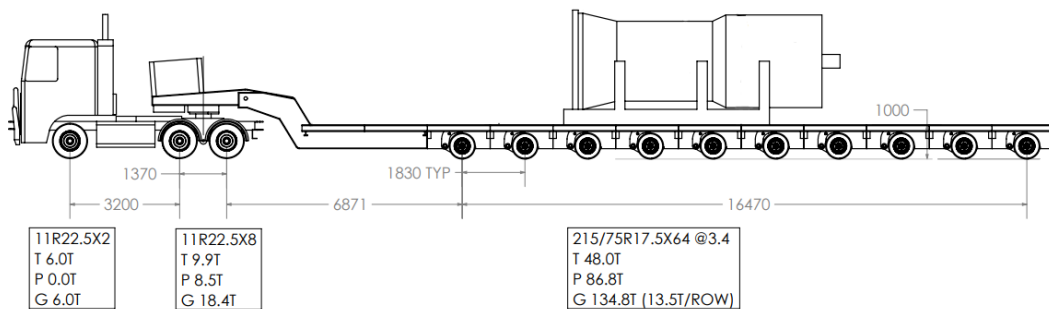
Based on the existing data as can be seen in Figure 6.33, the load distributions to each axle (group) of the considered hauling vehicle can be easily defined, with the results shown in Table 6.22.

Table 6.22 Axle loads distribution of heavier tower sections hauling unit (kN)

Front axle	= 62.5
Tractor tandem axle	= 185
Middle quad-axle	= $200 + 0.40 \cdot W_{Cargo}$
Rear five-axle group	= $250 + 0.60 \cdot W_{Cargo}$

Tractor with 10x8 Platform trailer

In the movements of transformers, driver trains and hubs, a hauling vehicle consisting of a tractor and a 10x8 platform trailer was considered in this study. Figure 6.34 depicted the configuration of the vehicle, alongside with the corresponding data of load distributions for the movement of a 95.3 tonnes drive train.



Source: Modified from Tilt Renewables Australia Pty Ltd (2022)

Figure 6.34 Hauling unit for transformers, driver trains and hubs

Based on the readily available data as shown in Figure 6.34, the load distributions of the considered vehicle can be easily defined, with the results shown in Table 6.23. It is noted that the load distributed to the front single axle was considered negligible in comparing the payload due to its specialized configuration of the vehicle.

Table 6.23 Axle loads distribution of transformers hauling unit (kN)

Front axle	= 60
Tractor tandem axle	= $99 + 0.09 \cdot W_{Cargo}$
Rear ten-axle group	= $480 + 0.91 \cdot W_{Cargo}$

6.3.2 Estimates of ESALs

In this subsection, the axle loads of each type of considered vehicles employed in the assumed development of wind and solar energy plants in this study will be calculated in accordance with the axle load distribution factors as calculated previously. The fourth power law and the associated parameters as described in the Annex will be used to estimate EALF to a standard 80 kN single-axle, and subsequently, the calculation of the ESALs with the estimated passages of each type of vehicles would be carried out.

It is noted that the superimposing effects of stresses and strains induced by the quad-axle, five-axle, and ten-axle groups in the pavement layers were assumed negligible due to the wide spacing of axles (1.8 m). Hence, those axle groups were considered as multiple single axles in the calculations of EALF. The passenger cars and light vehicles were not included in the calculation process since it is believed that these vehicles with lower mass and can therefore be neglected in the structural design process.

6.3.2.1 Wind Plant

In the following, the ESALs were calculated accordingly for each type of employed vehicles within two major categories, namely, heavy vehicles and OW/OS vehicles.

Heavy vehicles associated ESALs

The heavy vehicles are typically used to delivery construction material, civil works plant, and other associated miscellaneous equipment throughout the life span of a wind farm. In the present study of traffic spectrum analysis of a wind farm, the heavy vehicles include dump trucks, water trucks, flatbed trailers and lowbed trailers.

Water tanker trucks and dump trucks:

The ESALs associated with the movements of dump trucks and water trucks were calculated for various payloads according to the cargo to be carried on. Additionally, the ESALs for the passes of empty trucks leaving the development site were also estimated. In consequence, as presented in Table 6.24 and 8.25, for the 45516 one-way passes of water trucks and dump trucks estimated in Section 6.1 were normalized into 656050 and 5074 ESALs under fully loaded and empty travelling conditions, respectively.

Table 6.24 ESALs of fully loaded dump trucks and water trucks

Dump Truck							
Purposes	Payload per vehicle (kN)	Axle loads per vehicle (kN)		EALF per vehicle		One-way loaded traffic	ESALs
		Front single axle	Rear tandem axle	Front single axle	Rear tandem axle		
Gravel and crushed stones; Sand; Steel debris; Concrete debris.	300	117	278	4.57	12.76	31834	551818
Cement; Aggregate; Excavation debris; Seeding soil;	225	99	221	2.35	5.10	12420	92418
Water truck							
Portable water	200	57	223	0.26	5.28	156	865
Non-portable water	200	57	223	0.26	5.28	1187	6577
Total estimated ESALs							651678

Table 6.25 ESALs of empty dump trucks and water trucks

Dump Truck					
Axle loads per vehicle (kN)		EALF per vehicle		One-way empty traffic	ESALs
Front single axle	Rear tandem axle	Front single axle	Rear tandem axle		
45	50	0.10	0.01	44254	5022
Water truck					
35	45	0.04	0.01	1343	61
Total estimated ESALs					5074

Lowbed trailer:

The lowbed trailers were expected to be employed in hauling construction plants in the development of wind farms. By accessing the specifications of considered equipment from several manufactures, such as Wolfe Equipment, Manitowoc, Caterpillar, Sinotruk, the general weights of those equipment were obtained and are listed in Table 6.26.

Table 6.26 Weights of construction plant

Construction plant	Weight (kN)
Roller	300
Bulldozer	250
Trencher	250
Grader	250
Wheel loader	250
Excavator	300
60 t capacity Crane	360

Subsequently, the ESALs of empty and loaded lowbed trailers were estimated as 59 and 243 according to the weight of each plant anticipated in this study. The resulting values are presented in Table 6.27 and 6.28.

Table 6.27 ESALs of loaded lowbed trailers

Loaded lowbed trailer									
Purposes	Payload per vehicle (kN)	Axle loads per vehicle (kN)			EALF per vehicle			One-way loaded traffic	ESALs Total
		Front single axle	Middle tandem axle	Rear tridem axle	Front single axle	Middle tandem axle	Rear tridem axle		
Bulldozer, Trencher, Grader, Wheel loader	250	97	145	203	2.17	0.95	0.84	34	135
Roller, Excavator	300	100	166	229	2.45	1.62	1.37	14	76
60-t capacity crane	360	104	191	261	2.82	2.81	2.30	4	32
Total estimated ESALs									243

Table 6.28 ESALs of empty lowbed trailers

Lowbed trailer							
Axle loads per vehicle (kN)			EALF per vehicle			One-way loaded traffic	ESALs Total
Front single axle	Middle tandem axle	Rear tridem axle	Front single axle	Middle tandem axle	Rear tridem axle		
82	43	70	1.11	0.01	0.01	52	59

Flatbed trailer:

The 812 passes of one-way flatbed trailer traffic estimated through the traffic analysis in Section 6.1 were used in the computation of ESALs. By linking the weights of different cargos transported on flatbed trailers, the corresponding total ESALs were approximated to be 6396 and 627 for loaded and empty flatbed trailers, as demonstrated in Tables 6.29 and 6.30.

Table 6.29 ESALs of loaded flatbed trailers

Loaded flatbed trailer									
Purposes	Payload per vehicle (kN)	Axle loads per vehicle (kN)			EALF per vehicle			One-way loaded traffic	ESALs Total
		Front single axle	Middle tandem axle	Rear tridem axle	Front single axle	Middle tandem axle	Rear tridem axle		
Miscellaneous equipment, disassembled crawler crane, portacabin, electricity reticulation cables, control cable, high voltage transmission line, transmission tower, steel work	300	99	168	205	2.32	1.71	0.88	274	1345
Crane counterweight, disassembled wind turbine, disassembled transformer	400	107	210	255	3.16	4.18	2.10	534	5044
Powerline poles	140	86	101	125	1.33	0.22	0.12	4	7
Total estimated ESALs									6396

Table 6.30 ESALs of empty flatbed trailers

Empty flatbed trailer							
Axle loads per vehicle (kN)			EALF per vehicle			One-way loaded traffic	ESALs Total
Front single axle	Middle tandem axle	Rear tridem axle	Front single axle	Middle tandem axle	Rear tridem axle		
75	42	55	0.76	0.01	0.005	812	627

Finally, the ESALs generated by each heavy vehicle type examined in the previous calculations were summarized, resulting in 658316 and 5768 ESALs for 46461 one-way passages of heavy vehicles under loading and unloading states, respectively.

OW/OS vehicles associated ESALs

The transportation of wind turbine components and heavy equipment like transformers and cranes necessitates the use of OW/OS hauling units. These vehicles are typically customized with multi-axle groups to effectively distribute the abnormal payloads and/or to accommodate the movement of oversized components such as blades. The ESALs for each OW/OS vehicle considered in this study were computed based on load distribution factors derived in Section

6.3.1.2 and the weights of the cargos to be transported. The resulting ESALs for each type of OW/OS vehicle, both in loaded and empty states, are presented in Tables 6.31 to 6.34.

Table 6.31 ESALs of Tractor with 2x8 dolly, 4x4 Steerable extendable

Tractor with 2x8 dolly, 4x4 Steerable extendable											
Purposes	Payload per vehicle (kN)	Axle loads per vehicle (kN)				EALF per vehicle				One-way traffic	ESALs Total
		Front single axle	Tractor tandem axle	Dolly tandem axle	Rear quad-axle	Front single axle	Tractor tandem axle	Dolly tandem axle	Rear quad-axle		
Blades	280	63	143	196	312	0.37	0.88	0.56	3.60	90	487
Empty	0	63	109	81	180	0.37	0.30	0.02	0.40	90	98

Table 6.32 ESALs of Tractor with 4x8-4x8 extending platform trailer

Tractor with 4x8-4x8 extending platform trailer											
Purposes	Payload per vehicle (kN)	Axle loads per vehicle (kN)				EALF per vehicle				One-way traffic	ESALs Total
		Front single axle	Tractor tandem axle	Middle quad-axle	Rear quad-axle	Front single axle	Tractor tandem axle	Middle quad-axle	Rear quad-axle		
Nacelle	860	63	185	604	604	0.37	2.50	50.77	50.77	30	3132
Base section No.1	860	63	185	604	604	0.37	2.50	50.77	50.77	30	3132
Base section No.2	850	63	185	599	599	0.37	2.50	49.11	49.11	30	3033
Top section No.1	760	63	185	554	554	0.37	2.50	35.93	35.93	30	2242
Top section No.2	640	63	185	494	494	0.37	2.50	22.72	22.72	30	1449
Empty	0	63	185	174	174	0.37	2.50	0.35	0.35	150	536

Table 6.33 ESALs of Tractor with 4x8-5x8 low extending platform trailer

Tractor with 4x8-5x8 low extending platform trailer											
Purposes	Payload per vehicle (kN)	Axle loads per vehicle (kN)				EALF per vehicle				One-way traffic	ESALs Total
		Front single axle	Tractor tandem axle	Middle quad-axle	Rear five-axle	Front single axle	Tractor tandem axle	Middle quad-axle	Rear five-axle		
Middle section	900	63	185	560	790	0.37	2.50	37.52	76.07	30	3494
Empty	0	63	185	200	250	0.37	2.50	0.61	0.76	30	127

Table 6.34 ESALs of Tractor with 10x8 platform trailer

Tractor with 10x8 platform trailer									
Purposes	Payload per vehicle (kN)	Axle loads per vehicle (kN)			EALF per vehicle			One-way traffic	ESALs Total
		Front single axle	Tractor tandem axle	Rear ten-axle	Front single axle	Tractor tandem axle	Rear ten-axle		
Transformer	800	60	171	1208	0.32	1.83	51.99	1	54
120-t capacity crane	600	60	153	1026	0.32	1.17	27.05	14	400
Driver train	953	60	185	1347	0.32	2.49	80.43	30	2497
Hub	621	60	155	1045	0.32	1.23	29.13	30	920
Empty	0	60	99	480	0.32	0.21	1.30	75	136

Upon aggregating the individual ESALs linked with each OW/OS hauling vehicle type, a total of 20841 and 898 ESALs were approximated for the expected 345 one-way OW/OS vehicle traffic movements in loaded and empty conditions, correspondingly.

It is noteworthy that the wind turbine type selected to be installed in wind farms varies depending on various factors such as wind speed, geological and topographical conditions at the site, etc. Moreover, it was observed that the ESALs generated by the movement of wind turbine components were more significant compared to those generated by the site preparation and/or construction associated activities, given the same number of vehicle movements. To obtain a comprehensive assessment of the ESALs associated with the movement of wind components during the development of wind farms, two different types of wind turbines were selected from a study conducted by Jolanda Prozzi et al. in 2011 and a wind energy project in Australia (NSW, 2021). The magnitude of the wind components for each of the considered wind turbines is presented in Tables 6.35 and 6.36, respectively.

Table 6.35 Siemens 2.3 MW Unit

Wind Components	Weight (kN)
Hub	286
Nacelle (with drive train)	875
Tower-Base section	604
Tower-Middle section	599
Tower-Top section	496
Blade	123

Source: Jolanda Prozzi (2011)

Table 6.36 Bowmans Creek Wind Farm (6.2 MW Unit)

Wind Components	Weight (kN)
Hub	150
Nacelle	800
Blade	100
Drive Train	800
Tower-Base section	500
Tower-Middle section No.1	500
Tower-Middle section No.2	500
Tower-Top section	500

Source: NSW (2021)

The ESALs associated with the movement of each of the considered wind components were computed for two different types of wind turbines using the same methodology and steps as previously presented. The resulting ESALs are presented in Tables 6.37 to 6.42 below.

Table 6.37 ESALs calculation - Siemens 2.3 MW Unit (1)

Tractor with 2x8 dolly, 4x4 Steerable extendable											
Purposes	Payload per vehicle (kN)	Axle loads per vehicle (kN)				EALF per vehicle				One-way traffic	ESALs Total
		Front single axle	Tractor tandem axle	Dolly tandem axle	Rear quad-axle	Front single axle	Tractor tandem axle	Dolly tandem axle	Rear quad-axle		
Blades	123	63	124	131	238	0.37	0.50	0.11	1.22	90	199
Empty	0	63	109	81	180	0.37	0.30	0.02	0.40	90	98

Table 6.38 ESALs calculation - Siemens 2.3 MW Unit (2)

Tractor with 4x8-4x8 extending platform trailer											
Purposes	Payload per vehicle (kN)	Axle loads per vehicle (kN)				EALF per vehicle				One-way traffic	ESALs Total
		Front single axle	Tractor tandem axle	Middle quad-axle	Rear quad-axle	Front single axle	Tractor tandem axle	Middle quad-axle	Rear quad-axle		
Base section	604	63	185	476	476	0.37	2.50	19.58	19.58	30	1261
Middle section	599	63	185	474	474	0.37	2.50	19.18	19.18	30	1237
Top section	496	63	185	422	422	0.37	2.50	12.10	12.10	30	812
Empty	0	63	185	174	174	0.37	2.50	0.35	0.35	90	322

Table 6.39 ESALs calculation - Siemens 2.3 MW Unit (3)

Tractor with 10x8 platform trailer									
Purposes	Payload per vehicle (kN)	Axle loads per vehicle (kN)			EALF per vehicle			One-way traffic	ESALs Total
		Front single axle	Tractor tandem axle	Rear ten-axle	Front single axle	Tractor tandem axle	Rear ten-axle		
Nacelle (with driver train)	875	60	178	1276	0.32	2.13	64.77	30	2017
Hub	286	60	125	740	0.32	0.52	7.33	30	245
Empty	0	60	99	480	0.32	0.21	1.30	60	109

Table 6.40 ESALs calculation - Bowmans Creek Wind Farm (1)

Tractor with 2x8 dolly, 4x4 Steerable extendable											
Purposes	Payload per vehicle (kN)	Axle loads per vehicle (kN)				EALF per vehicle				One-way traffic	ESALs Total
		Front single axle	Tractor tandem axle	Dolly tandem axle	Rear quad-axle	Front single axle	Tractor tandem axle	Dolly tandem axle	Rear quad-axle		
Blades	100	63	121	122	227	0.37	0.46	0.08	1.01	90	174
Empty	0	63	109	81	180	0.37	0.30	0.02	0.40	90	98

Table 6.41 ESALs calculation - Bowmans Creek Wind Farm (2)

Tractor with 4x8-4x8 extending platform trailer											
Purposes	Payload per vehicle (kN)	Axle loads per vehicle (kN)				EALF per vehicle				One-way traffic	ESALs Total
		Front single axle	Tractor tandem axle	Middle quad-axle	Rear quad-axle	Front single axle	Tractor tandem axle	Middle quad-axle	Rear quad-axle		
Nacelle	800	63	185	574	574	0.37	2.50	41.41	41.41	30	2571
Base section	500	63	185	424	424	0.37	2.50	12.33	12.33	30	826
Middle section No.1	500	63	185	424	424	0.37	2.50	12.33	12.33	30	826
Middle section No.2	500	63	185	424	424	0.37	2.50	12.33	12.33	30	826
Top section	500	63	185	424	424	0.37	2.50	12.33	12.33	30	826
Empty	0	63	185	174	174	0.37	2.50	0.35	0.35	150	536

Table 6.42 ESALs calculation - Bowmans Creek Wind Farm (3)

Tractor with 10x8 platform trailer									
Purposes	Payload per vehicle (kN)	Axle loads per vehicle (kN)			EALF per vehicle			One-way traffic	ESALs Total
		Front single axle	Tractor tandem axle	Rear ten-axle	Front single axle	Tractor tandem axle	Rear ten-axle		
Driver train	800	60	171	1208	0.32	1.83	51.99	30	1624
Hub	150	60	113	617	0.32	0.34	3.53	30	126
Empty	0	60	99	480	0.32	0.21	1.30	60	109

By examining the ESALs generated by the movements of OW/OS vehicles during the transportation of wind components for each of the three types of wind turbines, a comparative analysis was performed to determine the expected total ESALs resulting from the movements of 30 wind turbines, as demonstrated in Table 6.43. The results revealed that the ESALs associated with the movements of wind turbine components were influenced by the total weight of the wind turbine and the installation configuration of the wind turbine, such as the number of sections composing a wind tower.

Table 6.43 ESALs comparison of three types of wind turbine

Wind components associated ESALs - Comparison				
		Vestas V162-6.2 MW (729 t)	Siemens 2.3 MW Unit (323 t)	Bowmans Creek Wind Farm (6.2 MW Unit) (405 t)
One-way traffic		330	240	300
Total ESALs	Loaded	20390	5770	7798
	Empty	871	529	743

Remarks

In the course of estimating the ESALs for heavy and OW/OS vehicles anticipated in the development of a wind farm consisting of 30 Vestas V162-6.2 MW wind turbines installed over a 25-year life span. An estimated one-way traffic flow of 46725 heavy and OW/OS vehicles was then converted into ESALs. For loading conditions of these vehicles, 679157 ESALs were estimated, while for empty travelling conditions, 6666 ESALs were predicted.

6.3.2.2 Solar Plant

Similar to the ESALs calculations for wind farm development, the ESALs associated with an assumed solar farm development, as described in Section 6.2, were computed for each type of vehicles in two main categories (i.e., heavy vehicles and OW/OS vehicles). Employing the identical assumptions and estimation methodologies utilized earlier in the ESALs calculations for wind

farm, the corresponding ESALs for the transportation of heavy and OW/OS vehicles were estimated and are presented in the subsequent sections.

Heavy vehicles associated ESALs

The development of a solar farm required the use of various heavy vehicles, including dump trucks, concrete mixers, water trucks, flatbed trailers, and lowbed trailers. Assuming the use of the same types of dump trucks, water trucks, flatbed trailers, and lowbed trailers as employed in wind farm development, and incorporating the configuration and load distribution factors of concrete mixer as presented and defined in Section 6.3.1.1, for the one-way heavy traffic of 23359 vehicles as calculated previously, the aggregated ESALs linked to the trips made by the heavy vehicles in unladen and loaded travelling conditions were estimated to be 3888 and 301777, respectively. The breakdown of ESALs for each vehicle type is presented below through Tables 6.44 to 6.49.

Table 6.44 ESALs of loaded dump trucks, water trucks and concrete mixers

Dump Truck							
Purpose	Payload per vehicle (kN)	Axle loads per vehicle (kN)		EALF per vehicle		One-way loaded traffic	ESALs Total
		Front single axle	Rear tandem axle	Front single axle	Rear tandem axle		
Gravel and crushed stones; Sand; Steel debris; Concrete Debris	300	117	278	4.57	12.76	14951	259165
Excavation debris	225	99	221	2.35	5.10	2016	15002
Water tanker							
Portable water	200	57	223	0.26	5.28	138	765
Non-portable water	200	57	223	0.26	5.28	1824	10106
Concrete mixer							
Concrete mixture	145	73	189	0.69	2.73	2515	8600

Table 6.45 ESALs of empty dump trucks, water trucks and concrete mixers

Empty Dump Truck					
Axle loads per vehicle (kN)		EALF per vehicle		One-way loaded traffic	ESALs Total
Front single axle	Rear tandem axle	Front single axle	Rear tandem axle		
45	50	0.10	0.01	16967	1926
Empty Water tanker					
35	45	0.04	0.01	1962	90
Empty Concrete mixer					
44	73	0.09	0.06	2515	383

Table 6.46 ESALs of loaded lowbed trailers in solar farm

Loaded lowbed trailer									
Purposes	Payload per vehicle (kN)	Axle loads per vehicle (kN)			EALF per vehicle			One-way loaded traffic	ESALs Total
		Front single axle	Middle tandem axle	Rear tridem axle	Front single axle	Middle tandem axle	Rear tridem axle		
Bulldozer, Trencher, Grader, Wheel loader, Pilling rig	250	97	145	203	2.17	0.95	0.84	20	79
Roller, Excavator, Miscellaneous	300	100	166	229	2.45	1.62	1.37	10	54
60-t compacity crane	360	104	191	261	2.82	2.81	2.30	4	32
Total estimated ESALs									165

Table 6.47 ESALs of empty lowbed trailers in solar farm

Empty lowbed trailer								One-way loaded traffic	ESALs Total
Axle loads per vehicle (kN)			EALF per vehicle						
Front single axle	Middle tandem axle	Rear tridem axle	Front single axle	Middle tandem axle	Rear tridem axle				
82	43	70	1.11	0.01	0.01	34		38	

Table 6.48 ESALs of loaded flatbed trailers in solar farm

Flatbed trailer									
Purposes	Payload per vehicle (kN)	Axle loads per vehicle (kN)			EALF per vehicle			One-way loaded traffic	ESALs Total
		Front single axle	Middle tandem axle	Rear tridem axle	Front single axle	Middle tandem axle	Rear tridem axle		
Miscellaneous equipment, portacabin, electricity reticulation cables, high voltage transmission line, transmission tower, steel work, wire fence	300	99	168	205	2.32	1.71	0.88	206	1011
Disassembled transformer, Tracker frame	400	107	210	255	3.16	4.18	2.10	448	4232
Solar panel	190	90	122	150	1.59	0.47	0.25	1076	2498
Power conversion unit	100	83	84	105	1.14	0.11	0.06	76	100
Battery Energy Storage Container	150	87	105	130	1.38	0.26	0.14	75	134
Total estimated ESALs									7974

Table 6.49 ESALs of empty flatbed trailers in solar farm

Empty flatbed trailer							
Axle loads per vehicle (kN)			EALF per vehicle			One-way loaded traffic	ESALs Total
Front single axle	Middle tandem axle	Rear tridem axle	Front single axle	Middle tandem axle	Rear tridem axle		
75	42	55	0.76	0.01	0.005	1881	1451

OW/OS vehicles associated ESALs

The use of OW/OS hauling units in the development of solar farms was limited as identified across the traffic analysis in Section 6.2. It was expected that only the movements of transformer and heavy cranes necessitated the use of platform trailers. The ESALs of 5 and 111 resulted from three one-way travels of such a specialized vehicle in unladen and loaded conditions were calculated respectively and are presented in Table 6.50 and 6.51.

Table 6.50 ESALs of loaded 10x8 platform trailers

Tractor with 10x8 platform trailer (Loaded)									
Purposes	Payload per vehicle (kN)	Axle loads per vehicle (kN)			EALF per vehicle			One-way loaded traffic	ESALs Total
		Front single axle	Tractor tandem axle	Rear ten-axle	Front single axle	Tractor tandem axle	Rear ten-axle		
Transformer	800	60	171	1208	0.32	1.83	51.99	1	54
120-t capacity crane	600	60	153	1026	0.32	1.17	27.05	2	57
Total estimated ESALs									111

Table 6.51 ESALs of unladen 10x8 platform trailers

Tractor with 10x8 platform trailer (Empty)							
Axle loads per vehicle (kN)			EALF per vehicle			One-way loaded traffic	ESALs Total
Front single axle	Tractor tandem axle	Rear ten-axle	Front single axle	Tractor tandem axle	Rear ten-axle		
60	99	480	0.32	0.21	1.30	3	5

Remarks

In the course of estimating the ESALs for heavy and OW/OS vehicles anticipated in the development of a solar farm over a 30-year of life span. An estimated one-way traffic volume of 23359 heavy and OW/OS vehicles was then

converted into ESALs, for loaded conditions, 301888 ESALs were estimated, while for empty travelling conditions, 3893 ESALs were predicted.

6.4 Summary

Throughout this chapter, the traffic spectra for proposed wind and solar developments were estimated. The derived results revealed that, for the same energy output capacity of 186 MW in wind and solar farms, the total vehicle passages in wind development were roughly 1.6 times greater than that of proposed solar development, amounting to 71676 and 43522, respectively. Moreover, the number of one-way trips made by heavy vehicles in the wind energy development of 46461 was double compared to that of the solar development of 23359, while the number of trips made by car/light vehicles was similar in both cases. Specifically, due to the characteristics of wind turbines movements in wind developments, 345 one-way trips of OW/OS vehicles were anticipated in the proposed wind farm development, whereas the use of such vehicles in the proposed solar farm development was limited to only 3 one-way trips.

Based on the estimated traffic information, for the trips generated solely by heavy and OW/OS vehicles, the total ESALs calculated to a standard 80 kN single axle were 679157 and 6666 for respective loaded and unloaded vehicles in the development of the proposed wind development. While for the proposed solar development, the ESALs were computed to be 301888 and 3893, respectively. The analysis demonstrated that ESALs calculated for empty vehicles were approximately 1% of that for loaded vehicles, for both wind and solar developments. Hence, it can be said that the impact of empty vehicles on estimates of ESALs is negligible when compared to that of loaded vehicles.

It is important to note that the aim of the study in this chapter was to provide a general assessment of the traffic spectra for wind and solar energy developments. To simplify the analysis, a readily available model and several available vehicle analyses to define the axle load distribution factors were used, vehicles information was collected from various manufactures. Several assumptions were made throughout the study in this chapter. However, if different vehicles or load distribution models were employed, it could potentially alter the results. Nonetheless, the trends presented in this study would still be applicable, even if the magnitude of the discrepancy changed.

Chapter 7

Pavements Design for Wind and Solar Plants

The following chapter focuses on the structural design of asphalt pavements for a proposed wind energy plant and a proposed solar energy plant, following a mechanistic-empirical pavement design approach. The structural distresses considered during the design process included fatigue cracking, rutting deformation, and load-induced shear failure. Empirical damage laws were employed to evaluate the extent of damage resulting from fatigue cracking and rutting at the end of the analysis periods. Meanwhile, for the load-induced shear failure in unbound layers, the designs followed the Russian standards for the design of flexible pavements (ODN 218.046-01). To ensure accurate structural designs in terms of fatigue and rutting, 12 analysis periods were utilized, with each period assigned to a specific month of the year. This approach was taken because it was observed from the analyses conducted in Chapter 3 that pavement designs based on fewer analysis periods, such as five or three, tended to neglect significant damages that occur during brief periods of high temperature and/or moisture content. This could potentially lead to unconservative designs, resulting in poor performance and early deterioration of pavements. On the other hand, the shear stability design was solely conducted in a specific analysis period which with the most critical environmental condition among the 12 analysis periods.

7.1 Description of Pavements Section and Layer Materials

A typical conventional flexible pavement cross section is depicted in Figure 7.1. The top layer, known as the surface course, provides direct support to traffic loads and is typically made of high-quality and relatively costly bituminous materials, while also preventing excessive surface water from penetrating the underlying

pavement layers. The binder course, which is constructed using larger aggregates and less bitumen compared to the surface course, provides the structural function of load distribution to the subgrade layer. The base course is usually made up of a granular mixture (e.g., crushed stone), stabilized mixtures, or asphalt mixture in modern heavy-duty asphalt pavements. The layer of material situated underneath the base course is called the subbase course. It is typically constructed with unbound granular mixture. The primary function of both the base and subbase courses is to distribute the applied loads, which helps to reduce the transmitted stress of the imposed load and ensure that the bearing capacity of the subgrade is not exceeded. In addition, the subbase course can offer a filter effect in the case of an unbound base course. A seal coat is a thin bitumen surface treatment used for providing waterproofing and/or skid resistance. A tack coat is a light application of bitumen, usually in the form of emulsion, to ensure bonding between bituminous layers. A prime coat is an emulsion or cutback bitumen applied to an untreated granular layer to ensure bonding between bituminous and granular layers and provide waterproofing effects. The subgrade, which uniformly supports the entire pavement, is the natural or imported soil that must be protected from applied traffic loads.

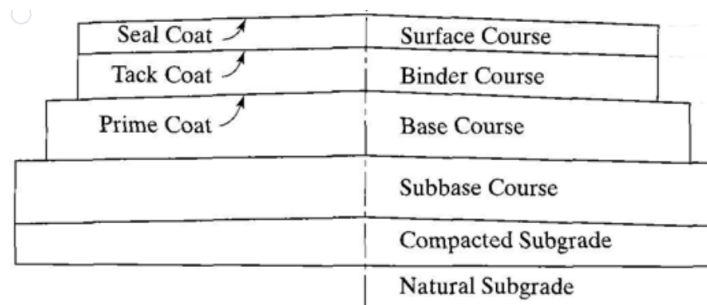


Figure 7.1 Typical conventional flexible pavement structure (Huang, 2004)

The asphalt pavement structure (see Fig. 7.2) anticipated in renewable energy plants in the current study involves a HMA surface course, a base layer that is expected to be built with unbound granular materials, and a homogeneous subgrade layer is assumed at the bottom of the pavement cross-section. The study does not consider any coating treatments as part of the analysis, as the boundary conditions between layers are assumed to be fully bound.

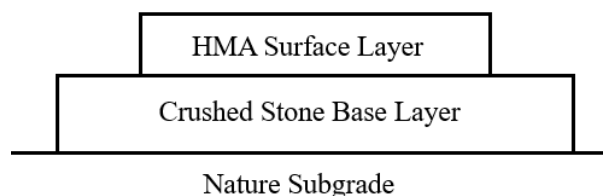


Figure 7.2 Pavement structure

For the purposes of pavement structural designs in the wind and solar farms, a pavement section was pre-defined as consisting of three layers. The surface layer was composed of HMA mixture with a binder performance grade of 70-22P, a mixture air void of 6.80%, and a volumetric binder content of 12%. The detailed descriptions of this type of HMA mixture can be found in Section 3.3.4. The unbound base layer was assumed to be constructed with crushed limestone, while the subgrade layer lying below the subbase layer comprises a type of high plastic clay soil as outlined in Section 3.3.1.

7.2 Description of Traffic Information

The traffic spectra associated with the proposed developments of a wind farm and a solar plant were thoroughly analyzed and presented in Chapter 6. The key traffic information related to the pavement structural designs in the considered wind and solar farm will be briefly presented as follows.

Solar farm

Throughout the analyses of traffic spectrum in the proposed solar farm with an energy output capacity of 186 MW. The total number of one-way vehicle passages was estimated to be 43522, including cars/light vehicles, heavy vehicles, and specialized superheavy vehicles. By homogenizing the various axle loads linked to 23362 passes of loaded heavy and superheavy vehicles into a reference 80 kN single axle, 301888 ESALs were estimated. The ESALs associated with the empty vehicles were found insignificant, accounting for only 1% compared to the ESALs of loaded vehicles, and therefore they were not considered in the design process. Similarly, passenger cars and light vehicles, due to their lower mass, were also considered negligible for the structural design process. Moreover, each of the 139 kN weighted single axle was found to be the heaviest axle load within a tandem axle group of a loaded dump truck in the development of the proposed solar plant. It was assumed that the load on the tandem axle was evenly supported by each of the two axles. Figure 7.3 illustrates the configuration of the heaviest axle based on the manufacturer's specifications.

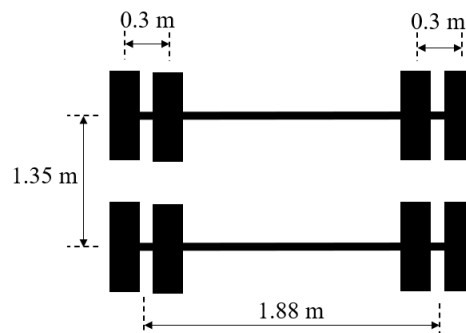


Figure 7.3 The heaviest axle configuration in solar farm

Wind farm

Regarding the traffic associated with a proposed 186 MW wind energy development, it was anticipated that 71676 vehicles would enter the site over the lifespan of the wind farm. Of these, 46461 vehicles were projected to be made by heavy and superheavy vehicles, while the remaining 25215 would be cars/light vehicles. The ESALs were calculated to be 679157 from the expected one-way heavy and superheavy vehicles, with the analysis excluding the travels of cars/light vehicles and empty vehicles for the same considerations made in traffic homogenizations for solar farm. The heaviest single axle load recorded was 158 kN, which was observed within a 790 kN five-axle group of a specialized hauling unit (consisting of a tractor with 4x8-5x8 low extending platform trailer) while transporting a 900 kN weighted middle tower section, assuming a uniform distribution of the load on the five-axle group to each composed axle. It is noted that even for the same type of superheavy load moving vehicle, a variety of axle and wheel spacings still exist (Fritz J. Jooste et al., 1995). Therefore, to provide a general assessment of such vehicles on pavement structural designs, some typical values of axle and wheel spacing were selected to construct the configuration of the observed heaviest axle (see Fig. 9.4) in the wind farm based on a study conducted by Fritz J. Jooste et al. in 1995. The study involved investigating a number of superheavy loads moves and load configurations.

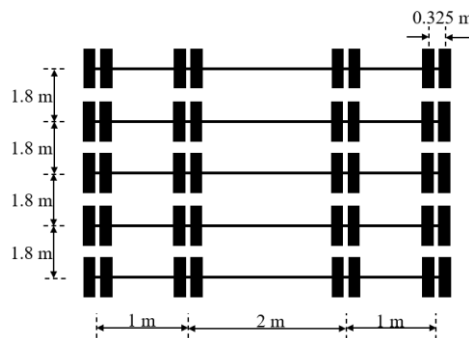
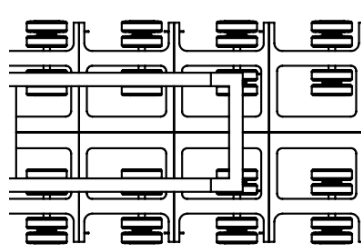


Figure 7.4 The heaviest axle load configuration in wind farm



Source: Tilt Renewables Australia Pty Ltd, 2022

Figure 7.5 Five-axle group (only 4 axles illustrated)

7.3 Pavement Design for Solar Farm

To structurally design an asphalt pavement in the proposed solar farm, the mechanical properties of each layer composing the pavement section were first defined according to the predefined thickness of each layer. Next, following the Russian pavement design guide, the shear stability in the unbound layers was designed in terms of the heaviest axle load expected from the traffic spectrum analysis. Last, the fatigue cracking in the asphalt layers and rutting deformation in the subgrade were verified by means of empirical damage laws and predicted equivalent single axle loads based on a mechanistic-empirical pavement design method.

7.3.1 Determinations of Layer Mechanical Properties

A pavement cross section was pre-defined with the following layer thicknesses:

- A HMA surface layer measuring 17-cm depth;
- An unbound granular base layer constructed with crushed limestone with a depth of 10 cm; and
- A homogeneous subgrade layer composed of high plastic clay (CH) soils.

By applying the same monthly climatic data (i.e., air temperature and precipitation) over a 10-year span as collected in Kaufman County, North Texas and presented in Section 3.3.3, and using identical models and the corresponding parameters as outlined in Chapter 3, the moduli of the layers corresponding to each analysis period were calculated. The resulting material properties are tabulated in Table 7.1. It was assumed that the Poisson's coefficients of the asphalt layers and subgrade layer were 0.35, while the unbound base layer had a Poisson's coefficient of 0.30.

Table 7.1 Mechanical properties in 12 analysis periods (MPa)

Analysis period	1	2	3	4	5	6	7	8	9	10	11	12
Surface course $ E^* $	11796	11133	8475	6588	4869	3442	2997	2832	4054	6196	8352	11247
Base course E_{MG}	193	191	187	187	181	176	174	174	177	181	188	192
Subgrade M_R	121	121	118	118	114	111	110	109	111	114	118	121

It is worth noting that the monthly average moisture contents calculated in the subgrade were all below the optimal moisture content, as presented in Section 3.3.2.2. However, to account for the significant impact of brief precipitation events on moisture content fluctuations, it is recommended to determine the values of cohesions and friction angles at moisture contents above the optimum

level for a conservative analysis. For the current study, the cohesion and angle of internal friction values for fat clayey soil and crushed limestone were selected at moisture conditions above the optimum level as outlined in Section 5.2. The selected values of cohesions and friction angles for subbase and subgrade layers are presented in Table 7.2.

Table 7.2 Cohesion and Friction Angle Values for base and subgrade Materials

Material type	Cohesion (MPa)	Friction angle (°)
Base- Crushed Limestone	0.0544	52
Subgrade- Fat Clayey soil	0.0434	0

Additionally, the typical material densities for asphalt layers, base layer were selected as per the Russian pavement design guide ODN 218.046-01. These densities are presented in Table 7.3.

Table 7.3 Physical Characteristics of Structural Layer Materials

Material Type	Density (kN/m ³)
Hot Mixed Asphalt	2.40E-05
Crushed Limestone	1.60E-05

7.3.2 Shear Stability Design

Upon comparing the determined mechanical properties of each pavement layer across 12 analysis periods as shown in Table 7.1, it was observed that the eighth analysis period was subjected to the most critical environmental condition. Therefore, the shear stability design was based on the mechanical properties of this particular analysis period.

The stress components in the computational multi-layer system structure under the heaviest axle load were computed at four critical depths and four distinct transversal positions, as described in Section 5.1.2. The evaluated response points and the acting semi-axle load configuration are presented in Figure 7.6.

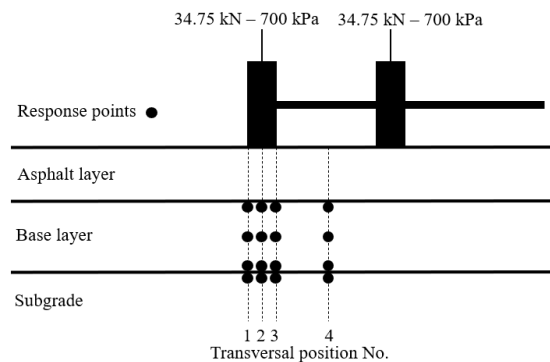


Figure 7.6 Evaluated response points within pavement

Subsequently, the numerical solutions of the structural response under loading at each of previously defined response points were obtained by using the ALVA analysis tool based on MATLAB[®] code. Following the uses of the Equations 7.1 and 7.2, as described in Section 5.1.1, the major and minor principal stresses were computed using the stress components previously derived at each analysis point.

The major principal stress:

$$\sigma_1 = \frac{\sigma_x + \sigma_z}{2} + \sqrt{\left(\frac{\sigma_z - \sigma_x}{2}\right)^2 + \tau_{xz}^2} \quad 7.1$$

The minor principal stress:

$$\sigma_3 = \frac{\sigma_x + \sigma_z}{2} - \sqrt{\left(\frac{\sigma_z - \sigma_x}{2}\right)^2 + \tau_{xz}^2} \quad 7.2$$

Where:

- σ_1 is major principal stress, in MPa;
- σ_3 is minor principal stress, in MPa;
- σ_x and σ_z are the stresses calculated in x and z direction in a cartesian coordinate system, respectively, in MPa; and
- τ_{xz} is tangential stress calculated in x-z direction, in MPa.

A calculation example is provided to the response point located at the bottom of base layer on the transversal position No.4.

Calculated stress components:

$$\sigma_x = -0.025 \text{ MPa}, \sigma_z = 0.090 \text{ MPa}, \tau_{xz} = 0.000 \text{ MPa}$$

Major principal stress:

$$\begin{aligned} \sigma_1 &= \frac{\sigma_x + \sigma_z}{2} + \sqrt{\left(\frac{\sigma_z - \sigma_x}{2}\right)^2 + \tau_{xz}^2} = \frac{-0.025 + 0.090}{2} + \sqrt{\left(\frac{0.090 - (-0.025)}{2}\right)^2 + 0} \\ &= 0.090 \text{ MPa} \end{aligned}$$

Minor principal stress:

$$\sigma_3 = \frac{\sigma_x + \sigma_z}{2} - \sqrt{\left(\frac{\sigma_z - \sigma_x}{2}\right)^2 + \tau_{xz}^2} = \frac{-0.025 + 0.090}{2} - \sqrt{\left(\frac{0.090 - (-0.025)}{2}\right)^2 + 0} = -0.025 \text{ MPa}$$

Finally, the maximum active shear stresses can be determined by substituting the derived major and minor principal stresses at each evaluation point, with the values of friction angles of subbase and subgrade as defined in Section 7.3.1 into the formulation 7.3, following the Russian pavement design guide as outlined in Section 7.1.1.

$$\tau_{max} = \frac{1}{2 \cdot \cos \varphi} [(\sigma_1 - \sigma_3) - (\sigma_1 + \sigma_3) \sin \varphi] \quad 7.3$$

Followed by the previous calculation example to the response point located at the bottom of base layer on the transversal position No.4, the maximum active shear stress can be derived as follows.

Maximum active shear stress:

$$\begin{aligned} \tau_{max} &= \frac{1}{2 \cdot \cos \varphi} [(\sigma_1 - \sigma_3) - (\sigma_1 + \sigma_3) \sin \varphi] \\ &= \frac{1}{2 \cdot \cos 52^\circ} [(0.090 \text{ MPa} - (-0.025 \text{ MPa})) - (0.090 \text{ MPa} + (-0.025 \text{ MPa})) \sin 52^\circ] \\ &= 0.052 \text{ MPa} \end{aligned}$$

The resulting stress components and calculated active shear stresses at each evaluation point were compiled and are presented in Table 7.4.

Table 7.4 Maximum active shear stresses results

Critical Depth	Transversal Position No.	Stress Components			Principal Stresses		Maximum Active Shear Stress (MPa)
		Sigma x (MPa)	Sigma z (MPa)	Sigma xz (MPa)	Sigma 1 (MPa)	Sigma 3 (MPa)	
Base_Top	1	0.006	0.088	-0.044	0.107	-0.013	0.037
	2	-0.007	0.127	-0.022	0.130	-0.011	<u>0.038</u>
	3	-0.001	0.126	-0.001	0.126	-0.001	0.023
	4	0.000	0.126	0.000	0.126	0.000	0.022
Base_Middle	1	-0.002	0.075	-0.033	0.087	-0.014	0.035
	2	-0.014	0.101	-0.018	0.104	-0.017	<u>0.042</u>
	3	-0.014	0.105	-0.002	0.106	-0.014	0.038
	4	-0.013	0.105	0.000	0.105	-0.013	0.038
Base_Bottom	1	-0.009	0.065	-0.023	0.072	-0.016	0.035
	2	-0.023	0.084	-0.014	0.086	-0.025	0.051

	3	-0.025	0.090	-0.002	0.090	-0.025	<u>0.052</u>
	4	-0.025	0.090	0.000	0.090	-0.025	<u>0.052</u>
Subgrade_Top	1	0.011	0.065	-0.023	0.074	0.003	0.035
	2	0.007	0.084	-0.014	0.086	0.005	<u>0.041</u>
	3	0.008	0.090	-0.002	0.090	0.007	<u>0.041</u>
	4	0.008	0.090	0.000	0.090	0.008	<u>0.041</u>

Table 7.4 presents the results of the maximum active shear stress under the heaviest axle load in the pavement of proposed solar farm development based on the Mohr–Coulomb yield criterion in the plane stress state given by Equation 7.3. The values that are underlined in the results correspond to the most critical horizontal location at each corresponding vertical depth in the pavement.

The allowable shear resistances in the base and subgrade layers were calculated according to the definition provided by the Russian structural pavement design guide (ODN 218.046-01), by the following relationship:

$$\tau_{all} = \frac{1}{F_{rel}} \cdot (c_c \cdot k + \sigma \cdot \tan\varphi_{st}) \quad 7.4$$

Where:

- τ_{all} is the allowable shear strength of the material composing the analyzed layer, in MPa;
- F_{rel} is a reliability parameter that depends on the importance of the pavement;
- c_c is the cohesion of the soils in the analyzed layer under critical environmental condition, in MPa;
- k is a parameter that depends on the boundary properties at the layer interface;
- When constructing with reinforced materials, as well as when inserting a separating geotextile layer at the boundary base-subgrade, the values can be taken as:
 - = 4,5, when used in a sandy layer of coarse sand;
 - = 4, when used in a sand layer of medium-size sand;
 - = 3, when used in a sandy layer of fine sand;
 - = 1, in all other cases.
- σ is the normal stress generated from the self-weight of the layers placing above the analyzed one, in MPa;
- φ_{st} is the design value of the angle of internal friction of the material of the analyzed layer under the static action of the load, expressed in °.

This study assumed a reliability factor and k parameter of 1.

The normal stress generated from the self-weight of the layers placing above the analyzed one can be calculated as:

$$\sigma = \gamma_{avg} \cdot H \quad 7.5$$

Where:

- γ_{avg} is the weighted average density of the structural layers located above the analyzed one, in kN/m^3 , $\gamma_{avg} = \frac{\sum \gamma_i \cdot H_i}{\sum H_i}$,
- H is the depth of the layer's surface being analyzed, measured from the top of the pavement structure, in m.

The allowable shear resistances in the base layer at three critical depths, and in the subgrade layer are determined as follows:

At the top of base layer:

$$\begin{aligned} \tau_{all1} &= \frac{1}{F_{rel}} \cdot (c_{c1} \cdot k + \sigma \cdot \tan \varphi_{st1}) \\ &= 0.054 \text{ MPa} + \frac{0.0024 \text{ kN/m}^3 \cdot 0.17 \text{ m}}{0.17 \text{ m}} * \tan 52^\circ \\ &= 0.060 \text{ MPa} \end{aligned}$$

At the middle of subbase layer:

$$\begin{aligned} \tau_{all2} &= \frac{1}{F_{rel}} \cdot (c_{c1} \cdot k + \sigma \cdot \tan \varphi_{st1}) \\ &= 0.054 \text{ MPa} + \frac{0.0024 \text{ kN/m}^3 \cdot 0.17 \text{ m} + 0.0016 \text{ kN/m}^3 \cdot 0.05 \text{ m}}{0.17 \text{ m} + 0.05 \text{ m}} * \tan 52^\circ \\ &= 0.061 \text{ MPa} \end{aligned}$$

At the base of subbase layer:

$$\begin{aligned} \tau_{all3} &= \frac{1}{F_{rel}} \cdot (c_{c1} \cdot k + \sigma \cdot \tan \varphi_{st1}) \\ &= 0.054 \text{ MPa} + \frac{0.0024 \text{ kN/m}^3 \cdot 0.17 \text{ m} + 0.0016 \text{ kN/m}^3 \cdot 0.10 \text{ m}}{0.17 \text{ m} + 0.10 \text{ m}} * \tan 52^\circ \\ &= 0.062 \text{ MPa} \end{aligned}$$

At the top of subgrade layer:

$$\begin{aligned} \tau_{all4} &= \frac{1}{F_{rel}} \cdot (c_{c2} \cdot k + \sigma \cdot \tan \varphi_{st2}) \\ &= 0.041 \text{ MPa} + \frac{0.0024 \text{ kN/m}^3 \cdot 0.17 \text{ m} + 0.0016 \text{ kN/m}^3 \cdot 0.10 \text{ m}}{0.17 \text{ m} + 0.10 \text{ m}} * \tan 0^\circ \\ &= 0.0413 \text{ MPa} \end{aligned}$$

Verification of shear failure at each evaluation point was conducted by comparing the calculated maximum active shear stresses with the corresponding allowable shear resistance. Shear verifications at all evaluation points are presented in Table 7.5.

Table 7.5 Shear failure verifications

Critical Depth	Transversal Position No.	Maximum Active Shear Stress (MPa)	Shear resistance (MPa)	Verifications
Base_Top	1	0.037	0.060	Yes
	2	0.038		Yes
	3	0.023		Yes
	4	0.022		Yes
Base_Middle	1	0.035	0.061	Yes
	2	0.042		Yes
	3	0.038		Yes
	4	0.038		Yes
Base_Bottom	1	0.035	0.062	Yes
	2	0.051		Yes
	3	0.052		Yes
	4	0.052		Yes
Subgrade_Top	1	0.035	0.0413	Yes
	2	0.041		Yes
	3	0.041		Yes
	4	0.041		Yes

As shown in Table 7.5, the maximum active shear stresses at all the evaluation points were all lower than its allowable shear strength, indicating that the pavement had adequate shear strength to accommodate the considered heaviest axle load without the occurrence of shear failure.

However, the above presented results evaluated below the transversal evaluation positions 1, 2 and 3 could only indicate the partial fulfillment of shear stability, except the evaluation point 4 at which the abruptness of full equilibrium of shear stability was identified. This is because, as explained in Section 5.1.2, the stress states calculated at evaluation positions 1, 2 and 3 were not subjected to the volumetric stress conditions.

Thus, to predict shear failures that disrupt full limit equilibrium in pavements under volumetric stress conditions, the dual-wheel load was converted to an Equivalent Single-Wheel Load (ESWL). This was done by considering the equal

vertical deformations at the most critical point in the pavement induced by these two types of loads, as described in Section 5.1.2. In this study, according to the results presented in Table 7.4, the most critical point can be identified as below the transversal evaluation position No. 4 on the bottom of base layer. Subsequently, by applying the “trial and error” calculating approach in the AVLA computational program, the ESWL was determined with the equal vertical deflection of 0.5414 mm at the bottom of base layer, the determined ESWL load configuration is presented in Table 7.6.

Table 7.6 The configuration of defined Equivalent Single-Wheel Load

Equivalent Single-Wheel Load (kN)	Tire pressure (kPa)	Load radius (mm)
66.37	700	173.73

By following the same evaluation processes, the maximum active shear stress and the corresponding allowable shear strength were calculated at evaluation points (Fig 7.7) located below the center of the defined ESWL at four critical depths in the pavement (i.e., at the top of both base and subgrade layers, and at the middle and bottom of base layer).

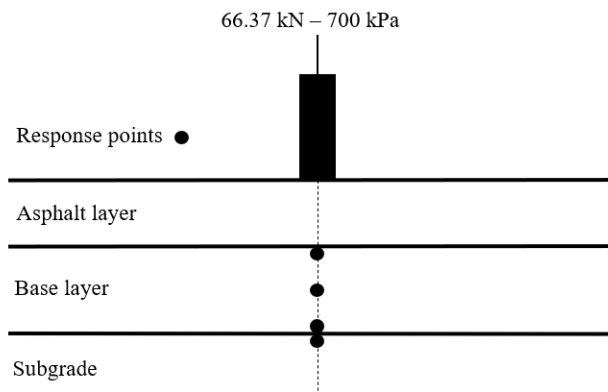


Figure 7.7 Evaluation points in the pavement under ESWL

Table 7.7 shows the resulting values of the maximum active shear stresses calculated at defined evaluation points in the same pavement section with the same layer thicknesses as analyzed previously, alongside the shear stability verifications.

Table 7.7 Maximum active shear stresses and shear stability verifications

Critical Depth	Stress Components			Principal Stresses		Maximum Active Shear Stress (MPa)	Shear resistance (MPa)	Verifications
	Sigma _x (MPa)	Sigma _z (MPa)	Sigma _{xz} (MPa)	Sigma ₁ (MPa)	Sigma ₃ (MPa)			
Base_Top	-0.021	0.154	0.000	0.154	-0.021	0.057	0.060	Yes
Base_Middle	-0.029	0.121	0.000	0.121	-0.029	0.062	0.061	No
Base_Bottom	-0.040	0.099	0.000	0.099	-0.040	<u>0.075</u>	0.062	No
Subgrade_Top	0.001	0.099	0.000	0.099	0.001	0.016	0.041	Yes

An immediate observation that can be made from the results shown in Table 7.7 is that the predicted shear stresses at the evaluation points in the base layer under ESWL were all greater than those under the dual-wheel load at the same evaluation points. Meanwhile, the shear resistance remained unchanged, resulting in shear failures in the pavement. This implies that the converted ESWL load configuration generally leads to more conservative predictions of shear failure potential.

This is to be expected, as it is believed that the two loads adjacent to the central axle increase the compressive stresses in the horizontal directions, due to the relatively high friction angle of granular layer materials, a higher state of compression would result a lower shear stress. Additionally, because of its higher confinement, it leads to higher modulus values in the layer materials, which in turn results in a lower deviatoric stress component. This results in less critical shear stress values being calculated in the pavement under dual-wheel load compared to converted ESWL.

Nonetheless, the predefined pavement structure was not verified in terms of shear stability. To guarantee the shear stability of the designed pavement section, a thicker pavement structure would be necessary, such as one that consisting of 20 cm of asphalt layer. However, this type of pavement structure may not be practical or feasible in the current state of practice in the solar farms.

Therefore, several redefined pavement structures were assumed and analyzed again. The redefined pavement structures are presented in Table 7.8.

Table 7.8 Redefined pavement structures in solar farm

Pavement structure No.	Layer thickness (cm)	
	Asphalt layer	Base layer
Structure No. 1	15	10
Structure No. 2	15	18
Structure No. 3	15	30

It is noted that in all the redefined pavement structures, in order to be representative of a real case in the pavement structural design in solar farms, the thickness of asphalt layer was limited to a value of 15 cm, and that of 30 cm for base layer. Since it is believed unrealistic structures that do not represent the actual state of practice in the pavement structural design in the solar farms will be made if the defined thicknesses of asphalt and base layers surpass these two limit values.

Although the pavement structure changed, the most critical environmental condition was still situated in analysis period No. 8. Therefore, by recalculating the mechanical properties of layer materials in this analysis period according to the layer thicknesses and by following the same evaluation processes, the maximum active shear stress and the corresponding allowable shear strength were calculated at each of evaluation points (Fig. 7.5) in all the redefined pavement structures. The resulting stress components and calculated active shear stresses and resistances at each evaluation point were compared to one another for each redefined pavement structure (Table 7.9 to 7.11).

Table 7.9 Maximum active shear stresses results and verifications (Structure No.1)

Critical Depth	Transversal Position No.	Stress Components			Principal Stresses		Maximum Active Shear Stress (MPa)	Shear resistance	Verifications
		Sigma x (MPa)	Sigma z (MPa)	Sigma xz (MPa)	Sigma 1 (MPa)	Sigma 3 (MPa)			
Base_Top	1	0.009	0.102	-0.053	0.126	-0.015	<u>0.043</u>	0.059	Yes
	2	-0.005	0.151	-0.025	0.155	-0.009	0.040		Yes
	3	0.004	0.148	-0.001	0.148	0.004	0.019		Yes
	4	0.005	0.148	0.000	0.148	0.005	0.018		Yes
Base_Middle	1	0.000	0.086	-0.039	0.101	-0.016	0.040	0.060	Yes
	2	-0.014	0.119	-0.022	0.122	-0.018	<u>0.046</u>		Yes
	3	-0.013	0.124	-0.002	0.124	-0.013	0.040		Yes
	4	-0.013	0.124	0.000	0.124	-0.013	0.039		Yes
Base_Bottom	1	-0.009	0.075	-0.027	0.083	-0.017	0.039	0.061	Yes
	2	-0.026	0.098	-0.016	0.100	-0.028	0.058		Yes
	3	-0.028	0.105	-0.002	0.105	-0.028	0.058		Yes
	4	-0.028	0.105	0.000	0.105	-0.028	<u>0.058</u>		Yes
Subgrade_Top	1	0.014	0.075	-0.027	0.085	0.004	0.041	0.041	Yes

	2	0.009	0.098	-0.016	0.101	0.007	0.047		No
	3	0.010	0.105	-0.002	0.105	0.010	<u>0.048</u>		No
	4	0.010	0.105	0.000	0.105	0.010	0.048		No

Table 7.10 Maximum active shear stresses results and verifications (Structure No.2)

Critical Depth	Transversal Position No.	Stress Components			Principal Stresses		Maximum Active Shear Stress (MPa)	Shear resistance	Verifications
		Sigma x (MPa)	Sigma z (MPa)	Sigma xz (MPa)	Sigma 1 (MPa)	Sigma 3 (MPa)			
Base_Top	1	0.011	0.111	-0.065	0.143	-0.021	<u>0.056</u>	0.059	Yes
	2	-0.006	0.172	-0.032	0.177	-0.011	0.047		Yes
	3	0.007	0.166	-0.001	0.167	0.007	0.018		Yes
	4	0.008	0.165	0.000	0.165	0.008	0.017		Yes
Base_Middle	1	-0.007	0.079	-0.041	0.096	-0.023	0.050	0.061	Yes
	2	-0.020	0.108	-0.024	0.113	-0.024	<u>0.054</u>		Yes
	3	-0.021	0.114	-0.003	0.115	-0.021	0.050		Yes
	4	-0.021	0.115	0.000	0.115	-0.021	0.050		Yes
Base_Bottom	1	-0.023	0.060	-0.021	0.065	-0.028	0.052	0.063	Yes
	2	-0.041	0.076	-0.013	0.077	-0.042	0.075		No
	3	-0.047	0.082	-0.002	0.082	-0.047	0.082		No
	4	-0.047	0.082	0.000	0.082	-0.047	<u>0.082</u>		No
Subgrade_Top	1	0.007	0.060	-0.021	0.067	0.000	0.034	0.041	Yes
	2	0.003	0.076	-0.013	0.078	0.001	0.039		Yes
	3	0.002	0.082	-0.002	0.082	0.002	0.040		Yes
	4	0.002	0.082	0.000	0.082	0.002	<u>0.040</u>		Yes

Table 7.11 Maximum active shear stresses results and verifications (Structure No.3)

Critical Depth	Transversal Position No.	Stress Components			Principal Stresses		Maximum Active Shear Stress (MPa)	Shear resistance	Verifications
		Sigma x (MPa)	Sigma z (MPa)	Sigma xz (MPa)	Sigma 1 (MPa)	Sigma 3 (MPa)			
Base_Top	1	0.016	0.124	-0.073	0.161	-0.021	<u>0.059</u>	0.059	Yes
	2	-0.001	0.196	-0.034	0.202	-0.007	0.044		Yes
	3	0.016	0.189	0.000	0.189	0.016	0.009		Yes
	4	0.017	0.188	0.000	0.188	0.017	0.007		Yes
Base_Middle	1	-0.008	0.069	-0.038	0.085	-0.024	0.049	0.062	Yes
	2	-0.018	0.093	-0.024	0.098	-0.023	<u>0.050</u>		Yes
	3	-0.020	0.101	-0.004	0.101	-0.021	0.047		Yes
	4	-0.020	0.101	0.000	0.101	-0.020	0.047		Yes
Base_Bottom	1	-0.031	0.043	-0.014	0.046	-0.033	0.056	0.065	Yes
	2	-0.045	0.052	-0.009	0.053	-0.046	0.076		No
	3	-0.052	0.056	-0.002	0.056	-0.052	0.085		No

	4	-0.052	0.056	0.000	0.056	-0.052	<u>0.085</u>		No
Subgrade_Top	1	0.003	0.043	-0.014	0.047	-0.002	0.025	0.041	Yes
	2	0.000	0.052	-0.009	0.053	-0.002	0.028		Yes
	3	-0.001	0.056	-0.002	0.056	-0.001	<u>0.029</u>		Yes
	4	-0.001	0.056	0.000	0.056	-0.001	0.029		Yes

It can be seen from the results shown from Table 7.9 to 7.11 is that all the redefined structures, which featured an asphalt layer thickness of 15 cm and a base layer thickness of less than or equal to 30 cm, were not satisfied with shear stability checks. Nonetheless, some important observations that can be made with regards to the correlation between the pavement structure and its ability to maintain shear stability when subjected to loading.

The most critical points in the pavement in terms of shear failure were situated at the top of subgrade layer in the pavement composing a thick asphalt layer and a comparatively thin base layer. In cases where the thickness of the asphalt layer remained the same and only the thickness of the base layer was increased, the active shear stresses at the base layer's bottom experienced a significant rise, leading to a greater potential of shear failure at the bottom of base layer as compared to the subgrade. Furthermore, if the thickness of the base layer continued to increase, the shear stress in the subgrade would decrease significantly, while the shear stress level in the base layer would experience a moderate rise, thus continuing to remain the most critical area prone to shear failure in the base layer.

These findings suggest that the thickness and mechanical properties of the layer above have a greater influence on the likelihood of shear failure in the layer below than the properties of the layer itself. Additionally, if the thicknesses of the other layers remain unchanged, increasing the thickness of a particular layer would result in an increase in shear stress within that layer, while the shear stress in the layer below could be effectively controlled.

7.3.3 Fatigue Cracking and Rutting Design

In this section, the previously defined pavement structure No. 1 (Table 7.12) in regards the designs of load-induced shear stability were evaluated in terms rutting and fatigue cracking. Twelve multi-layer elastic systems were assumed as reference structural models according to 12 analysis periods in predicting rutting and fatigue cracking in the defined pavement structure. Each multi-layer system, which corresponds to a specific analysis period, was characterized by the mechanical properties of the materials estimated in the corresponding analysis period and the defined thicknesses of all the layers composing the pavement structure (Table 7.13). It was assumed that each material is considered as linearly

elastic, homogeneous, isotropic and each layer is indicated as infinite in lateral extension and characterized by a constant thickness, except for the subgrade, which is modelled as a homogeneous infinite half-space.

Table 7.12 Pavement structure in fatigue and rutting design

Layer	Thickness (cm)	Material
Asphalt layer	15	Mix-A (see Section 5.3.4)
Base layer	10	Crushed limestone

Table 7.13 Mechanical properties in fatigue and rutting design (MPa)

Analysis period	1	2	3	4	5	6	7	8	9	10	11	12
Surface course $ E^* $	11775	11108	8435	6541	4819	3393	2950	2786	4004	6147	8311	11223
Base course E_{MG}	193	191	187	187	181	176	174	174	177	181	188	192
Subgrade M_R	121	121	118	118	114	111	110	109	111	114	118	121

The load applied to each multi-layer system was considered as the reference 80 kN axle in dual tire configuration. However, for structural analysis purposes, only the semi-axle was considered. The reference semi-axle consists of two circular loads, each with a 20 kN load, and a uniform pressure of 700 kPa. Dual spacing was assumed to be 0.35 m.

The stress-strain responses of each multi-layer system structure under loading were computed at critical depths. To predict fatigue resistance, the principal horizontal tensile strain at the bottom of the base asphalt layer was determined, with the assumption made of the top and base asphalt layers are fully bounded and considered as an integral asphalt layer in this structural analysis. The vertical compressive strain on the top of the subgrade was considered in estimating the critical response for rutting. Additionally, such responses were evaluated at three distinct transversal positions. The evaluated response points and the applied semi-axle load configuration were presented in Figure 7.8.

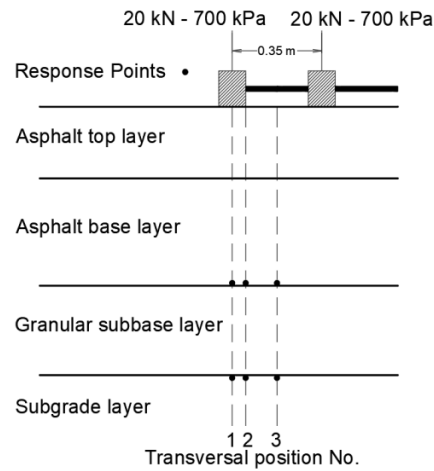


Figure 7.8 Evaluated response points within pavement

The numerical solutions of the structural response in the pavement under loading at each of previously defined response points were obtained for every multi-layer elastic system in each of 12 analysis periods by using an open-source MATLAB[®] based code titled: Adaptive Layered Viscoelastic Analysis (ALVA). Once the principal critical responses of pavement structure in each analysis period were computed, two transfer functions were used to predict the number of standard load applications that would lead to limiting conditions in terms of fatigue cracking and rutting. The Annex entailed the descriptions of these two transfer functions and the incremental damage calculations. The parameters used in each transfer function were calculated/assumed and presented in Table 7.14.

Table 7.14 Parameters used in transfer functions

Fatigue cracking	
Parameters	Values
Reliability parameter	Assumed equal to 6
Lab. shift factor	Assumed equal to 10
Self-healing shift factor	Assumed equal to 1
f_1	$f_1 = (6918 \cdot 10^{-6} \cdot (0.856 \cdot V_b + 1.08))^5$ $= (6918 \cdot 10^{-6} \cdot (0.865 \cdot 12\% + 1.08))^5$ $= 2.99 \cdot 10^{-6}$
f_2	Assumed equal to 5
f_3	Assumed equal to 1.8
Rutting	
Parameters	Values
f_4	Assumed to be $6.15 \cdot 10^{-7}$
f_5	Assumed equal to 4

The ESALs of 301888 estimated from 23359 heavy and OW/OS vehicles resulted from the analyses conducted in Chapter 6 were assumed to be evenly distributed in each of 12 analysis periods. Consequently, the fatigue and rutting damages resulting from each analysis period were identified by comparing the actual ESALs obtained from the traffic spectrum analysis to the predicted limiting number of load application resulting from transfer functions for the corresponding analysis period. The rutting and fatigue damages resulting at the end of the 30-year design period in each analysis period were respectively added together and are presented in Table 7.15.

Table 7.15 Predicted fatigue and rutting damages in solar farm pavement

Total Fatigue Damage D_f	0.019
Total Rutting Damage D_r	0.012

As shown in Table 7.15, the values of the predicted fatigue and rutting damages were much below unity, indicating that the pavement was overdesigned regards the resistance to fatigue and rutting when to consider the fulfillment of the shear stability in the pavement.

To assess the magnitude of overdesigning, another pavement structure was defined as shown in Table 7.16 to solely consider the design criteria in terms of fatigue and rutting.

Table 7.16 Pavement structure in fatigue and rutting design (2)

Layer	Thickness (cm)	Material
Asphalt layer	7	Mix-A (see Section 5.3.4)
Base layer	8.5	Crushed limestone

The layers mechanical properties were subsequently calculated and are presented in Table 7.17.

Table 7.17 Mechanical properties in fatigue and rutting design (MPa) (2)

Analysis period	1	2	3	4	5	6	7	8	9	10	11	12
Surface course $ E^* $	11661	10971	8216	6283	4548	3136	2704	2545	3737	5884	8090	11090
Base course E_{MG}	179	178	174	174	168	164	162	161	164	169	175	178
Subgrade M_R	121	121	118	118	114	111	110	109	111	114	118	121

By following the same calculation processes, the rutting and fatigue damages resulting from 301888 ESALs were determined and are presented in Table 7.18.

Table 7.18 Predicted fatigue and rutting damages in solar farm pavement

Total Fatigue Damage D_f	0.97
Total Rutting Damage D_r	0.39

Table 7.18 shows that by maximum use of the pavement resistances in terms of the fatigue and rutting damages, leading to designed asphalt and base layer thicknesses that were approximately half of those analyzed in the structure outlined in Table 7.12. This implies that when to consider the shear stability together in the structural pavement design by following the Russian pavement design guide, the pavement thickness would need to be designed roughly doubled compared to when only considering fatigue and rutting resistance in the designs.

7.4 Pavement Design for Wind Farm

In the structural pavement design for the proposed wind farm, the same design processes were followed as which conducted previously in the designs for solar farm. First, the mechanical properties of each layer composing the pavement section were defined according to the composing materials and predefined thickness of each layer. Then, the shear stability was checked in the pavement which subjected to the heaviest axle load by following the Russian pavement design guide, and the fatigue cracking in the asphalt layer and rutting deformation in the subgrade were subsequently checked to the same pavement structure.

7.4.1 Determinations of Layer Mechanical Properties

A pavement cross section was pre-defined in the proposed wind farm with the following layer thicknesses:

- A HMA surface layer measuring 8-cm depth;
- An unbound granular base layer constructed with crushed limestone with a depth of 16 cm; and
- A homogeneous subgrade layer composed of high plastic clay (CH) soils.

By following the same calculation procedures in the definition of layers mechanical properties as processed in Section 7.3, the moduli of the layers corresponding to each analysis period were calculated and are presented in Table 7.19. The Poisson's coefficients of the asphalt layers and subgrade layer were assumed to be 0.35, the unbound base layer was assumed to have a Poisson's coefficient equal to 0.30.

Table 7.19 Mechanical properties in 12 analysis periods (MPa)

Analysis period	1	2	3	4	5	6	7	8	9	10	11	12
Surface course $ E^* $	11679	10992	8250	6323	4589	3175	2741	2582	3778	5924	8124	11111
Subbase course E_{MG}	238	237	231	232	223	218	215	214	218	224	232	237
Subgrade M_R	121	121	118	118	114	111	110	109	111	114	118	121

The cohesion and angle of internal friction values for fat clayey soil and crushed limestone and densities of each layer were considered to be the same as that of defined in the pavement design for solar farm. The selected values can be found in Table 7.2 and 7.3 as presented in Section 7.3.

7.4.2 Shear Stability Design

The same as the designs for solar farm, the eighth analysis period was found to be subjected to the most critical environmental condition, and the materials mechanical properties of this analysis period were subsequently used in the shear stability designs.

The load applied to the multi-layer system was considered as the heaviest axle load as determined in Section 7.2. The load model illustrated in Figure 7.2 was simplified into a semi-axle load in the structural analysis. Pavement responses at 64 most critical locations, as shown in Figure 7.9, within the pavement section were evaluated. These locations included four critical depths and sixteen distinct transversal positions, as described in Section 7.1.2.

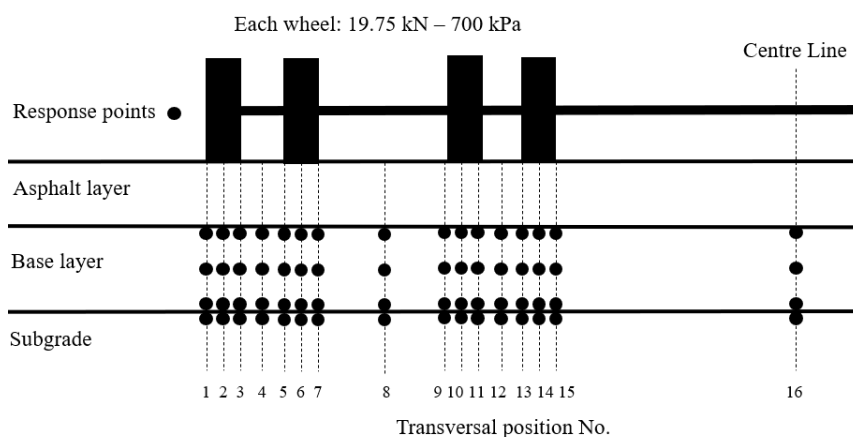


Figure 7.9 Evaluated response points within pavement - Wind farm

Subsequently, by following the same calculations as shown in Section 7.3, the active shear stresses at each evaluation point can be determined. The resulting values are listed in Table 7.20.

Table 7.20 Maximum active shear stresses results

Critical depth	Transversal Position No.	Stress Components			Principal Stresses		Maximum Active Shear Stress (MPa)
		Sigma _x (MPa)	Sigma _z (MPa)	Sigma _{xz} (MPa)	Sigma ₁ (MPa)	Sigma ₃ (MPa)	
Base_Top	1	0.033	0.151	-0.083	0.194	-0.010	<u>0.047</u>
	2	0.018	0.244	-0.021	0.246	0.016	0.020
	3	0.050	0.177	0.033	0.185	0.042	-0.030
	4	0.068	0.132	-0.001	0.132	0.068	-0.076
	5	0.051	0.177	-0.036	0.187	0.042	-0.029
	6	0.020	0.245	0.018	0.246	0.019	0.015
	7	0.038	0.152	0.078	0.191	-0.001	0.035
	8	0.034	0.018	0.000	0.034	0.018	-0.020
	9	0.038	0.152	-0.078	0.191	-0.001	0.035
	10	0.020	0.245	-0.018	0.246	0.019	0.015
	11	0.051	0.177	0.036	0.187	0.042	-0.029
	12	0.068	0.132	0.001	0.132	0.068	-0.076
	13	0.050	0.177	-0.033	0.185	0.042	-0.030
	14	0.018	0.244	0.021	0.246	0.016	0.020
	15	0.033	0.151	0.083	0.194	-0.010	0.047
	16	0.002	0.000	0.002	0.003	-0.001	0.002
Base-Middle	1	0.006	0.096	-0.049	0.118	-0.015	<u>0.043</u>
	2	-0.004	0.133	-0.022	0.136	-0.007	0.033
	3	0.008	0.122	0.002	0.122	0.008	0.009
	4	0.015	0.112	-0.002	0.112	0.015	-0.003
	5	0.010	0.122	-0.006	0.122	0.010	0.007
	6	0.001	0.134	0.017	0.136	-0.001	0.025
	7	0.013	0.099	0.042	0.116	-0.004	0.025
	8	0.034	0.029	0.000	0.034	0.029	-0.036
	9	0.013	0.099	-0.042	0.116	-0.004	0.025
	10	0.001	0.134	-0.017	0.136	-0.001	0.025
	11	0.010	0.122	0.006	0.122	0.010	0.007
	12	0.015	0.112	0.002	0.112	0.015	-0.003
	13	0.008	0.122	-0.002	0.122	0.008	0.009
	14	-0.004	0.133	0.022	0.136	-0.007	<u>0.033</u>

	15	0.006	0.096	0.049	0.118	-0.015	0.043
	16	0.005	0.000	0.002	0.006	0.000	0.002
Base-Bottom	1	-0.014	0.065	-0.025	0.073	-0.022	0.044
	2	-0.028	0.083	-0.015	0.085	-0.030	<u>0.059</u>
	3	-0.024	0.086	-0.006	0.086	-0.024	0.050
	4	-0.020	0.086	-0.003	0.086	-0.020	0.043
	5	-0.021	0.087	0.000	0.087	-0.021	0.046
	6	-0.022	0.084	0.009	0.085	-0.023	0.048
	7	-0.005	0.069	0.017	0.073	-0.008	0.025
	8	0.035	0.035	0.000	0.035	0.035	-0.045
	9	-0.005	0.069	-0.017	0.073	-0.008	0.025
	10	-0.022	0.084	-0.009	0.085	-0.023	0.048
	11	-0.021	0.087	0.000	0.087	-0.021	0.046
	12	-0.020	0.086	0.003	0.086	-0.020	0.043
	13	-0.024	0.086	0.006	0.086	-0.024	0.050
	14	-0.028	0.083	0.015	0.085	-0.030	<u>0.059</u>
	15	-0.014	0.065	0.025	0.073	-0.022	0.044
	16	0.008	0.001	0.003	0.009	0.000	0.002
Subgrade-Top	1	0.011	0.065	-0.025	0.075	0.001	0.037
	2	0.009	0.083	-0.015	0.086	0.006	<u>0.040</u>
	3	0.012	0.086	-0.006	0.087	0.012	0.037
	4	0.014	0.086	-0.003	0.086	0.014	0.036
	5	0.014	0.087	0.000	0.087	0.014	0.037
	6	0.013	0.084	0.009	0.086	0.011	0.037
	7	0.017	0.069	0.017	0.074	0.012	0.031
	8	0.028	0.035	0.000	0.035	0.028	0.003
	9	0.017	0.069	-0.017	0.074	0.012	0.031
	10	0.013	0.084	-0.009	0.086	0.011	0.037
	11	0.014	0.087	0.000	0.087	0.014	0.037
	12	0.014	0.086	0.003	0.086	0.014	0.036
	13	0.012	0.086	0.006	0.087	0.012	0.037
	14	0.009	0.083	0.015	0.086	0.006	<u>0.040</u>
	15	0.011	0.065	0.025	0.075	0.001	0.037
	16	0.005	0.001	0.003	0.006	-0.001	0.003

Table 7.20 presents the results of the maximum active shear stress under the heaviest axle load in the pavement of proposed wind farm development based on the Mohr–Coulomb yield criterion in the plane stress state given by Equation 7.3. The values that are underlined in the results correspond to the most critical horizontal location at each corresponding vertical depth in the pavement.

Knowing the pavement layers mechanical and physical properties as defined earlier, and by the use of Equation 7.4, the allowable shear resistances in the base layer at three critical depths, and in the subgrade layer can be determined as follows:

At the top of subbase layer:

$$\begin{aligned}\tau_{all1} &= \frac{1}{F_{rel}} \cdot (c_{c1} \cdot k + \sigma \cdot \tan\varphi_{st1}) \\ &= 0.0544 \text{ MPa} + \frac{0.0024 \text{ kN/m}^3 \cdot 0.08 \text{ m}}{0.08 \text{ m}} * \tan 52^\circ \\ &= 0.057 \text{ MPa}\end{aligned}$$

At the middle of subbase layer:

$$\begin{aligned}\tau_{all2} &= \frac{1}{F_{rel}} \cdot (c_{c1} \cdot k + \sigma \cdot \tan\varphi_{st1}) \\ &= 0.0544 \text{ MPa} + \frac{0.0024 \text{ kN/m}^3 \cdot 0.08 \text{ m} + 0.0016 \text{ kN/m}^3 \cdot 0.08 \text{ m}}{0.08 \text{ m} + 0.08 \text{ m}} * \tan 52^\circ \\ &= 0.058 \text{ MPa}\end{aligned}$$

At the base of subbase layer:

$$\begin{aligned}\tau_{all3} &= \frac{1}{F_{rel}} \cdot (c_{c1} \cdot k + \sigma \cdot \tan\varphi_{st1}) \\ &= 0.0544 \text{ MPa} + \frac{0.0024 \text{ kN/m}^3 \cdot 0.08 \text{ m} + 0.0016 \text{ kN/m}^3 \cdot 0.16 \text{ m}}{0.08 \text{ m} + 0.16 \text{ m}} * \tan 52^\circ \\ &= 0.060 \text{ MPa}\end{aligned}$$

At the top of subgrade layer:

$$\begin{aligned}\tau_{all4} &= \frac{1}{F_{rel}} \cdot (c_{c2} \cdot k + \sigma \cdot \tan\varphi_{st2}) \\ &= 0.0413 \text{ MPa} + \frac{0.0024 \text{ kN/m}^3 \cdot 0.08 \text{ m} + 0.0016 \text{ kN/m}^3 \cdot 0.16 \text{ m}}{0.08 \text{ m} + 0.16 \text{ m}} * \tan 0^\circ \\ &= 0.0413 \text{ MPa}\end{aligned}$$

Shear stability verifications at all evaluation points are presented in Table 7.21.

Table 7.21 Shear failure verifications – Wind farm

Critical depth	Transversal Position No.	Maximum Active Shear Stress (MPa)	Shear resistance (MPa)	Verifications
Base_Top	1	<u>0.047</u>	0.057	Yes
	2	0.020		Yes
	3	-0.030		Yes
	4	-0.076		Yes

	5	-0.029		Yes
	6	0.015		Yes
	7	0.035		Yes
	8	-0.020		Yes
	9	0.035		Yes
	10	0.015		Yes
	11	-0.029		Yes
	12	-0.076		Yes
	13	-0.030		Yes
	14	0.020		Yes
	15	0.047		Yes
	16	0.002		Yes
Base_Middle	1	<u>0.043</u>	0.058	Yes
	2	0.033		Yes
	3	0.009		Yes
	4	-0.003		Yes
	5	0.007		Yes
	6	0.025		Yes
	7	0.025		Yes
	8	-0.036		Yes
	9	0.025		Yes
	10	0.025		Yes
	11	0.007		Yes
	12	-0.003		Yes
	13	0.009		Yes
	14	<u>0.033</u>		Yes
	15	0.043		Yes
	16	0.002		Yes
Base_Bottom	1	0.044	0.060	Yes
	2	<u>0.059</u>		Yes
	3	0.050		Yes
	4	0.043		Yes
	5	0.046		Yes
	6	0.048		Yes
	7	0.025		Yes
	8	-0.045		Yes
	9	0.025		Yes
	10	0.048		Yes
	11	0.046		Yes
	12	0.043		Yes
	13	0.050		Yes
	14	<u>0.059</u>		Yes

	15	0.044		Yes
	16	0.002		Yes
Subgrade_Top	1	0.037	0.041	Yes
	2	<u>0.040</u>		Yes
	3	0.037		Yes
	4	0.036		Yes
	5	0.037		Yes
	6	0.037		Yes
	7	0.031		Yes
	8	0.003		Yes
	9	0.031		Yes
	10	0.037		Yes
	11	0.037		Yes
	12	0.036		Yes
	13	0.037		Yes
	14	<u>0.040</u>		Yes
	15	0.037		Yes
	16	0.003		Yes

As shown in Table 7.21, the maximum active shear stresses at all the evaluation points were all lower than its allowable shear strength, indicating that the pavement had adequate shear strength to accommodate the considered heaviest axle load without the occurrence of shear failure.

However, the above presented results could only indicate the fulfillment of partial shear stability at most of the evaluated critical points. This is because, as explained in Section 5.1.2, the stress states calculated at the predefined estimation points were not subjected to the volumetric stress conditions, except the positions where the tangential stresses were determined equal to zero. Thus, to predict shear failures that disrupt full limit equilibrium in pavements under volumetric stress conditions, the dual-wheel load was converted to an Equivalent Single-Wheel Load (ESWL). This was done by considering the equal vertical deformations at the most critical point in the pavement induced by these two types of loads, as described in Section 5.1.2.

In this study, according to the results presented in Table 7.20, the most critical point can be identified as below the center of the outmost wheel load, at the critical depth of at the bottom of base layer. Subsequently, by using the AVLA computational program, the ESWL was determined with an equal vertical deformation at the bottom of base layer of 0.5108 mm, the ESEL load configuration is presented in Table 7.22.

Table 7.22 The configuration of defined Equivalent Single-Wheel Load (Wind farm)

Equivalent Single-Wheel Load (kN)	Tire pressure (kPa)	Load radius (mm)
44.75	700	142.65

By following the same evaluation processes, the maximum active shear stress and the corresponding allowable shear strength were calculated at evaluation points located below the center of the defined ESWL at four critical depths in the pavement (i.e., at the top of both subbase and subgrade layers, and at the middle and bottom of subbase layer). For the same reason as explained in Section 7.3.2, due to a lower confinement stress in the pavement under ESWL compared to that of under multiple wheel load, which leads to a higher shear stress, and in turn, the pavement structure was not verified under ESWL in terms of shear stability.

Therefore, to ensure the shear stability of the designed pavement section, thicker asphalt layer would be needed. By increasing the asphalt layer thickness up to 17 cm, while simultaneously reducing the base layer thickness to 11 cm, the shear stability in all layers can be verified. The resulting values and the verifications are presented below in Table 7.23.

Table 7.23 Shear verifications under ESWL

Critical depth	Maximum Active Shear Stress (MPa)	Shear resistance (MPa)	Verifications
Base_Top	0.042	0.060	Yes
Base_Middle	0.047	0.061	Yes
Base_Bottom	0.060	0.062	Yes
Subgrade_Top	0.039	0.041	Yes

Again, as observed in the solar farm pavement design, to guarantee the shear stability of the designed pavement section, a thick pavement structure that consisting of a 17 cm of asphalt layer was designed. However, this type of pavement structure may not be practical or feasible in the current state of practice in the wind farm pavement design.

7.4.3 Fatigue Cracking and Rutting Design

By following the same structural analysis methodology and the calculation procedures as conducted in Section 7.3.2, an estimate was made of the fatigue cracking and rutting damages in a previously confirmed, unrealistic pavement section. The assessment was based on 679157 ESALs homogenized from a combination of 46461 heavy vehicles and OW/OS vehicles. The resulting values are presented in Table 7.24.

Table 7.24 Predicted fatigue and rutting damages in solar farm pavement

Total Fatigue Damage D_f	0.018
Total Rutting Damage D_r	0.013

The results presented in Table 7.24 revealed that the estimated values for fatigue and rutting damages were significantly lower than unity, thus, the pavement was substantially overdesigned regards the resistance to fatigue and rutting when considering the fulfillment of shear stability in the pavement.

In order to determine the extent of overdesign, a pavement structure was defined, as outlined in Table 7.25, with the sole purpose of evaluating the design standards with regards to fatigue and rutting.

Table 7.25 Pavement structure in fatigue and rutting design – Wind farm

Layer	Thickness (cm)	Material
Asphalt layer	8	Mix-A (see Section 5.3.4)
Base layer	11	Crushed limestone

The layers mechanical properties were subsequently calculated and are presented in the table below.

Table 7.26 Mechanical properties in fatigue and rutting design – Wind farm

Analysis period	1	2	3	4	5	6	7	8	9	10	11	12
Surface course $ E^* $	11679	10992	8250	6323	4589	3175	2741	2582	3778	5924	8124	11111
Base course E_{MG}	201	200	195	196	189	184	182	181	184	189	196	200
Subgrade M_R	121	121	118	118	114	111	110	109	111	114	118	121

By following the same calculation processes, the rutting and fatigue damages resulting from 679157 ESALs were determined and are presented in Table 7.27.

Table 7.27 Predicted fatigue and rutting damages in wind farm pavement

Total Fatigue Damage D_f	0.91
Total Rutting Damage D_r	0.30

According to Table 7.27, the resistances of pavement structure to fatigue and rutting damages was effectively used, resulting in an asphalt layer thickness in the designed structure that was only half of the analyzed thickness designed in satisfying shear stability requirements. This indicates that when to consider the shear stability together in the structural pavement design by following the Russian pavement design guide for the proposed wind farm, the asphalt layer thickness

would need to be designed roughly doubled compared to when only considering fatigue and rutting resistance in the designs.

7.5 Summary

The structural design of asphalt pavements in the proposed wind and solar energy plants in the definition of a mechanistic-empirical methodology was developed in this chapter. More specifically, the structural design criteria considered during the design process included fatigue cracking, rutting deformation, and load-induced local shear failure. The extent of damage resulting from fatigue cracking and rutting were analyzed in 12 analysis periods using empirical damage laws. The potential of load-induced shear failure was assessed in unbound layers accounts for the most critical environmental condition in the definition of a design approach according to the Russian flexible pavement design guide (ODN 218.046-01).

In the proposed solar farm, to guarantee the shear stability of the designed pavement section subjected to the heaviest axle of 139 kN with dual wheels, a thick pavement structure would be necessary, such as one that consisting of 20 cm of asphalt layer. However, this type of pavement structure may not be practical or feasible in the current state of practice of pavement designs in the solar farms. In order to be representative of a real case in the pavement structural design, three different pavement sections were assumed with the thickness of asphalt layer was limited to a value of 15 cm, and that of 30 cm for base layer. However, none of those was satisfied with shear stability checks. For the rutting and fatigue resistances design, a pavement featured with a 7 cm asphalt layer and an 8.5 cm crushed stone base layer would be capable of withstanding the ESALs of 301888 estimated from 23359 heavy and OW/OS vehicles resulted in the proposed solar farm.

In the proposed wind farm, a pavement structure consists of an 8 cm asphalt layer and a crushed stone base layer measuring 16 cm thickness could ensure the partial shear stability in the pavement under the anticipated heaviest axle load of 158 kN with quad-wheels configured within a five-axle group. However, to verify the shear abruption of full equilibrium in the unbound layers with the load applied on the pavement converted into an equivalent single-wheel load, the asphalt layer thickness would need to be increased up to 17 cm, while simultaneously to reduce the base layer thickness to 11 cm. This type of pavement structure is believed to be unrealistic and does not represent the actual state of practice in the pavement structural design in the wind farms. To solely consider fatigue and rutting design criteria in the design process, a combination of 8 cm asphalt layer and an 11 cm base layer would be satisfied to carry 679157 ESALs homogenized from a combination of 46461 heavy vehicles and OW/OS vehicles in the proposed wind farm.

Although there was not a realistic pavement structure realized in this chapter, from the results obtained throughout the design processes, the major findings and observations of the study effort in this chapter could be made and are summarized as follows:

- Conservative and unrealistic pavement structures would be designed in the proposed solar and wind farms, due to the high level of conservatism made of simplifying multi-axle load group to only one critical axle, and that of converting the dual-wheel load into an equivalent single-wheel load in the structural analysis.
- The converted ESWL load configuration from a dual-wheel generally leads to more conservative predictions of shear failure potential. As it is believed that the dual-wheel loads adjacent to the central axle increase the compressive stresses in the horizontal directions, due to the relatively high friction angle of granular layer materials, a higher state of compression would result a lower shear stress. Additionally, because of its higher confinement, it leads to higher modulus values in the layer materials, which in turn results in a lower deviatoric stress component.
- The most critical depth in the pavement regards shear failure was situated at the top of subgrade layer in the pavement composing a thick asphalt layer and a comparatively thin base layer. In cases where the thickness of the asphalt layer remained the same and increased the thickness of the base layer, a greater potential of shear failure could be observed at the bottom of base layer as compared to the subgrade.
- The thickness and mechanical properties of the layer above have a greater influence on the likelihood of shear failure in the layer below than the properties of the layer itself. Additionally, if the thicknesses of the other layers remain unchanged, increasing the thickness of a particular layer would result in an increase in shear stress within that layer, while the shear stress in the layer below could be effectively controlled.
- For the pavement structures and the corresponding mechanical properties considered, the pavement would be subjected to overdesign regards the resistance to fatigue and rutting when to consider the fulfillment of the shear stability simultaneously.

Chapter 8

Conclusions and Recommendations

This chapter summarizes the extensive efforts undertaken in this study to characterize an approach for structural design of asphalt pavements for renewable energy plants. The primary goal of this study was the definition of a mechanistic-empirical methodology for the structural design of asphalt pavements in facilitating the development of renewable energy plants, such as wind plants and solar plants. The proposed design criteria consisted of three categories, including the loaded-induced shear stability design in the unbound layers, fatigue cracking and rutting deformation resistance design in the asphalt layer and subgrade layer, respectively.

To achieve the study objectives, initially, the effects of climate on structural design were analyzed, with special emphasis on the role played by monthly variations of temperature and precipitation in the definition of the mechanical characteristics of both the asphalt layers and the subgrade soil. In all, three categories of multiple analysis periods (12 analysis periods, 5 analysis periods, and 3 analysis periods) were applied to quantify the influence of climate variation on material properties. The stiffness of asphalt layer was determined for each analysis period as a function of the average air temperature, a mathematical M_R -Moisture model was applied to estimate the changes in resilient modulus values of subgrade soils in response to variations in moisture content. The functional performances (i.e., fatigue and rutting resistances) of the pavement in each of three categories of multiple analysis periods were calculated, using the ALVA computing program based on MATLAB[®] following a mechanistic-empirical design methodology internally developed at Politecnico di Torino (in Annex), with material properties estimated from the corresponding multiple analysis periods to reflect the influence of climate variation on the damage accumulation in the pavement structural design.

As part of this study, considering the nature of heavy axle load of the vehicles employed in the development of renewable energy plants, the influence of the model used for traffic homogenization was estimated. By using the Mechanistic-Empirical Pavement Design Method, the analyses were made with the comparison of the variations in fatigue cracking the rutting damages caused by the same amount of traffic, but with the ESALs and stress-strain responses calculated with respected to two different standard axles, namely, a 120 kN single axle with twin wheels at a wheelbase distance of 0.375 m and 800 kPa inflation pressure, in accordance with the maximum values set by current Italian legislation (Highway Code), and a single axle of 80 kN with dual tires at a wheelbase distance of 0.35 m and 700 kPa inflation pressure as defined in the 2008 AASHTO mechanistic-empirical design method.

A rational approach for the evaluation of the potential of rapid load-induced shear failure in the unbound layers in accordance with the Russian structural pavement design guide (ODN 218.046-01) was further studied in this work. By adhering to this design guide, the potential for localized shear failure can be investigated through a rational approach based on the Mohr–Coulomb yield criterion in the plane stress state, wherein the maximum active shear stress generated by traffic loading is compared to the shear strength of the soil under critical environmental conditions.

Ultimately, an assessment was presented regarding the reference traffic spectra for a proposed wind plant and a proposed solar plant. By aggregating the findings derived from the aforementioned analyses, the structural designs for a wind farm and a solar farm were conducted.

The subsequent sections provide noteworthy observations and a summary of major findings pertaining to structural design of asphalt pavements for renewable energy plants. The conclusions are accompanied by recommendations for future study in the area of shear stability analysis and design for the pavement structures subjected to taxing loading conditions in renewable energy plants.

8.1 Conclusions

A summary of major findings of the thesis is provided as follows:

- A comprehensive analysis of the effects of climate on structural design confirmed the importance of using 12 analysis periods to define the mechanical properties of materials in pavement designs. Specifically, for the various models and parameters considered in this study, the fatigue cracking damage was underestimated by 2% and by 6% in rutting damage when using the materials properties derived from 3 analysis periods compared to those obtained from 12 analysis periods. This behavior was anticipated, as the pavement designs based on 5 or 3 analysis periods

neglect the significant damages that occur during brief periods of high temperature and/or moisture content, leading to unconservative designs, and in turn often resulting in poor performance and early deterioration of pavements.

- The reference axle used in traffic modeling highly influences the structural design. A modest increase of approximately 5 % in anticipated fatigue damage, and conversely, a significant decrease of 17 % in the projected rutting damage were determined, when replacing the 80 kN reference single axle and its corresponding load configuration with that of 120 kN in the traffic homogenization model. While the ESALs modeled with the 120 kN reference axle were about 5 times lower than those modeled with the 80 kN reference axle. Additionally, the principal tensile strains and compressive strains resulting from the 120 kN reference axle at the corresponding evaluation depth were, on average, approximately 1.4 times greater than that resulting from the 80 kN reference axle.
- For the development of wind and solar farms with the same power output capacity, the total vehicle passages in wind development were estimated roughly 1.6 times greater than that of solar development. Similarly, the number of heavy vehicles in wind energy development was double compared to that of solar development.
- On average, 11 OW/OS hauling vehicles would be necessary to install a single wind turbine, while the use of OW/OS vehicles in solar farm development was limited.
- The analysis of reference traffic spectra demonstrated that ESALs calculated for empty vehicles were approximately 1% of that for loaded vehicles, for both wind and solar developments.
- The shear stability design approach in accordance with the Russian structural pavement design guide (ODN 218.046-01) was investigated. The design approach is capable of evaluating the likelihood of shear failure at the evaluation points wherein the volumetric stress conditions are fulfilled. To determine the shear stability at several critical response points under multi-wheel load configurations, the volumetric stress conditions may not exist in some points. Therefore, the shear failure projected in those points can be only considered as a partial shear failure in accordance with the design method.
- To predict the shear disruption that achieves a complete limit equilibrium regards Mohr- Coulomb yield criterion in pavement under the simplified dual-wheel load, such a load configuration was converted into an equivalent single wheel load in order to analysis the critical points in the pavement wherein the volumetric stress state exist. However, the designs were found to contain a high level of conservatism, resulting unrealistic structures to be designed that do not represent the actual state of practice in the pavement structural design in the wind and solar farms.

- The shear stability analysis of pavement unbound layers indicated that the most critical depth was at the top of subgrade layer regards shear failure in the pavement composing a thick asphalt layer and a comparatively thin base layer. However, in cases where the thickness of the asphalt layer remained the same and increased the thickness of the base layer, a greater potential of shear failure could be observed at the bottom of base layer as compared to the subgrade.
- The thickness and mechanical properties of the layer above had a greater influence on the likelihood of shear failure in the layer below than the properties of the layer itself. Moreover, maintaining the thicknesses of other layers unchanged, increasing the thickness of a particular layer would result in an increase in shear stress in that layer, while the shear stress in the layer below could be effectively controlled.
- The structural design of asphalt pavements showed that, for the pavement structures and the corresponding mechanical properties considered, the pavement would be subjected to overdesign regards the resistance to fatigue and rutting when to consider the fulfillment of the shear stability simultaneously.

8.2 Recommendations for Future Works

The results of this study overestimated the shear stresses in the unbound pavement layers under the loads of super-heavy trailer operations, and in turn leading to a structural design with high level of conservatism. Accurate evaluations of rapid, load-induced shear stability are the prelude to designing asphalt pavements in renewable energy plants. In line with this necessity, the following items were outlined to be regarded as potential focus points for future studies associated with the analysis and design of transportation infrastructures in renewable energy plants that are exposed to non-conventional OW/OS vehicles.

- As a continuation of this study, future studies can deploy the analysis frameworks devised in this thesis for further implementation in the analysis of the shear stability in unbound layers varying pavement section materials. The results can be helpful in providing valuable insights into the definition of the critical depth in the pavement subjected to super-heavy vehicle loads.
- The shear stability design approach considered in this study is conservative in nature. In the future studies, it is worth evaluating the shear stability with the actual multi-axle load configurations of the critical load considered in the designs. This is of great importance, as it enables the determination of the exact level of stress state in the layer, thereby reducing any unnecessary assumptions and/or uncertainties, and resulting a representative design approach in the state of practice.

References

- Huang, Y. H. (2004). Pavement analysis and design. Upper Saddle River, Nj: Pearson Education.
- N. Thom. (2008). Principles of Pavement Engineering. Thomas Telford Publishing. <https://doi.org/10.1680/pope.34808>
- El-Badawy, S. M., Bayomy, F. M., Santi, M., & Clawson, C. W. (2011). Comparison of Idaho Pavement Design Procedure with AASHTO 1993 and MEPDG Methods. Transportation and Development Institute Congress 2011. [https://doi.org/10.1061/41167\(398\)56](https://doi.org/10.1061/41167(398)56)
- Christopher, B. R., Schwartz, C. W., Boudreaux, R., & Berg, R. R. (2006). Geotechnical aspects of pavements (No. FHWA-NHI-05-037). United States. Federal Highway Administration.
- Burmister, D. M. (1945). The General Theory of Stresses and Displacements in Layered Systems. I. Journal of Applied Physics, 16(2), 89–94. <https://doi.org/10.1063/1.1707558>
- Dehlen, G. L. (1969). The effect of non-linear material in the behavior of pavements subjected to traffic loads (Doctoral dissertation, PhD thesis, Univ. of California, Berkeley).
- American Association Of State Highway And Transportation Officials (AASHTO). (2008). Mechanistic-empirical pavement design guide : a manual of practice, July 2008. Washington, Dc: Aashto.

- Greene, J. S., & Geisken, M. (2013). Socioeconomic impacts of wind farm development: a case study of Weatherford, Oklahoma. *Energy, Sustainability and Society*, 3(1). <https://doi.org/10.1186/2192-0567-3-2>
- Prozzi, J.P., Grebenschikov, S., Banerjee, A., & Prozzi, J.A. (2011). Impacts of Energy Developments on the Texas Transportation System Infrastructure.
- Quiroga, C., Fernando, E., & Oh, J. (2012). Energy developments and the transportation infrastructure in Texas : impacts and strategies. (Texas Transportation Institute, Ed.).
- Burton, T., Sharpe, D., Jenkins, N., Bossanyi, E., & Al, E. (2004). *Wind energy : handbook*. Chichester Etc.: J. Wiley & Sons.
- The New South Wales Government (NSW). (2018). Wyalong Solar Farm | Planning Portal - Department of Planning and Environment. Retrieved March 1, 2023, from www.planningportal.nsw.gov.au website: <https://pp.planningportal.nsw.gov.au/major-projects/projects/wyalong-solar-farm>
- NCHRP. (2002). Contributions of Pavement Structural Layers to Rutting of Hot Mix Asphalt Pavements. National Cooperative Highway Research Program, Report n. 468.
- Mallick RB, El-Korchi T. (2009). *Pavement Engineering, Principles and Practice*. Ed. CRC Press, Taylor & Francis Group.
- Skar, A., and Andersen, S. (2020). ALVA: an adaptive MATLAB package for layered viscoelastic analysis. *Journal of Open-Source Software*, 5 (55), 2548.
- Skar, A., Andersen, S., and Nielsen, J. (2020a). Adaptive layered viscoelastic analysis (ALVA). Available from: <https://github.com/asmusskar/ALVA>

- EN 12697-24. (2018). Bituminous mixtures - Test methods - Part 24: Resistance to fatigue.
- ODN 218.046-01. State Road Service Ministry of Transportation of The Russian Federation. (2001). DESIGN OF FLEXIBLE ROAD PAVEMENTS (In Russian).
- (Nadia)Gkritza, K., Nlenanya, I., Jiang, W., Sperry, R., & Smith, D. (2011). Infrastructure Impacts of Iowa's Renewable Energy. Transportation Research Record: Journal of the Transportation Research Board, 2205(1), 238–246. <https://doi.org/10.3141/2205-30>
- Ahmed, A., Hossain, S., Khan, M. S., & Shishani, A. (2018). Data-Based Real-Time Moisture Modeling in Unsaturated Expansive Subgrade in Texas. Transportation Research Record: Journal of the Transportation Research Board, 2672(52), 86–95. <https://doi.org/10.1177/0361198118772960>
- Naji, K. (2016). Resilient modulus–moisture content relationships for pavement engineering applications. International Journal of Pavement Engineering, 19(7), 651–660. <https://doi.org/10.1080/10298436.2016.1199877>
- Kutay, M. E., & Jamrah, A. (2013). Preparation for Implementation of the Mechanistic-Empirical Pavement Design Guide in Michigan: Part 1 – HMA Mixture Characterization. (Michigan State University. Department of Civil and Environmental Engineering, Ed.).
- Gilbert Baladi, Dawson, T.A., & Sessions, C. (2009). Pavement subgrade MR design values for Michigan's seasonal changes : final report.

- Fredrick Lekarp, Isacson, U., & Dawson, A. (2000). State of the Art. I: Resilient Response of Unbound Aggregates. *Journal of Transportation Engineering- asce*, 126, 66-75.
- Raad, Lutfi, Minassian, George H, Gartin, Scott, 1992. Characterization of saturated granular bases under repeated loads. *Transp. Res. Rec.* 1369, Transportation Research Board, Washington, D.C., 73–82
- Xingwei Chen, Lambert, J. R., Tsai, C., & Zhang, Z. (2013). Evaluation of superheavy load movement on flexible pavements. *International Journal of Pavement Engineering*, 14(5), 440–448. <https://doi.org/10.1080/10298436.2012.690519>
- Jooste, F.J., & Fernando, E.G. (1995). Development of a procedure for the structural evaluation of superheavy load routes.
- Whitman, R. V., & Hoeg, K. (1966). Development of Plastic Zone Beneath a Footing. Report by MIT Department of Civil Engineering to US Army Engineering Waterways Experiment Station.
- Wind Europe. (2023). Wind energy in Europe: 2022 Statistics and the outlook for 2023-2027. Retrieved March 1, 2023, from WindEurope website: <https://windeurope.org/intelligence-platform/product/wind-energy-in-europe-2022-statistics-and-the-outlook-for-2023-2027/>
- SolarPower Europe. (2022). EU Market Outlook for Solar Power 2022-2026 - SolarPower Europe. Retrieved March 10, 2023, from www.solarpowereurope.org website: <https://www.solarpowereurope.org/insights/market-outlooks/eu-market-outlook-for-solar-power-2022-2026-2>

- SolarPower Europe. (2022a). Global Market Outlook For Solar Power 2022-2026 - SolarPower Europe. Retrieved March 10, 2023, from www.solarpowereurope.org website: <https://www.solarpowereurope.org/insights/market-outlooks/global-market-outlook-for-solar-power-2022#downloadForm>
- NWS. (2022). Daroobalgie Solar Farm Environmental Impact Statement – Appendix K Traffic and Transport Assessment Report | Planning Portal - Department of Planning and Environment. Retrieved March 10, 2023, from www.planningportal.nsw.gov.au website: <https://pp.planningportal.nsw.gov.au/major-projects/projects/daroobalgie-solar-farm>
- NWS. (2022a). Oxley Solar Farm– Appendix K Updated Traffic Impact Assessment (TIA) | Planning Portal - Department of Planning and Environment. Retrieved March 10, 2023, from www.planningportal.nsw.gov.au website: <https://pp.planningportal.nsw.gov.au/major-projects/projects/oxley-solar-farm>
- NWS. (2021). Glenellen Solar Farm Amendment Report – Appendix H - Revised Traffic Impact Assessment | Planning Portal - Department of Planning and Environment. Retrieved March 15, 2023, from www.planningportal.nsw.gov.au website: <https://pp.planningportal.nsw.gov.au/major-projects/projects/glenellen-solar-farm>
- Fotowatio Renewable Ventures (FRV). (2020). Metz solar farm traffic management plan. Retrieved February 22, 2023, from http://metzsolarfarm.com/wp-content/uploads/2021/02/MTSF-Traffic-Management-Plan_Companded.pdf

- Fotowatio Renewable Ventures (FRV). (2020a). Oversize transformer arrives at Winton solar farm site. Retrieved February 22, 2023, from <https://wintonsolarfarm.com/2020/10/26/oversize-transformer-arrives-at-winton-solar-farm-site/>
- The Manitowoc Company Inc. (2023). ALL-TERRAIN CRANES. Retrieved 27 February 2023. <https://www.manitowoc.com/grove/all-terrain-cranes>
- Steven D. Schrock, Udaipurwala, M., Han, J., & Parsons, R. L. (2017). Pavement deterioration due to horizontal hydraulic fracturing and wind farm development in Kansas : final report. (E. and A. E. University of Kansas. Dept. of Civil, Ed.). Retrieved from <https://rosap.nsl.bts.gov/view/dot/32124>
- W. Uddin, Barros, R., & Jaafar, Z. F. M. (2019). Sensitivity Analysis of Mechanistic-Empirical Pavement Structural Design Methods Considering Climate Impacts on Layer Modulus Values. *Bituminous Mixtures and Pavements VII*, 357–364. <https://doi.org/10.1201/9781351063265-51>
- Zuo, G., Drumm, E.C., & Meier, R.W. (2007). Environmental Effects on the Predicted Service Life of Flexible Pavements. *Journal of Transportation Engineering-asce*, 133, 47-56.
- P. Pereira, & Pais, J. (2017). Main flexible pavement and mix design methods in Europe and challenges for the development of an European method. *Journal of Traffic and Transportation Engineering (English Edition)*, 4(4), 316–346. <https://doi.org/10.1016/j.jtte.2017.06.001>
- JTJ D50. (2006). Design Specifications of Highway Asphalt Pavement. People's Transportation Press, Beijing

- LCPC and SETRA. (1994). Conception et dimensionnement des structures de chaussée: guide technique, The Central Laboratory for Roads and Bridges (LCPC), The Technical Studies Department of Roads and Motorways (SETRA), Paris, France.
- Powell, W. D., Potter, J. F., Mayhew, H. C., & Nunn, M. E. (1984). The structural design of bituminous roads (LR1132). Transport Research Laboratory, Crowthorne Berks. UK.
- Bellagamba G, Cariti G. (2010). The new highway codes. Giuffrè Editore. (In Italian)
- Renato Lancellotta. (2008). Geotechnical engineering. London ; New York: Taylor & Francis, Cop.
- Alexander Grakovski, Yunusov, S., & Medvedev, A. (2020). Static Approach for Solving the Problem of Cargo Weight Distribution on Vehicle's Axles. Lecture Notes in Networks and Systems, 151–161. https://doi.org/10.1007/978-3-030-44610-9_16
- Danish Wind Industry Association (DWIA). (2023). Wind with Miller v3.0. Retrieved from Xn--drmsttre-64ad.dk website: <http://www.xn--drmsttre-64ad.dk/wp-content/wind/miller/windpower%20web/en/kids/index.htm>
- Tilt Renewables Australia Pty Ltd. (2022). Rye Park Wind Farm - Project Approvals and Applications- Traffic Management Plan. Retrieved March 10, 2023, from Tilt Renewables website: <https://www.tiltrenewables.com/assets-and-projects/Rye-Park-Wind-Farm/project-approvals-and-applications/>

- Neeraj Gupta. (2016). A review on the inclusion of wind generation in power system studies. *Renewable and Sustainable Energy Reviews*, 59, 530–543. <https://doi.org/10.1016/j.rser.2016.01.009>
- Vestas. (2020). Annual Report 2020. Retrieved March 15, 2023, from www.vestas.com website: <https://www.vestas.com/en/investor/reports-and-presentations/vestas-reporting>
- The New South Wales Government (NSW). (2011). Bowmans Creek Wind Farm- Environmental impact statement. Retrieved February 10, 2023, from www.planningportal.nsw.gov.au website: <https://pp.planningportal.nsw.gov.au/major-projects/projects/flyers-creek-wind-farm>
- Liebherr Group. (2023). LR 1400 SX. Retrieved March 10, 2023, from www.liebherr.com website: <https://www.liebherr.com/en/ita/products/mobile-and-crawler-cranes/crawler-cranes/lr-crawler-cranes/details/lr1400.html#>
- WindEurope. (2020). Decommissioning of Onshore Wind Turbines. Retrieved March 5, 2023, from [WindEurope](http://www.windeurope.org) website: <https://windeurope.org/intelligence-platform/product/decommissioning-of-onshore-wind-turbines/>
- Solar FlexRack, LLC. (2023). TDP 1.0 - Solar Tracker. Retrieved March 8, 2023, from [Solar FlexRack](http://www.solarflexrack.com) website: <https://www.solarflexrack.com/flextrack-a-series>
- First Solar. (2023). Series 6 Family. Retrieved February 28, 2023, from www.firstsolar.com website: <https://www.firstsolar.com/en/Products/Series-6>

The New South Wales Government (NSW). (2022). Daroobalgie Solar Farm- Appendix A Updated Project description. Retrieved March 7, 2023, from www.planningportal.nsw.gov.au website: <https://pp.planningportal.nsw.gov.au/major-projects/projects/daroobalgie-solar-farm>

The New South Wales Government (NSW). (2022a). Oxley Solar Farm - Appendix A Updated Project Description and Schedule of Lands. Retrieved March 7, 2023, from www.planningportal.nsw.gov.au website: <https://pp.planningportal.nsw.gov.au/major-projects/projects/oxley-solar-farm>

Fotowatio Renewable Ventures (FRV). (2023). The Project-Winton Solar Farm. Retrieved March 6, 2023, from FRV Winton Solar Farm website: <https://wintonsolarfarm.com/about-us/>

Annex : Structural Design Procedure

This section provides design procedure for the structural design of asphalt pavements in renewable energy plants, following a mechanistic-empirical pavement design approach.

The Design Methodology

The design procedure presented in this study can be applied to pavements characterized by at least one asphalt course with a thickness not lower than 5 cm, laid on unbound aggregate and/or stabilized aggregate courses. The underlying subgrade is intended to be a natural, corrected, or stabilized soil. The typical service life of asphalt pavements designed according to the sector guidelines is 20 years. Different pavement service life durations can be assumed when justified by specific strategic choices, also related to the work relevance and to the available resources.

A mechanistic-empirical method is used for the design of asphalt pavements. Such a method combines the response of the pavement under loading, computed by means of a mechanistic approach, to empirical laws that describe the structural damage evolution of the pavement with respect to specific distresses (e.g., rutting and fatigue cracking). These empirical laws, known as transfer functions, are obtained from laboratory experimental tests combined with real-scale field tests, and further validated by means of real pavement monitoring and observations. Transfer functions mathematically correlate the pavement response under loading to limiting conditions with regard to specific distress types.

The mechanistic-empirical design procedure is based on an iterative process. Once a trial pavement structure is defined, transfer functions are used to estimate the allowable conditions to prevent failures. By comparing the forecast traffic to the allowable conditions, the structural verification is performed by computing the level of damage accumulated in the pavement service life by means of a linear law of damage accumulation. The analysis is performed independently for each distress type. When the damage is lower or equal to the unity, the trial structure is verified. Otherwise, in cases of damage exceeding the unity, the trial structure must be modified until all structural requirements are met.

The distress types considered in this study are those related to traffic loading. In particular, structural rutting, fatigue cracking and shear failure caused by superheavy loads are the damaging mechanisms involved in the analysis. Further damaging modes, such as those specifically related to environmental actions, can be added to the structural design procedure in case of extraordinary service conditions.

By referring to rutting, the design approach is based on the limitation of the vertical compressive strain on the top of the subgrade. When considering fatigue cracking of the asphalt layers, a “bottom-up” mechanism is assumed for structural analysis. In the specific case of cracks and/or ruts induced by superheavy loads, a shear mechanism of failure is taken into consideration.

Traffic

Information on traffic during the pavement service life is estimated for design purposes. The design traffic is expressed by means of a detailed description of axle load, axle group type (single, tandem, or tridem), and the number of load applications for each combination of axle group type and load. Vehicles of mass greater than 3.5 t are only included in the design process. Vehicles of lower mass can be neglected from the structural design process, as they are typically considered to have a negligible impact on the pavement structures.

The results of the traffic analysis, referred to the period of analysis, is converted into equivalent passages of a reference axle. The reference axle used in the structural design is a single axle of 80 kN with dual tires and tyre pressure of 700 kPa. The number of load applications by each elementary axle is converted in equivalent passages of the reference axle by means of an Equivalent Axle Load Factor (EALF), as indicated in Equation (1) :

$$EALF = K \cdot \left(\frac{P}{P_0}\right)^\alpha \quad (1)$$

Where:

- *EALF* is the equivalency factor between generic elementary axle and reference axle;
- *P* is the load on the generic elementary axle, in kN;
- *P₀* is the load on the reference axle, equal to 80 kN;
- *K* is a coefficient that depends on the load group type at which the elementary axle belongs, assumed equal to 1 for single axle, 0.7 for tandem axle group, and 0.55 for tridem axle group;
- *α* is a coefficient that depends on the structural type, assumed equal to 4.

In the case of a single axle type, the elementary axle corresponds to the single axle itself. In the case of tandem and tridem axle groups, the elementary axle corresponds to each of the two axles composing the tandem axle group or each of the three axles composing the tridem axle group, respectively. Hence, a tandem axle group is composed of two elementary axles while a tridem axle group is composed of three elementary axles.

The number of equivalent load applications by the reference axle can be computed by the formular as indicated in Equation (2):

$$N_{ref} = \sum_i \sum_{j=1}^3 EALF_{ij} \cdot N_{ij} \quad (2)$$

Where:

- N_{ref} is the equivalent number of load applications by the design reference axle;
- $EALF_{ij}$ is the equivalency factor for a generic elementary axle of i^{th} load and j^{th} configuration ($j=1$ for single axle, $j=2$ for tandem axle group, and $j=3$ for tridem axle group);
- N_{ij} is the number of elementary axles of i^{th} load and j^{th} configuration.

Climate

Precipitation and temperature information referred to the construction site are needed for design purposes. Such data can be collected from official databases or directly from meteorological stations, verifying the climatic coherency between the pavement construction site and the selected station. A minimum analysis period of 5 years is required.

The effect of climate on the variations in materials' mechanical properties can be taken into consideration by referring to 12 analysis periods, corresponding to the 12 months of the year.

For each month, climatic data are needed to predict moisture conditions and freeze thaw cycles in the subgrade. Hence, the stiffness of the subgrade must be estimated for each analysis period considering moisture conditions, as well as potential changes in mechanical properties caused by frost and thaw cycles.

Monthly changes in temperature and precipitations are neglected for the definition of the Poisson's ratios of the subgrade, and, more generally, for the definition of the mechanical properties of granular and stabilized courses. The effect of climate on the mechanical properties of the wearing course is always

neglected since the wearing course does not contribute to the structural functions of the pavement. It is assumed that the stiffness of the asphalt layers depends on temperatures, while the stiffness of the subgrade soil depends on moisture conditions and temperatures.

The stiffness of all the asphalt layers can be determined for each analysis period as a function of the average air temperature. By knowing the average air temperature, the average pavement temperature for each asphalt layer can be calculated as indicated in Equation (3), by considering the intermediate depth of each layer:

$$T_P = \frac{(450 \cdot T_A + 1500) \cdot z + 5715 \cdot T_A + 13970}{450 \cdot z + 4572} \quad (3)$$

Where:

- T_P is the temperature of the asphalt mixture, in °C;
- T_A is the air temperature, in °C;
- z is the depth from the pavement surface, in cm.

The stiffness of the subgrade is estimated for each analysis period considering moisture conditions, while the potential changes in mechanical properties caused by freeze and thaw cycles is neglected in the present design procedure. Moreover, the effects of monthly changes in temperature and precipitation are as well neglected in the definition of the Poisson's ratios of the pavement layers.

Structural Analysis

The multi-layer elastic system is assumed as the reference structural model. Each material is considered as linearly elastic, homogeneous, isotropic, with a stress-strain response defined by means of an elastic modulus and a Poisson's ratio coefficient. Each layer is assumed as infinite in lateral extension and characterized by a constant thickness, except for the subgrade, which is modelled as a homogeneous infinite half-space. Continuity conditions are assumed to be valid at all interfaces, coherently with the structural hypothesis of full adhesion between layers.

Based on the structural model described above, in the design procedure 12 multi-layer systems can be defined. Each multi-layer system, which refers to one of the 12 analysis periods, will be characterized by asphalt modulus and subgrade modulus that take into account the effects of climate. The elastic moduli of the granular materials are assumed to be equal to their resilient moduli, with the possibility of taking into consideration non-linearity.

For each structure, the stress-strain response of the pavement under loading will be computed. The load applied to the multi-layer system is that given by the reference 80 kN axle in dual tire configuration. For structural analysis purposes, the semi-axle is considered. The reference semi-axle is composed of two circular loads of 20 kN each, characterized by a uniform pressure of 700 kPa. Dual spacing is assumed to be 0.35 m.

The response of each structure under loading is computed at critical depths, which depend upon the specific failure criterion considered. By referring to fatigue cracking, the principal horizontal tensile strain at the bottom of asphalt layer will be determined. The critical response for structural rutting is represented by the vertical compressive strain at the top of the subgrade.

Such responses will be evaluated in three distinct transversal positions:

- Position 1- on the vertical axis of one of the two circular loads;
- Position 2- at the centre-point between the two circular loads vertical axis; and
- Position 3- at the edge of one circular load, in the closest point to position 2.

The structural response under loading can be derived from computation tools based on the multi-layer elastic structural model. Each layer must be described by means of an elastic modulus and a Poisson's ratio. Moreover, continuity conditions must be satisfied at all interfaces.

When considering shear failure, the maximum shear stresses generated by the heaviest axle load are computed in the subgrade and in all unbound subbase layers by considering the elastic properties of the multilayer system and the friction angle of the materials in critical environmental conditions.

Damage Laws

For the distresses such as fatigue cracking and rutting, the analysis of damage can be carried out by means of empirical damage laws, which correlate the structural responses in the pavement under loading to limiting failure conditions. Such damage laws are known as transfer functions.

In the case of fatigue cracking, by assuming a "bottom-up" mechanism of cracking, the control parameter computed by means of the structural analysis is the principal horizontal tensile strain at the bottom of each asphalt layer in the most critical transverse position (i.e., among position 1, 2, and 3). Limiting failure conditions are given by the number of allowable load repetitions to prevent fatigue cracking.

The corresponding transfer function for fatigue cracking is presented in Equation (4):

$$N_f = \frac{1}{F_{rel}} \cdot F_{lab} \cdot F_h \cdot f_1 \cdot \left(\frac{1}{\varepsilon_t}\right)^{f_2} \cdot \left(\frac{1}{E}\right)^{f_3} \quad (4)$$

Where:

- N_f is the number of load applications that leads to limiting conditions for fatigue damage in asphalt layer;
- F_{rel} is a reliability parameter;
- F_{lab} is a shift factor that relates laboratory performance to field performance, assumed equal to 10;
- F_h is a shift factor that accounts for the self-healing capability of the binder phase of the mixture;
- f_1, f_2, f_3 are regression parameters;
- ε_t is the principal horizontal tensile strain at the bottom of the layer, in m/m;
- E is the elastic modulus of asphalt concrete, expressed in MPa.

Depending on the relevance of the project, the regression parameters f_1 , f_2 and f_3 can be obtained from experimental laboratory tests or taken from the sector literature.

When the regression parameters are obtained from a laboratory experimentation, the effects of both the level of strain and the temperature must be considered. It is typically to determine the fatigue resistance of the asphalt mixtures by carrying out four-point bending tests on prismatic specimens according to EN standards (EN 12697-24). According to the experimental approach, fatigue tests must be carried out at three temperatures and, for each temperature, at three strain levels. For each combination of temperature and strain, six specimens must be tested. The strain levels can be selected to reach failure conditions in a strain interval that includes the equivalent number of load applications of the reference 80 kN axle obtained from the traffic analysis. The test frequency can be set at 10 Hz. The criterion used to define the number of load cycles to failure can be based on a 50% reduction in the initial modulus. When fatigue tests are performed at a single reference temperature (instead of three temperatures), the regression parameters f_1 and f_2 can be derived from the experimental tests, while the f_3 parameter can be set equal to 1.8. The reference test temperature can be assumed in the interval comprised between 10 °C and 20 °C.

In the case of preliminary or minor projects, it is also possible to derive the parameters f_1 and f_2 from the sector literature. For asphalt mixtures containing traditional bituminous binders, the regression parameter f_2 is set to equal to 5 and the parameter f_1 can be determined according to the relation presented in Equation (5):

$$f_1 = (6918 \cdot 10^{-6} \cdot (0.856 \cdot V_b + 1.08))^5 \quad (5)$$

Where:

- V_b is the volumetric percentage of the binder phase, in %.

F_{rel} is a reliability factor, which must be related to the importance of the project and to the degree of uncertainty of the fatigue characterization of the bituminous mixture. A value of 6 was considered in this study to be conservative.

For the self-healing shift factor F_h , which takes into account the self-healing capability of the binder phase of the bituminous mixture, it is recommended to assume a value equal to 1 when specific experimental investigations are not carried out to evaluate the self-repairing properties of the binder, in the environmental and load conditions representative of the site in question.

In the case of rutting, the transfer function correlates the vertical compressive strain on the top of the subgrade to the number of allowable load repetitions to prevent the accumulation of excessive permanent deformation.

The corresponding transfer function is presented in Equation (6):

$$N_d = f_4 \cdot \left(\frac{1}{\varepsilon_c}\right)^{f_5} \quad (6)$$

Where:

- N_d is the number of load applications that leads to limiting conditions for rutting;
- f_4 is a regression parameter assumed equal to $6.15 \cdot 10^{-7}$;
- f_5 is a regression parameter assumed equal to 4;
- ε_c is the vertical compressive strain at the top of the subgrade, in m/m.

In the case of shear failure, the shear strength of the subgrade soil and of the materials composing the unbound layers can be estimated in critical environmental conditions by means of a criterion (Eq. 7) based on the Mohr-

Coulomb failure criterion expressed in the plane stress state in accordance with the Russian structural pavement design guide (ODN 218.046-01):

$$\tau_{all} = \frac{1}{F_{rel}} \cdot (c \cdot k + \sigma \cdot \tan\varphi) \quad (7)$$

Where:

- τ_{all} is the shear strength, in MPa;
- F_{rel} is a reliability parameter that depends on the importance of the pavement;
- c is the cohesion, in MPa;
- k is a parameter that depends on the boundary properties at the layer interface;
- σ is the normal stress, in MPa; and
- φ is the angle of internal friction, expressed in °.

Structural Verification

The damage caused by traffic must be calculated separately for fatigue and rutting, adopting for each distress type a linear law of damage accumulation, as indicated in Equation (8):

$$D_{f,d} = \sum_{k=1}^{12} \frac{n_k}{N_k} \quad (8)$$

Where:

- D_f and D_d are the damage of fatigue and rutting, respectively;
- n_k is the number of applications of equivalent axles in the generic climatic period k ;
- N_k is the number of applications of projected equivalent axles in the generic climatic period k that leads to limiting damage conditions due to fatigue or rutting (evaluated by means of transfer functions).

By referring to shear failure, the ratio between the shear stress computed by means of the structural analysis and the allowable shear strength of the analyzed layer, is verified as indicated in Equation (9):

$$D_\tau = \frac{\tau}{\tau_{all}} \quad (9)$$

Where:

- D_τ is the damage induced by shear;
- τ is the maximum shear stress generated by the heaviest axle load, in MPa;
- τ_{all} is the allowable shear strength of the material composing the analyzed layer, in MPa.

The structural verification is satisfied when damage values computed for fatigue, rutting, and shear are all lower than the unity.

When the structural verification is satisfied, the trial pavement configuration can be validated. Otherwise, it is necessary to modify the layer thicknesses and/or the structural type and repeat the structural design procedure following an iterative process, until the structural verification is satisfied.

The thicknesses of the layers deriving from the design process are intended as a minimum requirement and do not take into account construction approximations and tolerances.